



**INTERNAL DAMAGE DETECTION AND ASSESSMENT IN
BEAMS USING EXPERIMENTAL NATURAL FREQUENCIES**

THESIS

Frances K. Durham, Ensign, USNR

AFIT/GAE/ENY/05-J03

**DEPARTMENT OF THE AIR FORCE
AIR UNIVERSITY**

AIR FORCE INSTITUTE OF TECHNOLOGY

Wright-Patterson Air Force Base, Ohio

APPROVED FOR PUBLIC RELEASE; DISTRIBUTION UNLIMITED

The views expressed in this thesis are those of the author and do not reflect the official policy or position of the United States Air Force, Department of Defense, or the United States Government.

INTERNAL DAMAGE DETECTION AND ASSESSMENT IN
BEAMS USING EXPERIMENTAL NATURAL FREQUENCIES

THESIS

Presented to the Faculty

Department of Aeronautics and Astronautics

Graduate School of Engineering and Management

Air Force Institute of Technology

Air University

Air Education and Training Command

in Partial Fulfillment of the Requirements for the
Degree of Master of Science in Aeronautical Engineering

Frances K. Durham, B.S.

Ensign, USNR

June 2005

APPROVED FOR PUBLIC RELEASE; DISTRIBUTION UNLIMITED

INTERNAL DAMAGE DETECTION AND ASSESSMENT IN
BEAMS USING EXPERIMENTAL NATURAL FREQUENCIES

Frances K. Durham, B.S.

Ensign, USNR

Approved:

_____ Anthony N. Palazotto, Ph.D. Thesis Advisor	_____ Date
_____ Richard G. Cobb, Ph.D. Committee Member	_____ Date
_____ Donald L. Kunz, Ph.D. Committee Member	_____ Date

Abstract

This study investigated the frequency response of a cantilever beam with the intent of establishing a reliable nondestructive method of damage detection. The test specimens were twelve Al 2024 T3 beams, each identical excepting a unique eccentrically located notch, and one reference notchless beam. The machined notches varied in length and location to simulate varying degrees of damage. Laser doppler vibrometry enabled the data acquisition. The changes in natural frequencies were correlated to notch length and notch location. A comparison of eccentric and centered notch influence on the natural frequencies was also discussed.

Acknowledgements

I would like to thank Dr. Anthony Palazotto for his guidance and humor in the role of my thesis advisor. I would also like to acknowledge the members of my committee Dr. Rich Cobb and Dr. Donald Kunz, for their input and insight. I thank Mr. Mark Derriso for his financial support. I also thank Mr. Wilbur Lacy and Mr. Jay Anderson for their help in the lab. They were always ready and willing to assist with their knowledge and support. Finally, I thank my parents for always expecting more from me.

Frances K. Durham

Table of Contents

	Page
Abstract	iv
Acknowledgements	v
List of Figures	viii
List of Tables	xii
I. Introduction	1-1
1.1 Motivation	1-1
1.2 Background	1-3
II. Theoretical Development	2-1
2.1 Natural Frequency Changes	2-1
2.2 Classical Beam Theory	2-2
2.3 Cobb-Durham Code	2-6
2.4 Perel-Palazotto Code	2-10
2.5 Theory Behind Laser Vibrometry	2-15
III. Experiment Setup and Procedure	3-1
3.1 Sample preparation	3-1
3.2 Support system	3-4
3.3 Excitation	3-7
3.4 Laser Doppler Vibrometer	3-10
3.5 Hardware Arrangement	3-11
3.6 Software preparation	3-12
3.7 Analysis	3-14
IV. Results and Discussion	4-1
4.1 Abberations in the FRF plots and Mode Shapes	4-1
4.2 Changes in Natural Frequency	4-4
4.3 Comparison with Beams Containing Centered Notches	4-16
4.4 Perel-Palazotto Code	4-24
4.5 Cobb-Durham Code	4-26
4.6 Notch Depth	4-28

	Page
4.7 Locations of maximum shear	4-32
4.8 Locations of Maximum Curvature	4-37
4.9 ABAQUS Model	4-40
V. Conclusions and Recommendations for Further Study	5-1
Appendix A. Mode Shapes and Frequencies of the Eccentrically Notched Beams	A-1
Appendix B. Cobb-Durham Code	B-1
Appendix C. Beam Drawings	C-1
Bibliography	BIB-1

List of Figures

Figure		Page
1.1.	Test support setup and amplifier.	1-6
1.2.	Laser vibrometer setup.	1-7
1.3.	Beams containing centrally located notches and reference notchless beam.	1-7
2.1.	A differential beam element.	2-2
2.2.	First eight modes of vibration of an isotropic cantilever beam.	2-7
2.3.	Finite element model of beam.	2-9
2.4.	Diagram of sublaminates dimensions.	2-10
3.1.	Beams containing eccentrically located notches.	3-2
3.2.	Beam containing additional holes.	3-3
3.3.	Beam with piezoelectric actuator affixed.	3-4
3.4.	Test support setup.	3-5
3.5.	Properly clamped beam flush with clamp.	3-6
3.6.	Acoustic horn.	3-8
3.7.	220 DN Bogen amplifier.	3-8
3.8.	Distance of acoustic horn from beam.	3-9
3.9.	ACX Quick Pack Power Amplifier Model EL 1224.	3-10
3.10.	Acoustic horn position.	3-12
4.1.	Eighth modal shape of beam containing 12-cm notch at clamped end, excited by acoustic horn at clamped end.	4-2
4.2.	FRF plots of beam with 12-cm notch located at the clamped end, excited by horn at three locations.	4-3
4.3.	Eighth modal shape of beam containing 12 cm notch at clamped end, excited by horn at free end.	4-4
4.4.	FRF plot of notchless beam excited by piezoelectric actuator.	4-5
4.5.	FRF plot of notchless beam excited by acoustic horn at clamped end.	4-6

Figure		Page
4.6.	Fourth modal shape of beam containing 8-cm notch in the middle.	4-8
4.7.	Fifth modal shape of beam containing 8-cm notch in the middle.	4-9
4.8.	Frequency modes of beam containing eccentrically located notch at the free end.	4-9
4.9.	Frequency modes of beam containing eccentrically located notch in the middle.	4-10
4.10.	Frequency modes of beam containing eccentrically located notch at the clamped end.	4-10
4.11.	Modal frequency percent deviation of 4-cm eccentrically notched beams.	4-13
4.12.	Modal frequency percent deviation of 8-cm eccentrically notched beams.	4-14
4.13.	Modal frequency percent deviation of 12-cm eccentrically notched beams.	4-14
4.14.	Modal frequency percent deviation of 16-cm eccentrically notched beams.	4-15
4.15.	Frequency modes of beam containing centrally located notch at the free end.	4-18
4.16.	Frequency modes of beam containing centrally located notch in the middle.	4-19
4.17.	Frequency modes of beam containing centrally located notch at the clamped end.	4-19
4.18.	Modal frequency percent deviation of 4-cm centrally notched beams.	4-22
4.19.	Modal frequency percent deviation of 8-cm centrally notched beams.	4-22
4.20.	Modal frequency percent deviation of 12-cm centrally notched beams.	4-23
4.21.	Modal frequency percent deviation of 16-cm centrally notched beams.	4-23
4.22.	Computational modal frequency percent deviation of 4-cm notched beams.	4-29
4.23.	Computational modal frequency percent deviation of 8-cm notched beams.	4-29

Figure		Page
4.24.	Computational modal frequency percent deviation of 12-cm notched beams.	4-30
4.25.	Computational modal frequency percent deviation of 16-cm notched beams.	4-31
4.26.	ABAQUS bending mode 1.	4-41
4.27.	ABAQUS bending mode 2.	4-41
4.28.	ABAQUS bending mode 3.	4-42
4.29.	ABAQUS bending mode 4.	4-42
4.30.	ABAQUS bending mode 5.	4-43
4.31.	ABAQUS bending mode 6.	4-43
4.32.	ABAQUS bending mode 7.	4-44
4.33.	ABAQUS bending mode 8.	4-44
A.1.	First eight mode shapes and modal frequencies of the notchless beam.	A-1
A.2.	First eight mode shapes and modal frequencies of the beam containing the 4-cm notch at the clamped end.	A-2
A.3.	First eight mode shapes and modal frequencies of the beam containing the 8-cm notch at the clamped end.	A-3
A.4.	First eight mode shapes and modal frequencies of the beam containing the 12-cm notch at the clamped end.	A-4
A.5.	First eight mode shapes and modal frequencies of the beam containing the 16-cm notch at the clamped end.	A-5
A.6.	First eight mode shapes and modal frequencies of the beam containing the 4-cm notch in the middle.	A-6
A.7.	First eight mode shapes and modal frequencies of the beam containing the 8-cm notch in the middle.	A-7
A.8.	First eight mode shapes and modal frequencies of the beam containing the 12-cm notch in the middle.	A-8
A.9.	First eight mode shapes and modal frequencies of the beam containing the 16-cm notch in the middle.	A-9
A.10.	First eight mode shapes and modal frequencies of the beam containing the 4-cm notch at the free end.	A-10
A.11.	First eight mode shapes and modal frequencies of the beam containing the 8-cm notch at the free end.	A-11

Figure		Page
A.12.	First eight mode shapes and modal frequencies of the beam containing the 12-cm notch at the free end.	A-12
A.13.	First eight mode shapes and modal frequencies of the beam containing the 16-cm notch at the free end.	A-13

List of Tables

Table		Page
2.1	Resonant eigenvalues for an isotropic cantilevered beam.	2-5
4.1.	Modal frequencies of notchless beam with different excitation sources.	4-3
4.2.	Comparison of theoretical and experimental modal frequencies for the notchless case.	4-5
4.3.	Experimental modal frequencies for the beams containing eccentrically located notches.	4-7
4.4.	Modal frequencies obtained from the least-squares curve-fit of the experimental data of the eccentrically notched beams.	4-12
4.5.	Comparison of eccentrically and centrally notched beams normalized by the notchless cases.	4-17
4.6.	Modal frequencies obtained from the least-squares curve-fit of the experimental data of the centrally notched beams.	4-21
4.7.	Ranges of percent deviation from notchless case for 4-cm and 8-cm notched beams for mode 5, mode 6, and mode 7.	4-24
4.8.	Comparison of theoretical and Perel-Palazotto natural frequencies of the notchless beam.	4-25
4.9.	Comparison of the experimental results and the Perel-Palazotto code results for selected cases.	4-25
4.10.	Comparison of theoretical and Cobb-Durham natural frequencies of the notchless beam.	4-26
4.11.	Comparison of experimental and Cobb-Durham results for the eccentrically notched beams.	4-27
4.12.	Comparison of experimental and Cobb-Durham results for the centrally notched beams.	4-28
4.13.	Modal frequency and nodes crossed of the eccentrically notched beams.	4-33
4.14.	Percent change between notch size and number points of maximum shear crossed in the eccentrically notched beam.	4-34
4.15.	Percent change between notch size and number points of maximum shear crossed in the centrally notched beam.	4-36

Table		Page
4.16.	Percent change between notch size and number anti-nodes crossed in the eccentrically notched beam.	4-38
4.17.	Percent change between notch size and number anti-nodes crossed in the centrally notched beam.	4-39
4.18.	Comparison of experimental ABAQUS modal frequencies for the 4-cm and 8-cm clamped-end notched beams.	4-40

INTERNAL DAMAGE DETECTION AND ASSESSMENT IN BEAMS USING EXPERIMENTAL NATURAL FREQUENCIES

I. Introduction

The present study investigated experimentally the use of natural frequency as a global diagnostic parameter. Notches were eccentrically placed in a beam to simulate a delamination, and an acoustic horn causes the beam to vibrate. The off-centered placement exaggerated the effects on the frequency modes in a vibrating beam. The vibration was measured and analyzed using a laser doppler vibrometer. This study investigated the natural frequency response of an off-centered notch in comparison to a centered notch. The history of studies on natural frequency response in beams follow in Chapter I. Chapter II briefly overviews classical theory, as well as the theory behind the computer models and the laser doppler vibrometer. Chapter III outlines the experimental equipment and the procedure followed. The experimental results are presented and compared with the computer modeling results, and further discussed in Chapter IV. The conclusions are presented in Chapter V.

1.1 Motivation

The need for an advanced structural health monitoring system can be found in several industries. The continual rise in air traffic has burdened the aerospace industry with demands for lower aircraft production and maintenance costs coupled with operational efficiency and environmentally friendly operations, while maintaining the level of safety. Health monitoring systems hold the possibility of reducing structural weight and minimizing structural inspection requirements.²⁰ These effects in turn reduce operation and maintenance costs significantly.

The demand for advancement of structural health monitoring is also growing in the space industry, as spacecraft size, complexity, and lifetime continue to increase. Damage is likely to occur due to exposure to the space environment, orbital maneuvering loads, spacecraft docking operations, and collisions with space debris.⁵ The common visual inspection is impractical and/or impossible in many space applications, such as unmanned spacecraft and spacecraft in high-altitude orbits. A reliable method of in-orbit damage detection of both location and extent is critical to schedule necessary repairs and/or mission changes.

A large portion of the costly maintenance required for the space shuttle is examination of the structural integrity. Fatigue, foreign object debris (FOD), and operational vibrations cause damage that is not always visible at the surface. The present methods of locating damage are costly and time-consuming. The present study investigates a possible simpler, less expensive method. If the self-monitoring systems in satellites could detect structural damage, they could possibly repair the damage before operational ability was impaired.

Global monitoring gives an immediate evaluation of the structural health. Visual inspections require extensive time and labor. Often disassembly is required to reach the important load bearing structures. Manually performed local non-destructive damage evaluation (NDE) methods are time-consuming and inefficient. Vibration-based global monitoring not only allows immediate evaluations, but can also be used for continuous long-term monitoring. The goal would be to extract information about the structure's remaining lifetime, time intervals to the next maintenance/repair and immediate shutdown.¹² This information would benefit many fields, including civil engineering structures, railway systems, wind power stations, and others. Global methods require a coarse sensor network since they monitor the whole system, but they are less sensitive and have a lower spatial resolution than the local methods. However, these problems can be resolved by using a computational model.¹²

1.2 Background

Initially, the concept of monitoring vibration to determine damage presence concerned rotor cracking in machinery and railroad equipment. Since then, vibration testing has been used extensively in industry to monitor rotating machinery.⁵ The earliest results concerning these applications is presented by Dimaroganas⁷ (1970). The work presented by Nagy, Dousis, and Finch (1978) on the cracks in railroad wheels noted the shift in resonance frequencies due to the presence of cracks.

Extensive research has been recorded on the vibration testing of beams with included cracks/notches. Cawley and Ray⁴ conducted an experiment to compare the natural frequency changes produced by cracks and slots in order to study the accuracy of experimentally modeling a crack with a slot. They tested simply supported steel beams containing single surface slots of equal depth and varying width. The report concluded that even when the slot width was small compared to the beam dimensions, the slot width still had a strong influence on the natural frequency changes. Therefore, the ability to detect a slot does not necessarily ensure the ability to detect a crack of the same depth. Along the length of the beam, the slots were located in the middle for all the test cases, which resulted in significant natural frequency changes in the first and third flexural modes, but in negligible changes in the second and fourth modes. The latter two modes have a stress and displacement node at the middle of the bar. In general, the natural frequency changes correlated well with reduction in the mid-bar second moment of inertia due to an increase in width of the slot.

Kam and Lee¹³ (1992) formulated a procedure to identify the cracked element and to estimate the crack size in a cantilevered beam from modal test data. The beam was discretized into a set of elements and the crack was assumed to be located within one of the elements. The measured vibration frequencies and mode shapes were used to identify the location of the damage by determining the cracked element using a simple reduced stiffness model. The crack size is estimated by comparing

the strain energy of the intact beam with the tested beam. The strain energy of the uncracked structure is determined by

$$W_0 = \frac{1}{2}[r_0]^T[K_0][r_0] \quad (1.1)$$

where $[K_0]$ is the stiffness matrix of the uncracked structure and $[r_0]$ is the matrix of the nodal displacements, which are obtained from

$$[r_0] = [K_0]^{-1}[F] \quad (1.2)$$

The matrix $[F]$ is the applied forces on the uncracked structure. The strain energy is found for the cracked structure using the same method. The stiffness matrix of the cracked structure is derived based on the stiffness matrix of the uncracked structure and the measured vibration frequencies and mode shapes of the cracked structure. With few exceptions, the crack depth was estimated within 2%.

Several studies have investigated the correlation of damage location and mode shapes. Yuen²² (1984) showed for a cantilevered beam, the first mode shape systematically changes with respect to the damage location. The model used involved a hollow beam with a square cross-section. The effect of the damage on the inertia matrix was ignored. Higher modes did not exhibit the same trends. This deviation which was attributed to the complexity of the higher mode shapes, and the intricacy in normalizing the mode shapes.

Pandey, Biswas, and Samman¹⁵ (1990) studied the changes in the curvature mode shapes. Curvature at a point is given by

$$\nu'' = \frac{M}{EI} \quad (1.3)$$

where M is the bending moment, E is the modulus of elasticity, and I is the second moment of inertia of the cross-sectional area. The curvature was computed from

numerical results using a central difference approximation

$$\nu'' = \frac{\nu_{i+1} - 2\nu_i + \nu_{i-1}}{h^2} \quad (1.4)$$

where h is the length of the elements. This study found that the absolute difference between the curvature mode shapes of the damaged and undamaged beams was largest in the element that contained the notch. Additionally, the absolute difference increased as the damage size increased.

Doyle¹⁰ (1995) used the spectral element method to estimate crack size and location in an aluminum beam containing a transverse crack. The time response of the beam was measured using four strain gages placed on both sides of the crack and on both sides of the beam. A transverse vibration was initiated, which resulted in an axial stress wave that propagated along the beam length and reflected from the crack tips and the end of the beam. This report models the beam analytically as two beams connected by a pinned joint with torsional stiffness. The torsional stiffness can then be related to the crack size.

Palacz, Krawczuk, and Ostachowicz¹⁴ (2004) also used a spectral finite element model and flexural-shear coupled wave propagation in delaminated, multiplayer composite beams. The beam free end velocity response, monitored in the time domain, demonstrated large increases in amplitude as the stress wave crossed the crack tips and reflected from the free end. The times at which the stress wave crossed the crack tips could be noted and used to derive the crack length.

For further information on vibration testing, Dimarogonas⁸ (1996) and Salawu¹⁹ (1995) provide thorough reviews.

The present study continues the studies of an earlier thesis by Capt Aaron Reifsnnyder,¹⁸ in which cantilevered centerline-notched 2024 T3 and 2024 O aluminum beams were used to determine whether natural frequency response measurement in beam structures is a usable method of damage detection. The length of the beams,

excluding the clamped portion, was 30.5 cm, the width was 3.81 cm, and the thickness of these beams was only 3.175 mm. The lengths of the notches were 4cm, 8cm, 12cm, and 16cm, which translated to 13%, 26%, 39%, and 52% of the beam length. Twelve test specimens, each containing a single notch corresponding to one of the notch lengths and a location of the cantilevered end, the free end, or mid-bar, were manufactured plus one reference notchless beam. However, the beam containing the 8-cm notch at the clamped end was manufactured improperly. Additional beams containing notches of lengths 20 cm and 24 cm were desired for further comparison. However, the residual stresses in the Al 2024 T3 effected warping within beams containing the longer notches. Therefore, the 20-cm and 24-cm notched beams were fabricated from Al 2024 O along with another set of beams containing notches of lengths 4 cm, 8 cm, 12 cm, and 16 cm at the clamped end, for comparison. The Al 2024 O beams produced natural frequencies approximately 3% greater than the Al 2024 T3. This difference was attributed to the residual stresses in the Al 2024 T3 beams. Each beam was excited by a piezoelectric actuator, and the dynamic beam response was measured using a laser Doppler vibrometer. The modal frequencies and shapes were characterized for each test case.

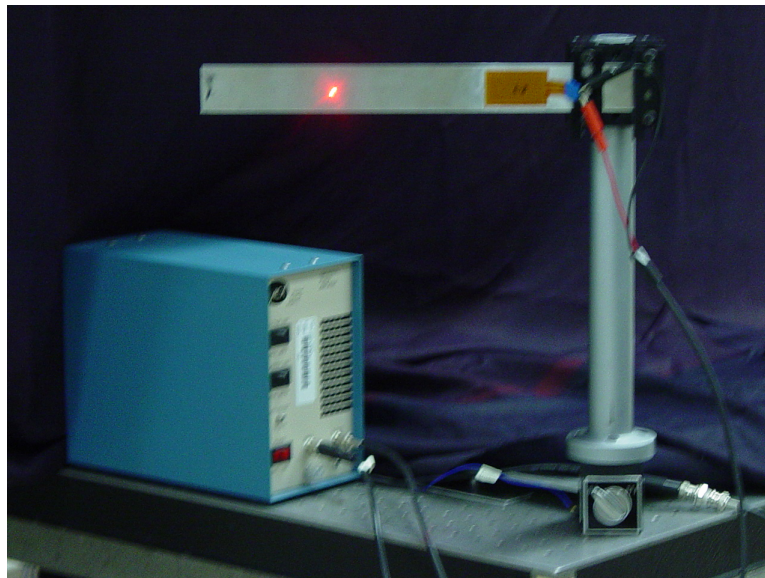


Figure 1.1 Test support setup and amplifier.

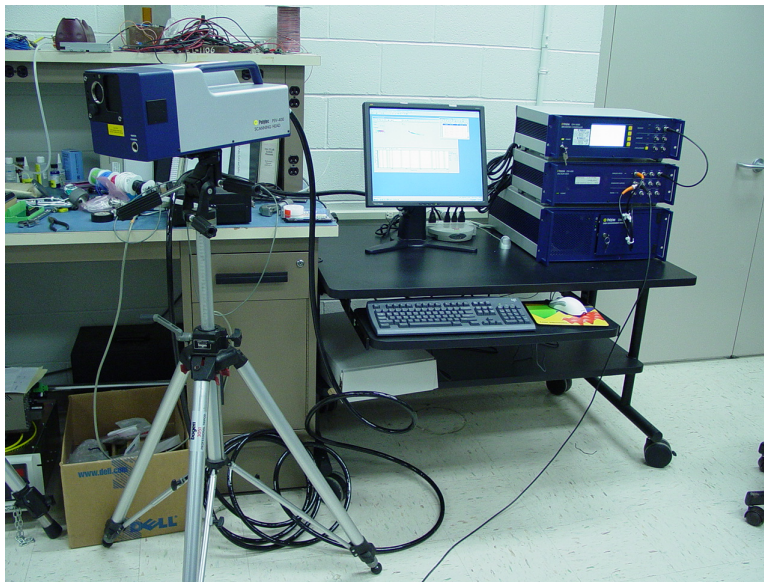


Figure 1.2 Laser vibrometer setup.

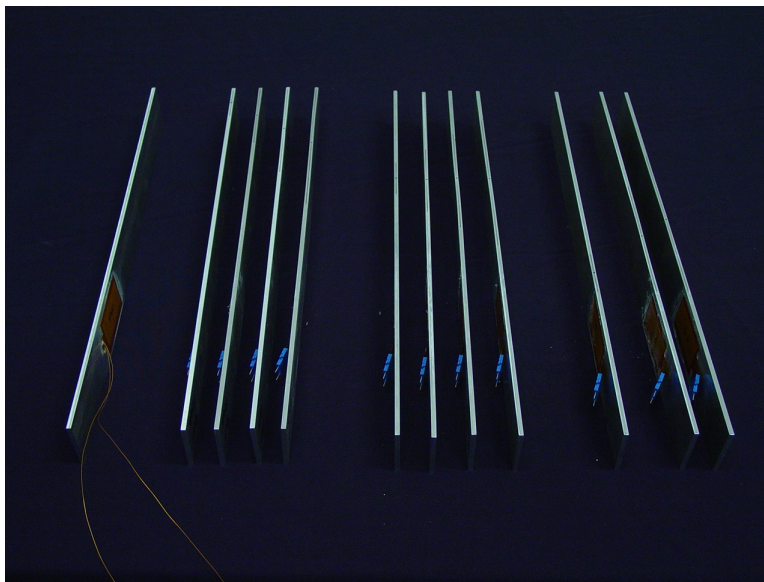


Figure 1.3 Beams containing centrally located notches and reference notchless beam.

II. Theoretical Development

The following sections present the theory considered. The first section describes the fundamental reasoning behind damage detection through vibration analysis. The next section outlines classical beam theory and the assumptions involved. The next two sections describe the composition of the Cobb-Durham and Perel-Palazotto finite element codes respectively. The final section discusses the signal processing of the laser vibrometer.

2.1 Natural Frequency Changes

Damage results in structural reduction in stiffness and increase in damping. A crack changes the dynamic frequency modes in a beam by changing the stiffness matrix, which is dependent on the moment of inertia, I . The reduction in stiffness corresponds to decreases in natural frequencies and alterations in the modes of vibrations. The modal characteristics, i.e. the modal shapes and modal damping, shift. The changes in characteristic properties between the measured state and the intact state can be used to categorize the extent and location of the damage. This method of damage detection requires a reliable reference model.¹²

A crack in a structure also causes changes in the damping because a plastic zone appears along the crack edge. However, the changes in damping are usually relatively small compared to the total damping of the structure.⁸ The methods used for modeling frequency response to crack depth are generally linear. However, for a breathing crack, a crack that opens and closes during vibration, the linear constant proportionality is different for an open crack and a closed crack. Thus, the crack will behave as a bilinear spring.

2.2 Classical Beam Theory

The natural frequencies of an isotropic cantilever beam can be determined using the analytical approach outlined by Meirovitch (1986). A one-dimensional differential beam element is considered with a shear and a bending moment at both ends, and an applied external load along the length of the element.

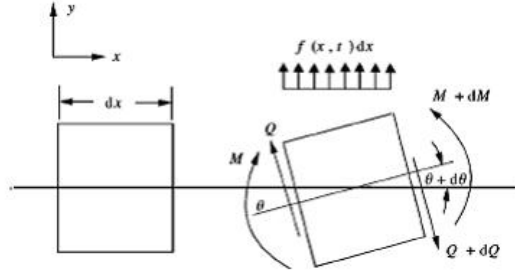


Figure 2.1 A differential beam element.

When the forces are balanced, the equation of motion becomes

$$[Q(x, t) + \frac{\partial Q(x, t)}{\partial x} dx] - Q(x, t) + f(x, t) dx = m(x) dx \frac{\partial^2 y(x, t)}{\partial t^2} \quad (2.1)$$

where x is the distance along the length of the beam between 0 and L , $Q(x, t)$ is the transverse shearing force, $f(x, t)$ is the applied external load, $m(x)$ is the mass per unit length, and $y(x, t)$ is the transverse displacement. Likewise, the moment equation of motion is

$$[M(x, t) + \frac{\partial M(x, t)}{\partial x} dx] - M(x, t) + [Q(x, t) + \frac{\partial Q(x, t)}{\partial x} dx] dx + f(x, t) dx \frac{dx}{2} = 0 \quad (2.2)$$

where $M(x, t)$ is the reaction moment about the center axis of the beam. If the element is sufficiently small, the dx^2 terms can be neglected and the moment and force equations can be combined to give

$$-\frac{\partial^2 M(x, t)}{\partial x^2} + f(x, t) = m(x) \frac{\partial^2 y(x, t)}{\partial t^2} \quad (2.3)$$

The assumption of transverse shear negligibility is validated by considering the thickness of the beam and notch elements. The beam is determined thin enough from a comparison of the beam thickness and length. The thickness of the test beams of the present study is 2% of the beam length. The 4-cm notched element is also considered, as the most extreme notch case. Calculation reveals the thickest sublaminar is 10% of the notch length. Therefore, the beam elements are small enough to neglect the through-the-thickness shear. The bending moment is related to the transverse displacement through

$$M(x, t) = EI(x) \frac{\partial^2 y(x, t)}{\partial x^2} \quad (2.4)$$

where E is the modulus of elasticity and $I(x)$ is the moment of inertia of the cross-sectional area. For a rectangular beam, the moment of inertia is

$$I = \frac{bh^3}{12} \quad (2.5)$$

where b is the base or width of the beam cross-section and h is the height. Combining Equations (2.3) and (2.4) yields the fourth-order differential boundary-value equation of motion

$$-\frac{\partial^2}{\partial x^2} [EI(x) \frac{\partial^2 y(x, t)}{\partial x^2}] + f(x, t) = m(x) \frac{\partial^2 y(x, t)}{\partial t^2} \quad (2.6)$$

The natural frequencies are obtained by considering the beam with zero applied force. The boundary conditions at the clamped end are zero displacement and zero

slope.

$$y(0, t) = 0 \quad (2.7)$$

$$\frac{\partial y}{\partial x} \Big|_{x=0} = 0 \quad (2.8)$$

At the free end the curvature and its derivative are zero.

$$EI \frac{\partial^2 y}{\partial x^2} \Big|_{x=l} = 0 \quad (2.9)$$

$$\frac{\partial}{\partial x} [EI \frac{\partial^2 y}{\partial x^2}] \Big|_{x=l} = 0 \quad (2.10)$$

The transverse displacement can be represented as a product of a time-dependent bounded harmonic oscillation with frequency ω , and an x-dependent displacement function $Y(x)$. Using the method of separation of variables, and incorporating the boundary conditions, Equation (2.6) reduces to

$$-\frac{\partial^2}{\partial x^2} [EI(x) \frac{\partial^2 Y(x)}{\partial x^2}] = \omega^2 m(x) Y(x) \quad (2.11)$$

For a uniform beam with a constant mass, modulus of elasticity, and moment of inertia, Equation (2.11) becomes

$$\frac{\partial^4 Y(x)}{dx^4} - \beta^4 Y(x) = 0 \quad (2.12)$$

where

$$\beta^4 = \frac{\omega^2 m}{EI} \quad (2.13)$$

The general solution to Equation (2.12) is

$$Y(x) = C_1 \cosh(\omega x) + C_2 \sinh(\omega x) + C_3 \cos(\omega x) + C_4 \sin(\omega x) \quad (2.14)$$

where C_i are unknown coefficients that are found by solving the boundary conditions. When the clamped and free boundary conditions are applied at $x = 0$ and $x = L$

respectively, the resulting characteristic equation is

$$\cos(\beta L) \cosh(\beta L) = -1 \tag{2.15}$$

Numerically solving Equation (2.15) yields the resonant eigenvalues β_r . In the absence of a forcing function, the resonant modes are equivalent to the natural modes. The eigenvalues for the first eight natural modes are

Table 2.1: Resonant eigenvalues for an isotropic cantilevered beam.

Mode	Resonant Eigenvalues
1	1.875
2	4.694
3	7.855
4	10.966
5	14.137
6	17.279
7	20.420
8	23.562

The natural frequencies are calculated by

$$\omega_n = \beta_r^2 \text{sqr}t \frac{EI}{mL^4} \tag{2.16}$$

where the material properties are in English units. The displacement function Equation (2.14) can be rewritten as

$$Y_r(x) = \frac{C_1}{\sin(\beta_r L) - \sinh(\beta_r L)} [(\sin \beta_r L - \sinh \beta_r L)(\sin \beta_r x - \sinh \beta_r x) + (\cos \beta_r L + \cosh \beta_r L)(\cos \beta_r x - \cosh \beta_r x)] \tag{2.17}$$

The first eight mode shapes are shown in Figure 2.2.

2.3 Cobb-Durham Code

The multi-degree of freedom system is

$$[M]\ddot{x} + [C]\dot{x} + [K]x = [F]f(t) \quad (2.18)$$

“A multi-degree of freedom system can be ideally represented by a series of coupled single degree of freedom systems.”¹⁷ The measured FRF can be understood as the superposition of the FRFs of the single degree of freedom systems. In general a system will vibrate at all eigenfrequencies⁹

$$\omega(x, t) = \sum_{n=0}^{\infty} [(A_1 C_2)_n \cos(\omega_n t) + (A_2 C_2) \sin(\omega_n t)] \sin\left(\frac{nx\pi}{l}\right) \quad (2.19)$$

where A and C are constants that vary with n and n is the eigenfrequency. However, the system will vibrate at a single frequency when the initial conditions coincide with an eigenfunction.

The mode shapes of a finite element can be described as a sum of mode shape functions, assuming the modes method

$$y(x) = \sum_{i=1}^4 \psi_i(t) \nu_i(t) \quad (2.20)$$

where $y(x)$ is the transverse displacement, $\psi_i(t)$ is the mode shape function, and $\nu_i(t)$ is the nodal displacement or rotation corresponding to one of the element degrees of freedom.⁶ The following boundary conditions are imposed

$$\psi_1(0) = 1, \psi_1'(0) = \psi_1(L) = \psi_1'(L) = 0 \quad (2.21)$$

$$\psi_2(0) = 1, \psi_2'(0) = \psi_2(L) = \psi_2'(L) = 0 \quad (2.22)$$

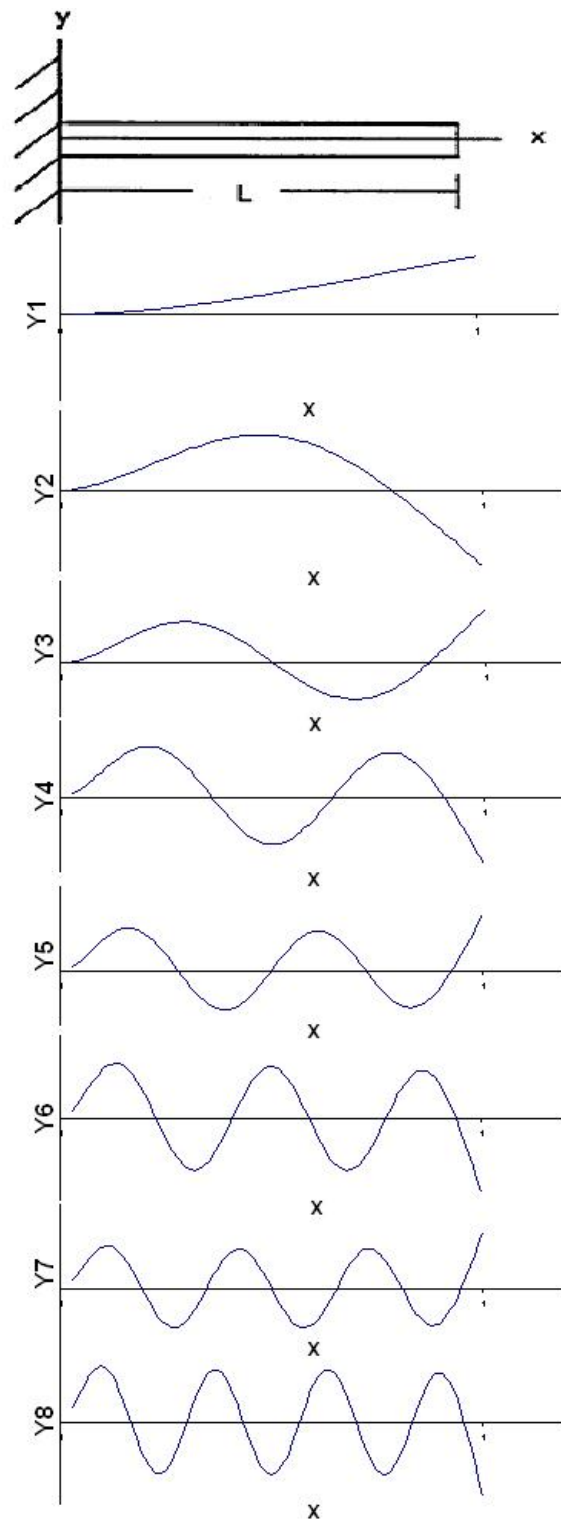


Figure 2.2 First eight modes of vibration of an isotropic cantilever beam.

$$\psi_3(0) = 1, \psi_3'(0) = \psi_3(L) = \psi_3'(L) = 0 \quad (2.23)$$

$$\psi_4(0) = 1, \psi_4'(0) = \psi_4(L) = \psi_4'(L) = 0 \quad (2.24)$$

The Bernoulli-Euler beam theory for a cantilevered beam describes the mode shape with

$$y(x) = c_1 + c_2\left(\frac{x}{l}\right) + c_3\left(\frac{x}{l}\right)^2 + c_4\left(\frac{x}{l}\right)^3 \quad (2.25)$$

where c_1 , c_2 , c_3 , and c_4 are constants specific to the mode. The mode shape functions for the first four modes are

$$\psi_1 = 1 - 3\left(\frac{x}{l}\right)^2 + 2\left(\frac{x}{l}\right)^3 \quad (2.26)$$

$$\psi_2 = x - 2l\left(\frac{x}{l}\right)^2 + l\left(\frac{x}{l}\right)^3 \quad (2.27)$$

$$\psi_3 = 3\left(\frac{x}{l}\right)^2 - 2\left(\frac{x}{l}\right)^3 \quad (2.28)$$

$$\psi_4 = -l\left(\frac{x}{l}\right)^2 + l\left(\frac{x}{l}\right)^3 \quad (2.29)$$

The elemental matrices are

$$k_{ij} = \int_0^l EI\psi_i''\psi_j''dx \quad (2.30)$$

$$m_{ij} = \int_0^l \rho A\psi_i\psi_jdx \quad (2.31)$$

The elemental matrices of each beam element are combined to form the stiffness and mass matrices of the entire structure. The following matrix is formed

$$\begin{bmatrix} 0 & I \\ -M^{-1}K & -M^{-1}C \end{bmatrix} \quad (2.32)$$

The eigenvalues and eigenvectors of this matrix are the resonant frequencies of the structure. The Cobb-Durham code assumes a small damping constant.

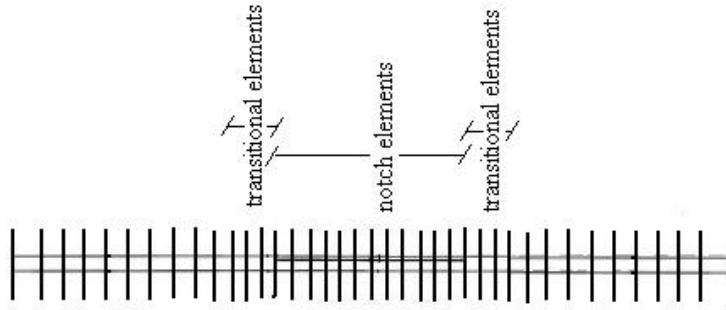


Figure 2.3 Finite element model of beam.

The finite element model was modified to include a notch of variable length. The beam was divided into 35 elements. The notched section contained 6 elements for every 4cm. Three transitional elements were added at the ends of the notches. The moment of inertia in the elements containing the notch was modified. For the undelaminated portion the moment of inertia is described by Equation (2.5). In the delaminated portion, the moment of inertia is

$$I_k = \frac{b(h_u^3 + h_l^3)}{12} \quad (2.33)$$

where h_u is the height of the upper sublaminates and h_l is the height of the lower sublaminates. This change effectively reduced the moment of inertia, which reduced the stiffness matrix to simulate damage.

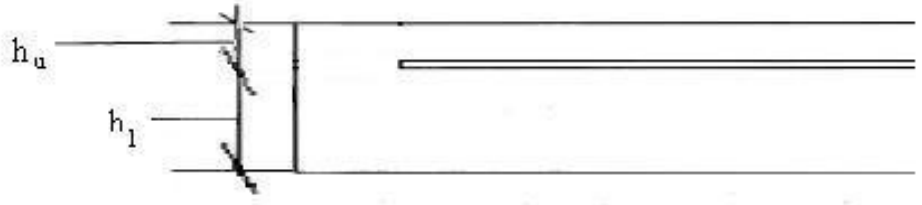


Figure 2.4 Diagram of sublaminates dimensions.

2.4 Perel-Palazotto Code

The theory and formulation of the Perel-Palazotto code is presented by Victor Perel¹⁶ (2003). This code only considers thin beams, which allows the assumption of negligible shear strains.

Hamilton's principle is used to derive the differential equations of motion with boundary conditions.

$$\delta \int_{t_1}^{t_2} J(t) dt = 0 \quad (2.34)$$

where $J(t)$ is a modified Lagrangian function based on the strain energy density and the kinetic energy density of the system. The latter two terms are described in terms of density as

$$\hat{T} = \frac{1}{2} \rho (\dot{u}^2 + \dot{w}^2) \quad (2.35)$$

$$\hat{U} = \frac{1}{2}\sigma_{xx}(u' + \frac{1}{2}(w')^2) \quad (2.36)$$

where u is the longitudinal displacement, and w is the transverse displacement. The nonlinear term $\frac{1}{2}(w')^2$ accounts for the longitudinal force resultants in the sublaminates.

The transverse displacement of the beam is assumed to have the form

$$w(x, z, t) = W_0(x, t) + D_\beta^\alpha(x)H_\gamma(z)[W_1(x, t) - W_0(x, t)] \quad (2.37)$$

where $W_0(x, t)$ is the transverse displacement at the center axis of the beam, $W_1(x, t)$ is the transverse displacement of the upper sublaminate in the delaminated region $\alpha < x < \beta$. The first term gives the transverse displacement for the undelaminated portions of the beam. $D_\beta^\alpha(x)$ is a unit step-function, which makes the second term zero in the undelaminated portions of the beam.

$$D_\beta^\alpha(x) = \begin{cases} 1 & \alpha < x < \beta \\ 0 & 0 \leq x \leq \alpha \text{ and } \beta \leq x \leq L \end{cases} \quad (2.38)$$

The Heaviside function influences the delaminated parts of the beam, and is dependent on the location along the thickness of the beam. In the lower sublaminate region, the Heaviside function zeroes the second term so that the transverse displacement of the lower sublaminate is $W_0(x, t)$.

$$H_\gamma(z) = \begin{cases} 0 & -\frac{h}{2} < z < \gamma \\ 1 & \gamma \leq z \leq \frac{h}{2} \end{cases} \quad (2.39)$$

Otherwise, in the upper sublaminate region, $W_1(x, t)$ is used for the transverse displacement.

In other words, the beam can be described by four regions of displacement, where

$$w(x, z, t) = \begin{cases} w_1(x, t) & \text{In the undelaminated part near the clamped end} \\ w_2(x, t) & \text{In the lower sublaminates} \\ w_3(x, t) & \text{In the upper sublaminates} \\ w_4(x, t) & \text{In the undelaminated part near the free end} \end{cases} \quad (2.40)$$

The boundary conditions imposed at either tip of the crack are equal transverse displacement and rotation for the upper sublaminates displacement, the lower sublaminates displacement, and the corresponding undelaminated part.

The crack faces are constrained to prevent interpenetration by accounting for a force that takes effect when the two crack faces touch. This constraint also uses the Heaviside function to zero the force when the crack is open, and to force the difference in displacement to zero when the crack is closed. Analytically, the force constraint is

$$f(w_2, w_3) = (w_3 - w_2) \left(\frac{1}{2} - \frac{1}{\pi} \arctan \frac{w_3 - w_2}{\varepsilon} \right) = 0 \quad (2.41)$$

where ε is some small number. The Lagrange multiplier of this contact forcing function is included in the modified Lagrangian function $J(t)$.

Based on Euler-Bernoulli beam theory and assuming no longitudinal displacement along the middle axis, the longitudinal displacement is

$$u(x, z, t) = -\frac{\partial w}{\partial z} z \quad (2.42)$$

For the finite element formulation, the displacement functions $W_0(x, t)$ and $W_1(x, t)$ are approximated by third degree Hermit polynomials.

$$W_0 = [N_1 \quad N_2 \quad N_3 \quad N_4] \begin{Bmatrix} W_0(0) \\ W_0'(0) \\ W_0(l) \\ W_0'(l) \end{Bmatrix} \quad (2.43)$$

$$W_1 = [N_1 \quad N_2 \quad N_3 \quad N_4] \begin{Bmatrix} W_1(0) \\ W_1'(0) \\ W_1(l) \\ W_1'(l) \end{Bmatrix} \quad (2.44)$$

where

$$N_1 = 1 - \frac{3\bar{x}^2}{l^2} + \frac{2\bar{x}^3}{l^3} \quad (2.45)$$

$$N_2 = \bar{x} - \frac{2\bar{x}^2}{l} + \frac{\bar{x}^3}{l^2} \quad (2.46)$$

$$N_3 = \frac{3\bar{x}^2}{l^2} - \frac{2\bar{x}^3}{l^3} \quad (2.47)$$

$$N_4 = -\frac{\bar{x}^2}{l} + \frac{\bar{x}^3}{l^2} \quad (2.48)$$

The elemental coordinates \bar{x} and l correspond to the x-coordinate of the left node of the finite element and the length of the element respectively. The displacements w and u and the strain are expressed in terms of the eight nodal parameters θ (derivation not shown for brevity).

$$w = [B_w]\{\theta\} \quad (2.49)$$

$$u = z[B_u]\{\theta\} \quad (2.50)$$

$$\varepsilon = z[B_\varepsilon]\{\theta\} + \frac{1}{2}\{\theta\}^T[\tilde{B}_\varepsilon]\{\theta\} \quad (2.51)$$

The elemental stiffness and mass matrices formulated in terms of the nodal parameters are

$$[k] = b \int_0^l \int_{-h/2}^{h/2} [B_\varepsilon]^T \frac{1}{\bar{S}_{11}} z^2 [B_\varepsilon] dz d\bar{x} \quad (2.52)$$

$$[m] = b \int_0^l \int_{-h/2}^{h/2} [B_u]^T \rho z^2 [B_u] dz d\bar{x} + b \int_0^l \int_{-h/2}^{h/2} [B_w]^T \rho [B_w] dz d\bar{x} \quad (2.53)$$

where ρ and \bar{S}_{11} are material properties. Ultimately, the finite element formulation for the strain energy and kinetic energy is

$$U = \frac{1}{2} \{\theta\}^T [k] \{\theta\} + U_{nq} \quad (2.54)$$

where U_{nq} is the nonlinear contribution of the longitudinal force resultants, and

$$T = \frac{1}{2} \{\dot{\theta}\}^T [m] \{\dot{\theta}\} \quad (2.55)$$

The contact forcing constraint formulated in terms of nodal parameters is

$$f_k = (\Theta_{4k-1} - \Theta_{4k-3}) \left(\frac{1}{2} - \frac{1}{\pi} \arctan \frac{\Theta_{4k-1} - \Theta_{4k-3}}{\varepsilon} \right) = 0 \quad (2.56)$$

where k is a global node number, and N is the total number of degrees of freedom of the system. The finite element system of equations is

$$[M] \{\Theta\} + [K] \{\Theta\} + \chi \{G\} + \{Q^{nl}\} = \{P\} \quad (2.57)$$

where

$[M]$ is the system mass matrix

$[K]$ is the system stiffness matrix

$\{Q^{nl}\}$ accounts for the nonlinear component of the strain density

$\chi \{G\}$ is a product of the penalty function method imposed on the constraints

$\{P\}$ is the force vector

The piezoelectric actuator introduces a time-dependent concentrated boundary condition. The boundary condition involves imposing upon the zone of the beam containing the actuator a time-dependent bending moment. To simplify, the bending moment is introduced in the forcing function, rather than the boundary conditions. The voltage is distributed evenly along the length of the actuator. The force imposed on the beam is calculated using the virtual work principle modified as

$$\begin{aligned}
& b \int_0^L \int_{-h/2}^{h/2} \frac{1}{S_{11}^e(z)} \varepsilon_{xx} \delta \varepsilon_{xx} dz dx + b \int_0^L \int_{-h/2}^{h/2+\tau} \frac{1}{S_{11}^p(z)} (\varepsilon_{xx} - d_{31} \frac{V}{\tau}) \delta \varepsilon_{xx} dz dx + \\
& + b \int_0^L \int_{-h/2}^{h/2} \rho^c (g + \ddot{w}) \delta w dz dx + b \int_0^L \int_{-h/2}^{h/2} \rho^p (g + \ddot{w}) \delta w dz dx + \\
& + b \int_0^L \int_{-h/2}^{h/2} \rho^c \ddot{u} \delta u dz dx + b \int_0^L \int_{-h/2}^{h/2+\tau} \rho^p \ddot{u} \delta u dz dx - \int_0^L q \delta w dx = \text{\textcircled{2.58}}
\end{aligned}$$

where V is the applied voltage across the piezoelectric patch, τ is the thickness of the piezoelectric patch, d_{31} is a matrix element characterizing the material properties of the piezoelectric patch, ρ^c is the density of beam material, ρ^p is the density of piezoelectric patch material, and q is the unit surface electric charge.

The finite element code for the piezoelectric patch and the delamination were integrated.

2.5 Theory Behind Laser Vibrometry

A laser doppler vibrometer is used to obtain the frequency response. For the system $m\ddot{x} + c\dot{x} + kx = f(t)$, assuming an under-damped system ($\zeta < 1$), the Lagrange transfer function is

$$\frac{X(s)}{F(s)} = \frac{1}{s^2 + 2\zeta\omega_n s + \omega_n^2} \quad (2.59)$$

The frequency response function is then

$$FRF(\omega) = \frac{X(j\omega)}{F(j\omega)} = \frac{\frac{1}{\omega_n^2}}{1 + 2\zeta(\frac{\omega}{\omega_n}) - (\frac{\omega}{\omega_n})^2} \quad (2.60)$$

The magnitude of the FRF is maximum at the resonant frequency

$$\omega_r = \omega_n \sqrt{1 - 2\zeta^2} \quad (2.61)$$

On lightly damped structures the resonant frequency, damping frequency, and natural frequency approach the same frequency.

If the vibration is periodic, the FRF can be obtained from the data of the response and excitation signals. The FRF at the available discrete frequencies is the ratio of the response component to the input component.

$$FRF(\omega) = \frac{X(j\omega)}{F(j\omega)} \quad (2.62)$$

The velocity and displacement of a moving object can be determined from back-scattered light. The displacement of the object's surface modulates the phase of the light wave.³ Shifts in the light frequency determine the velocity of the object's surface. The measurement beam from the interferometer in the scanning head is reflected from mirrors to a specified scan point on the test specimen. The back-scattered laser light interferes with the reference beam in the scanning head. A photo detector records the interference. A decoder in the vibrometer provides a voltage which is proportional to the velocity of the vibration of the test specimen parallel to the measurement beam. The voltage is digitized and processed as the vibrometer signal.

The sensor head contains a heterodyne interferometer. With the help of a Bragg cell, the interferometer generates a high-frequency carrier signal. The carrier signal is converted into two quadrature signals, I and Q , in a mixing process. This quadrature signal pair holds the same information as the carrier signal, but it is easier to process electronically because it lies in the base band. Ideally, the quadrature signals are sinusoidal, have the same amplitude, and are phase-shifted 90° apart. This relation means that the signals can be represented by a rotating pointer whose

angle of rotation is equal to the interferometric phase difference, $\Delta\phi$. The sense of rotation corresponds to the direction of movement of the test specimen. The phase difference is calculated by

$$I(\Delta\phi) = A \cos \Delta\phi \quad (2.63)$$

$$Q(\Delta\phi) = A \sin \Delta\phi \quad (2.64)$$

$$\Delta\phi = \arctan \frac{Q(\Delta\phi)}{I(\Delta\phi)} \quad (2.65)$$

The phase difference is proportional to the displacement x of the test specimen according to

$$\Delta\phi = \frac{4\pi\Delta x}{\lambda} \quad (2.66)$$

where λ is the laser wavelength. Finally, the Doppler frequency shift can be obtained as

$$\Delta f(t) = \frac{4u(t)}{\lambda} \quad (2.67)$$

where $u(t)$ is the velocity of the specimen. The phase and frequency demodulators in the interferometer recover the displacement and velocity time histories from the phase and frequencies of the received signal.

The processes behind the laser vibrometer hardware and software are described in the Polytec manual.¹ Periodic functions can be described in a series as a sum of trigonometric functions. Non-periodic functions can be described as an integral of trigonometric functions. The time signal recorded by the laser vibrometer can be split into a sum of vibrations at different frequencies through a Fourier transformation. Recorded data contains a discrete number of samples. The Polytec software uses the Fast Fourier Transformation to generate the corresponding frequency spectrum.

The Polytec software provides built-in alias suppression. Aliasing is a result of the following. Any signal above the Nyquist frequency will appear in the spectrum below the Nyquist frequency at the same interval from that frequency. Therefore,

the spectrum will appear to have more signal lines. For correct signal processing, $f_{sample} > 2f_{signal}$, where f_{sample} is the sampling frequency, and f_{signal} is the maximum signal frequency. Signals with frequencies $f_{signal} > \frac{f_{sample}}{2}$ generate artificial spectrum lines at frequencies $f_{alias} < \frac{f_{sample}}{2}$. This corruption of the spectrum is called the alias effect. To avoid aliasing, signal frequencies higher than $\frac{f_{sample}}{2}$ must be suppressed. To reject the alias, the vibrometer signal and reference signal are filtered digitally, requiring oversampling, and filtered analog to anti-alias filters. The digital filter attenuates frequencies above the bandwidth with a sharp cutoff, and the analog filter attenuates frequencies near the oversampling frequency. The time signal is sampled with an oversampling frequency which is four times bigger than the sampling frequency. In the upper 20% of the frequency response, the amplitude is already strongly attenuated.

$$\text{sampling frequency} = 2.56 \text{ Bandwidth} \quad (2.68)$$

The digital filters have a frequency response near the oversampling frequency and near multiples of the oversampling frequency.

Frequency domain averaging consists of computing the spectrum from each time trace by means of an FFT, and then obtaining the average spectrum by averaging all values at each frequency. Complex averaging will reduce noise that is not phase correlated to the input signal. This method of averaging can be used if the phase between the output and input signal is stable. Prior to complex averaging the software relates the phase of the vibrometer signal to that of the reference signal. Complex averaging consists of adding the real and imaginary parts of all the measurement values and then dividing the result by the number of measured values.

$$\bar{S} = \frac{1}{N} \sum_{n=1}^N S_n \quad (2.69)$$

$$\bar{S} = \frac{1}{N} \left[\sum_{n=1}^N \text{Re}(S_n) + i \sum_{n=1}^N \text{Im}(S_n) \right] \quad (2.70)$$

The coherence function is a measure of the power in the output signal caused by the input. If the coherence is 1, then all the output power is caused by the input. If the coherence is 0 then none of the output is caused by the input. Coherence values close to zero indicate a poor signal-to-noise ratio, whereas coherence close to one indicates a good signal-to-noise ratio. PSV first calculates the FFTs of all active channels. Then the auto power spectra (AP) for each channel and the cross power spectra (CP) for every possible combination of a vibrometer and reference channel are calculated.

$$AP_{ss} = S^* \times S \quad (2.71)$$

$$CP_{rv} = R^* \times V \quad (2.72)$$

$$CP_{vr} = V^* \times R = CP_{rv}^* \quad (2.73)$$

Where f is the frequency, S is the spectrum at any channel, V is the spectrum of a vibrometer channel (output), R is the spectrum of a reference channel (input) and * denotes the complex conjugate. Without averaging, the FRF is

$$FRF_{vr} = \frac{CP_{rv}}{AP_{rr}} = \frac{V}{R} \quad (2.74)$$

With averaging, the response functions H1 and H2 and the coherence function COH are calculated:

$$H1_{vr} = \frac{\bar{C}P_{rv}}{\bar{A}P_{rr}} \quad (2.75)$$

$$H2_{vr} = \frac{\bar{A}P_{vv}}{\bar{C}P_{vr}} \quad (2.76)$$

$$COH_{vr} = \frac{H1_{vr}}{H2_{vr}} \quad (2.77)$$

These response functions do not depend on the averaging mode because CP signals are always averaged in complex averaging mode, and AP signals are real. H1 and H2 can be used to estimate the FRF of the measured system. The phase of H1 and H2 is equal. H1 reflects noise in the reference signal. However, H2 is affected by noise in the vibrometer signal. With a large number of averages, H1 converges to a smaller value than the FRF and H2 converges to a larger value. Since the output noise is usually larger than the input, H1 is usually a better approximation because it is less sensitive to the output.

III. Experiment Setup and Procedure

The experiment was conducted in the Vibration Laboratory of the Air Force Institute of Technology at Wright-Patterson Air Force Base, Dayton, Ohio. This chapter describes the test specimen, support equipment, source of excitation, and data acquisition equipment and procedures.

3.1 Sample preparation

The test specimens were designed to be similar to those of the preceding thesis in order to allow direct comparison. The material selected for specimen manufacture was Al 2024-T3 because it was most abundant in the machine shop. In the earlier thesis, Reifsnnyder found residual stresses in the beams composed of this material from the coldworking process involved in manufacturing. However, the residual stresses were determined to have minimal effect on the beam dynamics for the notch lengths up to 16cm. The material properties for Al 2024-T3 are a modulus of elasticity of 73.084 GPa and a density of 2837.5 kg/m^3 .

The beams contain notches of lengths 4 cm, 8 cm, 12 cm, and 16 cm. The notches are located at the clamped end, at the free end, and in the middle and extend through the entire width of the beam. The length of the beam is 38.1 cm, of which 7.62 cm are clamped during the test, which leaves 30.48 cm of the beam that is actually observed. The width is 3.81 cm. Both the length and width of the beam match those of the preceding thesis. However, the thickness of the beams containing the eccentric notches is 0.635 cm, twice that of the beams containing centralized notches. The notches within the beam were manufactured using an electrical discharge machining (EDM) cutting wire, which required the drilling of a 1/6-cm starter hole. A smaller hole greatly increased the likelihood of snapping the drill bit off inside the specimen. Since the notch was cut off-centered, halfway between the center of the beam and one edge, the starter hole mandated a thicker beam. The beam

containing the 4 cm notch located in the middle was manufactured incorrectly and included extra clamp holes at the free end.



Figure 3.1 Beams containing eccentrically located notches.



Figure 3.2 Beam containing additional holes.

The EDM process is performed by passing a ultra-high current through a thin wire to burn away material. The cutting area is constantly flooded by a liquid coolant (in this case water) to avoid thermal conduction from the wire to areas of material beyond the immediate cut. The specimens for this study contained notches with widths of 0.31 mm, which was the smallest width achievable by the EDM machine used. Cawley and Ray found that increasing notch width had profound effects on the variations in natural frequency. Therefore, they concluded "it is desirable to use the narrowest available cutter." However, a thinner notch increases the probability of notch surface contact during vibration.

A piezoelectric transducer was affixed to one of the notchless beams. With one beam for each combination of notch length and location, and two notchless beams, the total number of beams is 14.

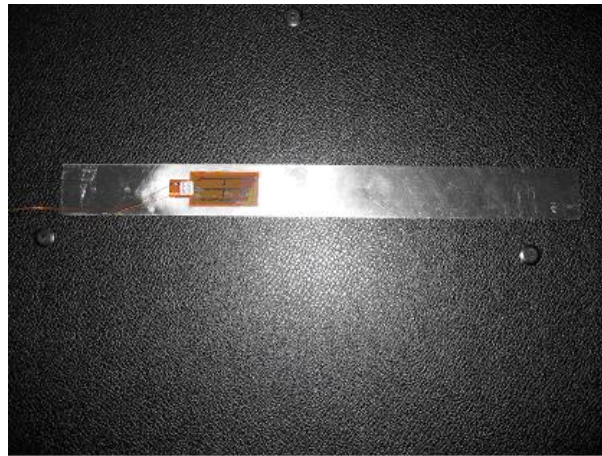


Figure 3.3 Beam with piezoelectric actuator affixed.

3.2 Support system

The beam was clamped to a stainless steel Newport Research Corporation Model 45 cylindrical test stand. The test stand was affixed through two socket head

cap screws to a Newport Research Corporation Model 100 magnetic base to provide a rigid connection. The magnetic base secured the test stand to a pneumatic shaker table. The clamp was tightened using four socket head cap screws. The screws were tightened equally so that the beam was aligned flush with the clamping plate. In reality the beam cannot be perfectly clamped, but the errors should be negligible. The end of the beam must be flush with the edge of the clamp. Two holes in the clamped section of the beam correspond to two pegs in the clamp, which ensured the proper placement of the beam within the clamp.

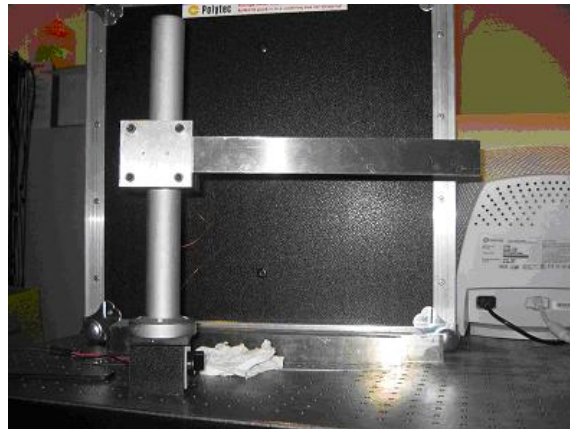


Figure 3.4 Test support setup.

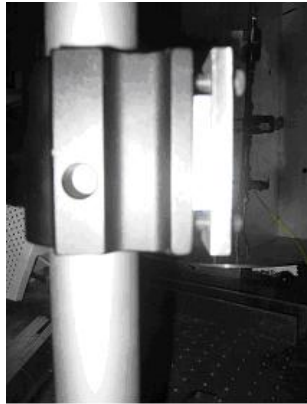


Figure 3.5 Properly clamped beam flush with clamp.

The vertical support was inspected to ensure that the test stand did not introduce vibrations or deflections that would alter the measurements. The maximum deflection, which would occur at the upper end of the vertical support was calculated by

$$p(L) = -\frac{PL_{cyl}^3}{3EI} \quad (3.1)$$

where P is the force, L_{cyl} is the height of the test stand, E is the modulus of elasticity, and I is the moment of inertia. The height of the test stand is 15 inches. The force was derived from the acceleration of the beam measured by the laser vibrometer. Using the largest acceleration measured and the mass of the unclamped beam, the maximum force was determined to be 255 kN. Thus the maximum end displacement of the test stand was 1 mm.

3.3 Excitation

The beam was excited by an Atlas Sound PD-60T acoustic horn. The horn was also affixed to a Newport Research Corporation Model 100 magnetic base, which eliminated base motion. The horn was placed behind the beam, at a 5mm distance from the beam in the center of the beam width, as can be seen in Figure 3.8. An off-centered excitation would introduce torsion moments, and disguise the bending moments in the FRF. The horn excited the beam in the center 23 mm from the clamped end. The horn was pointed directly perpendicular to the beam. The excitation signal was computed by the Polytec software program and passed through a 220 DN Bogen amplifier.



Figure 3.6 Acoustic horn.



Figure 3.7 220 DN Bogen amplifier.

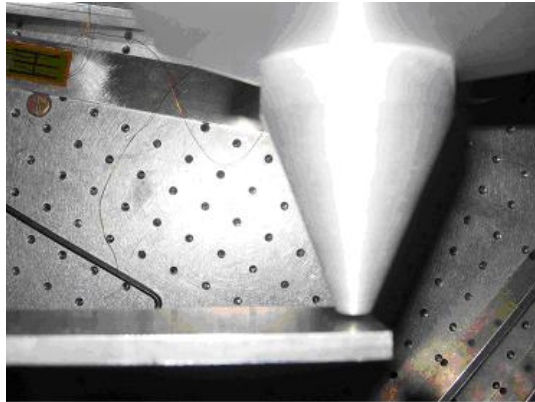


Figure 3.8 Distance of acoustic horn from beam.

A notchless case using a piezoelectric actuator was also prepared. A description of the attachment of the piezoelectric actuator is available in Reifsnyder (2004). The piezoelectric patch was placed centered on the beam to avoid introducing torsional moments, at the same location as in the experiments conducted by Reifsnyder.



Figure 3.9 ACX Quick Pack Power Amplifier Model EL 1224.

3.4 Laser Doppler Vibrometer

The laser Doppler vibrometer measures the velocity of the beam. The laser vibrometer system consists of the "TOP", "LEFT", and "RIGHT" Polytec PSV-400 Scanning Head supported by 3051 Manfrotto Tripods, the three corresponding Polytec OF V-5000 Vibrometer Controller, and the Polytec PSV-E-400-3D Junction Box. The scanning head must be aligned with the help of its built-in level so that the path of the laser is parallel to the floor. The laser should hit the beam as straight on as possible. The tripod legs are adjusted so that the beam is level in the camera view of the laser. The scanning head is positioned at the proper height by adjusting the tripod.

The vibrometer controller receives a high-frequency Doppler signal from the sensor head. The initial stage is a high-frequency stage in which the measurement signal is optimally conditioned. Then in the decoder stage the velocity information is recovered from the signal. The final stage, the low-frequency stage consists of an analog filter module and a digital interface.

3.5 Hardware Arrangement

The cylindrical test stand was tightly attached to the magnetic base using two cap screws. The clamp pegs were inserted into the two holes in the chosen beam. The four cap screws were tightened equally using an allen wrench to provide a fixed boundary condition. The stand was then placed so that the largest surface of the beam was facing the area where the laser vibrometer setup was established, and the magnet was set in the arrest position.

The acoustic horn was also affixed to a magnetic base using two cap screws. The horn center was positioned at the height of the middle of the beam width. The horn was connected to the output channel of the amplifier. For the test case in which the source of excitation was the piezoelectric actuator, an ACX Quick Pack Power Amplifier Model EL 1224 was used to amplify the generator signal. Switches on the amplifier were set to a voltage limit of 200V and a current limit of 200mA. The amplifier was placed on a chair separated from the table, to prevent added vibrations from the internal cooling fan. Alligator clips leading from the amplifier output channel connected to the prongs of the piezoelectric actuator.

A signal cable, through which the generated signal passed, ran from the signal output channel of the vibrometer junction box to the input channel of the amplifier. The generated signal was also connected to an input channel of the junction box, to provide the reference signal to the software. Signal cables ran from all three vibrometer control outlets to input channels in the junction box.



Figure 3.10 Acoustic horn position.

Although the three-dimensional scanning was not utilized, all three vibrometer controllers and scanning heads had to be turned on. For one-dimensional measurements, the “top” laser vibrometer was used. The laser vibrometer was connected to the rest of the data acquisition system through the junction box. The laser vibrometer was positioned so that the scanning head line of sight was perpendicular to the test specimen. The height of the tripod was adjusted so that the scanning head was level with the center of the test specimen and the laser beam was perpendicular to the plane of the test specimen.

3.6 Software preparation

The software Polytec 8.2 performed the data acquisition of the laser vibrometer. The following steps were followed to prepare the software for acquisition. With the test apparatus centered in the camera view, the laser beam was moved to a corner of the view to avoid interference and the camera was then focused on the test specimen. The laser beam was then repositioned on the beam and properly focused. The plane of the beam was defined. The laser was moved to at least four

positions on the beam in the camera view and the positions were recorded. These four readings by the laser were used to create a plane of reference. The scan points were then defined by creating a grid over the beam in the camera screen. Proper alignment could be verified by confirming the laser beam moved to the appropriate position at the center of the scan point when a scan point was selected in the camera view.

Each beam was tested using one-dimensional and two-dimensional grids. The one-dimensional grid avoids measuring much of the torsion, but the two-dimensional grid measures the torsion and helps to determine when the torsion is interfering with the measurements. The one-dimensional grid consisted of one line of grid points along the center of the beam. It was important to center the grid points to avoid including measurements due to torsional moments. The grid points numbered 30 for the coarsest grid. The grid was refined up to 62 points when considered necessary to obtain an accurate mode shape. For the two-dimensional grid, three grid points were placed across the beam. The vibrometer signal level was observed at several grid points to confirm a sufficient signal amplitude, or signal-to-noise ratio, for measurement.

The following factors were set in preparation for acquisition. The acquisition mode was Fast Fourier Transform (FFT) to process the beam velocity with respect to frequency. The averaging was complex and the software was set to remeasure data points of poor response signal. The upper limit of the frequency range was set to 8 kHz or 10 kHz, the lowest frequency range that captured the 8th mode. The window is "rectangle" so no samples were removed. Twenty samples were attempted at each data point and averaged. The number of samples processed by the FFT had to be a power of two. The velocity of the vibrometer was set at 2 mm/s/V. The tracking filter used was fast. The generator, which controlled the output of the acoustic horn, was pseudo-random with amplitude of 1V. For the test involving the piezoelectric actuator, the voltage used was 2V. Pseudo-random is a periodic signal, which has no

leakage and is best for fast measurements of complete spectra since all frequencies are excited simultaneously.

3.7 Analysis

The modal analysis used is the peak-amplitude method with the assumption that in the vicinity of a resonance the total response is dominated by the contribution of the mode whose natural frequency is closest. This method works when the structure is appropriately damped. If the structure is too heavily damped the resonant frequencies will be influenced by more than one mode, which violates the assumption required for this method.

The peak-amplitude method of analysis was performed as follows. The resonance peaks were picked from the FRF plot and the frequency of each peak was taken as the natural frequency of the corresponding mode. This study investigated only the bending modes. Therefore, the modal shapes at each peak were analyzed to discover whether the peak represented a bending mode or a torsional mode. This method assumed that the mode shapes of the damaged structure were close to the corresponding mode shapes of the intact structure. The classical modal shapes that indicate a bending mode are shown.

IV. Results and Discussion

4.1 Abberations in the FRF plots and Mode Shapes

The acoustic horn was originally positioned at the clamped end, 25 mm from the clamp, which was the closest to the clamp the acoustic horn could be positioned without touching the support equipment. However, when the mode shapes were analyzed, some of the beams were missing a mode and some of the mode shapes indicated interference. This interference was thought to be caused by the acoustic horn. The absence of a mode may be due to the position of the acoustic horn. If the excitation coordinates coincides with a node for one of the modes, then that mode will not appear as a resonance on the FRF plot. Since it is a node, the only response that will be encountered at that modal frequency will be due to the off-resonant contribution of all the other modes.¹¹ Further testing was performed with the acoustic horn positioned in the middle of the beam and 5 mm from the free end. None of the modes have nodes that are located at the free end location of the acoustic horn. Therefore, the free end positioning of the horn did not result in the absence of any resonant peaks. Also the grids were refined from 30 grid points up to 62.

The FRF plots produced by the acoustic horn in the three positions for the same beam reveal some influence of the excitation position on the amplitude. For example, the beam containing an 8-cm notch at the clamped end contained interference in the eighth mode, as can be seen in Figure 4.1. The FRF plots for the three acoustic horn positions for the 12-cm clamped-end notched beam are displayed in Figure 4.2.

The amplitude of the fourth mode is significantly diminished with the horn located at the middle. The peaks in the frequency range of 3000 through 6000 Hz are also reduced in amplitude for the mid-bar horn. The fifth modal peak with the horn located at the clamped end is reduced in amplitude. The eighth mode was

better captured by locating the horn at the free end. The eighth modal shape with the horn located at the free end is displayed in Figure 4.3.

A piezoelectric patch was then attached to a notchless beam. The FRF plot of the notchless case excited by the piezoelectric patch revealed clear resonance peaks.

The encircled peaks in Figures 4.4 and 4.5 are the first seven modal frequencies. The peaks of the acoustic horn FRF are less clear. More bumps appear in the horn FRF than in the PZT FRF. The horn FRF also contains noise in the extremely low amplitudes and in the frequency region of 7000 to 8000 Hz. This noise is common to all the beam cases in the FRF. The modal frequencies that fall within this region are difficult to pick out. The deviation between the modal frequencies obtained from the horn and the piezoelectric actuator are displayed in Table 4.1.

Although the peaks may be more difficult to distinguish for the acoustic horn, the modal peaks can still be determined by using the appropriate modal shapes. As the table shows, the resulting modal frequencies of the notchless beam tested with the acoustic horn and the notchless beam tested with the piezoelectric actuator differ by less than 2%, and differ much less than that for many of the modes. However, the third mode deviates significantly more than the other modes. Note that in both FRFs two peaks occur around the third mode. The mode shapes of these two peaks for the acoustic horn FRF are similar. The corresponding modal frequencies are

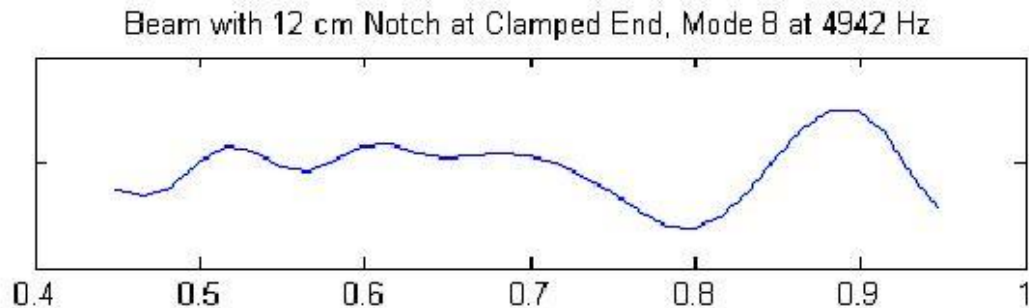


Figure 4.1 Eighth modal shape of beam containing 12-cm notch at clamped end, excited by acoustic horn at clamped end.

Acoustic Horn at Clamped End	Piezoelectric Actuator	Error
52.92	53.13	-0.40%
330.9	328.1	0.84%
1053	996.9	5.33%
1869	1869	0.02%
3093	3063	0.96%
4590	4588	0.04%
6306	6309	-0.04%
8450	8297	1.81%

Table 4.1 Modal frequencies of notchless beam with different excitation sources.

828.1 Hz and 1053 Hz. The discussion that follows will show some large variations of the modal frequencies of the test cases from the notchless case in the third mode. This enlarged variation may be due to the possibility that the third mode is not captured and is actually between these two peaks.

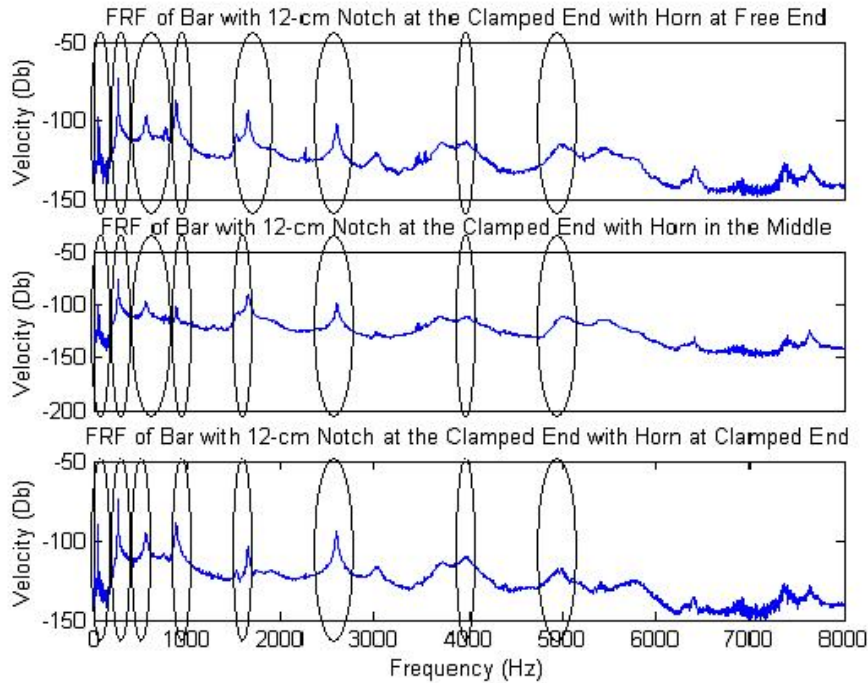


Figure 4.2 FRF plots of beam with 12-cm notch located at the clamped end, excited by horn at three locations.

Damping causes the peaks to decrease in amplitude. However, the piezoelectric actuator is affixed to the test specimen and will add a small damping effect, whereas the horn does not touch the test specimen and therefore should not cause notable damping. By this reasoning, if any change in amplitude is seen, the peaks of the piezoelectric actuator FRF plot should be slightly lower.

The smeared peaks are more likely due to interference from the excitation. The acoustic horn may increase the amplitudes of the torsional modes if it is positioned slightly off-centered, or if the acoustic vibration from the mouth of the horn is not symmetric. The mode shapes of the final modal frequencies chosen are plotted in Appendix B.

4.2 Changes in Natural Frequency

The resonant frequencies of the thicker notchless beam excited by the acoustic horn are displayed in Table 4.2. The theoretical results are calculated using the analytical approach briefly described in Chapter II.

The experimental modal frequencies are approximately 4% to 6% less than the theoretical modal frequencies, which means the experimental beam has a lower stiffness than the theoretical case, which is expected. The exception is the third

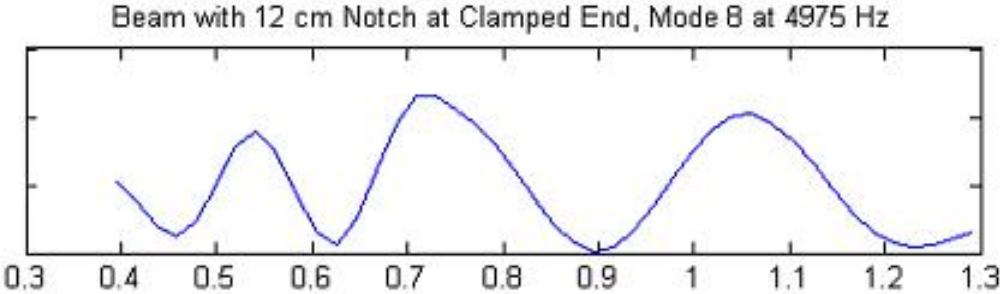


Figure 4.3 Eighth modal shape of beam containing 12 cm notch at clamped end, excited by horn at free end.

Theoretical	Experimental	Error
56.31	52.92	6.02%
352.9	330.9	6.24%
988.2	1053	-6.55%
1937	1869	3.47%
3201	3093	3.38%
4782	4590	4.01%
6678	6306	5.57%
8892	8450	4.97%

Table 4.2 Comparison of theoretical and experimental modal frequencies for the notchless case.

mode, which appears to have an almost 7% greater stiffness. This aberration is most likely due to the problem noted above, in finding the third mode on the FRF plot for the notchless beam.

The first eight modal frequencies for each beam containing an eccentric notch are shown in Table 4.3. The table also shows the percent change from the notchless case, calculated with respect to the notchless frequency.

$$\% \text{ change} = \frac{(\text{Modal frequency of notched beam}) - (\text{Modal frequency of notchless beam})}{(\text{Modal frequency of notchless beam})} \times 100\% \quad (4.1)$$

For each notch location and mode, as the notch length increases, the modal frequency decreases. The two exceptions are the fifth modal frequency of the 12-cm notch

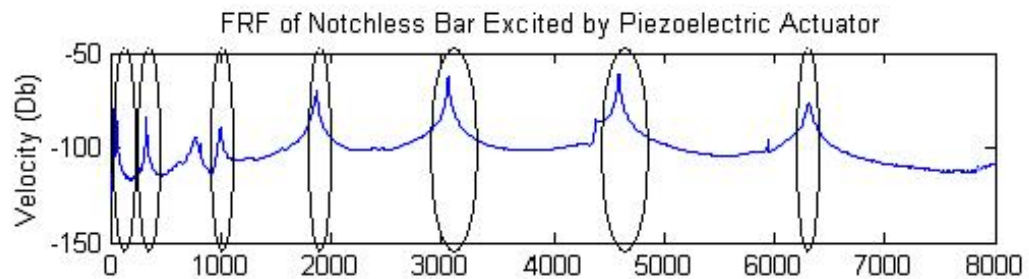


Figure 4.4 FRF plot of notchless beam excited by piezoelectric actuator.

located in the middle is larger than the fifth modal frequency of the 8-cm notch located in the middle, and the fourth modal frequency of the 8-cm notch located in the middle is larger than the fourth modal frequency of the 4-cm notch located in the middle. The modal shapes of the exceptions are examined in Figures 4.6 and 4.7.

The interference can be recognized by comparison of the experimental mode shapes to the classical mode shapes. Significant interference is apparent in the fourth and fifth modal shapes of the 8-cm mid-notched beam. The interference in the fourth mode is visible by the additional maximum at the location $\frac{x}{L} = 0.7$, whereas in the classical fourth mode shape, a minimum occurs. In the fifth mode, the first sine curve is not smooth, and the first two nodes are moved closer together. The interference in both these mode shapes occurs at the notch location. This interference may be a result of the notch upper sublaminar and lower sublaminar vibrating at different frequencies, since they are of different thicknesses, and thereby instigating contact.

In order to be able to detect a 4-cm notch, the accuracy of the measurement system would have to be less than 5%, if only the first eight modes are observed. Damage is easily detectable in the 8-cm clamped-end notched beam and in the 12-cm and 16-cm notched beams, where the natural frequency deviates from the reference case by more than 20%.

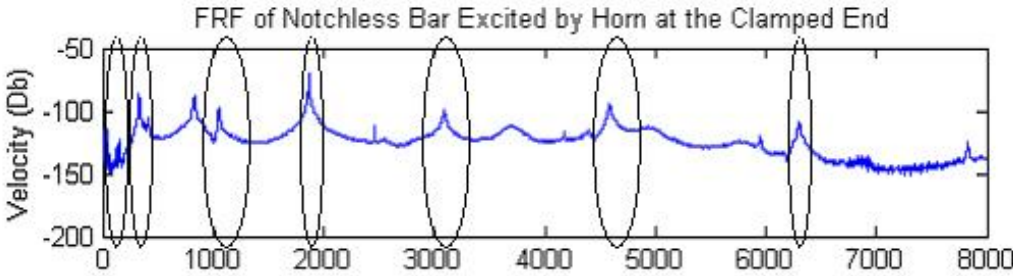


Figure 4.5 FRF plot of notchless beam excited by acoustic horn at clamped end.

	EXPERIMENTAL MODAL FREQUENCIES							
	Deviation from notchless beam (%)							
Mode	1	2	3	4	5	6	7	8
Notchless	52.92	330.9	1053	1869	3093	4590	6306	8450
Free End								
4-cm	52.81 0.21%	328.1 0.84%	1009 4.18%	1828 2.21%	2972 3.90%	4322 5.84%	6178 2.03%	8134 3.74%
8-cm	52.50 0.79%	325.0 1.77%	987.5 6.22%	1731 7.40%	2903 6.14%	3966 13.59%	5481 13.08%	6881 18.57%
12-cm	52.50 0.79%	306.3 7.42%	942.5 10.49%	1666 10.88%	2291 25.92%	2550 44.44%	3700 41.33%	5023 40.56%
16-cm	47.50 10.24%	295.0 10.84%	352.5 66.52%	857.5 54.13%	1485 51.98%	2400 47.71%	2805 55.52%	3738 55.76%
Middle								
4-cm	51.88 1.97%	331.3 -0.13%	812.5 1.96%	1853 0.87%	2887 6.66%	4309 6.12%	5844 7.33%	8159 3.44%
8-cm	50.94 3.74%	328.1 0.84%	775.0 6.48%	1878 -0.46%	2459 20.49%	4013 12.57%	5744 8.92%	7703 8.84%
12-cm	50.31 4.93%	317.5 4.04%	710.0 14.33%	1638 12.38%	2678 13.41%	3850 16.12%	5473 13.21%	7308 13.51%
16-cm	50.00 5.52%	293.8 11.20%	631.3 23.82%	906.3 51.52%	985 68.15%	1819 60.37%	2865 54.57%	3766 55.43%
Clamped End								
4-cm	50.94 3.74%	318.2 3.83%	955.7 9.24%	1747 6.60%	2858 7.59%	4212 8.24%	6279 0.43%	8169 3.33%
8-cm	50.63 4.33%	296.9 10.27%	871.9 17.20%	1747 6.54%	2850 7.85%	3760 18.08%	4031 36.08%	5725 32.25%
12-cm	49.38 6.69%	267.5 19.15%	575.5 45.35%	880 52.92%	1650 46.65%	2593 43.51%	3960 37.21%	4975 41.12%
16-cm	52.50 0.79%	242.5 26.71%	352.5 66.52%	857.5 54.13%	1485 51.98%	2400 47.71%	2805 55.52%	3738 55.76%

Table 4.3 Experimental modal frequencies for the beams containing eccentrically located notches.

The modal frequencies of the beams containing notches located at the free end are plotted against mode number in Figure 4.8, the modal frequencies of the beams containing notches located in the middle are plotted in Figure 4.9, and the modal frequencies of the beams containing notches located at the clamped end are plotted in Figure 4.10. Polynomial least-square curve fits are generated and the

curve-fit equations are displayed for each case. A power least-square curve fit was deemed appropriate for the 8-cm notch located at the clamped since it contained the erroneous frequencies and was not represented well by a polynomial equation.

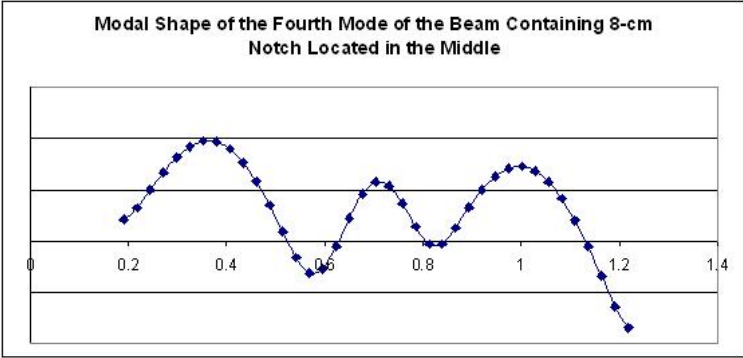


Figure 4.6 Fourth modal shape of beam containing 8-cm notch in the middle.

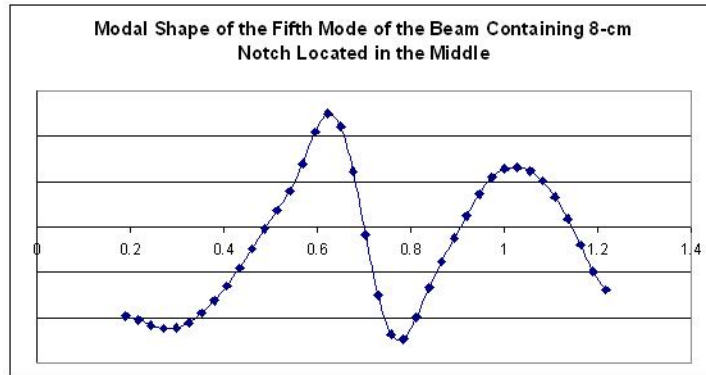


Figure 4.7 Fifth modal shape of beam containing 8-cm notch in the middle.

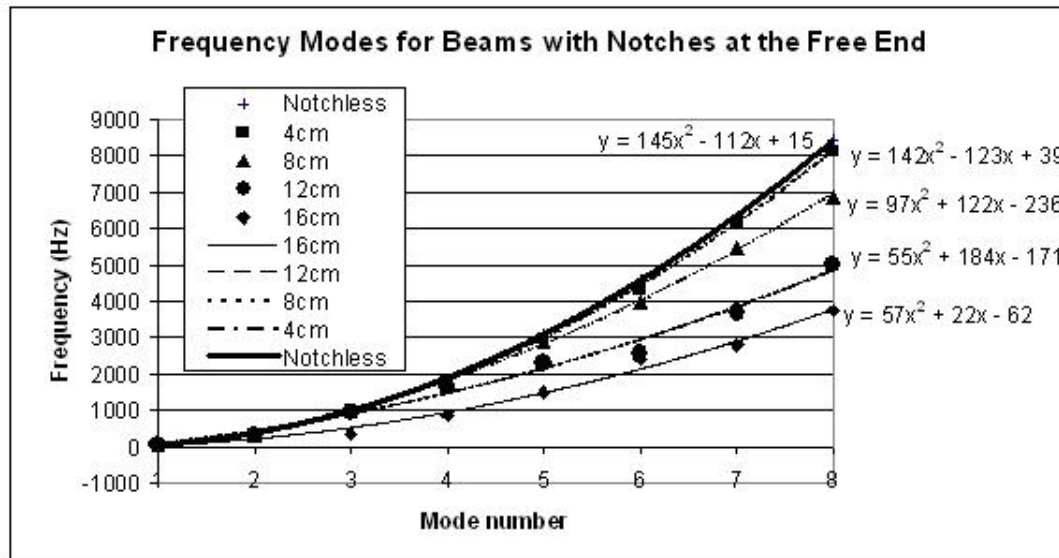


Figure 4.8 Frequency modes of beam containing eccentrically located notch at the free end.

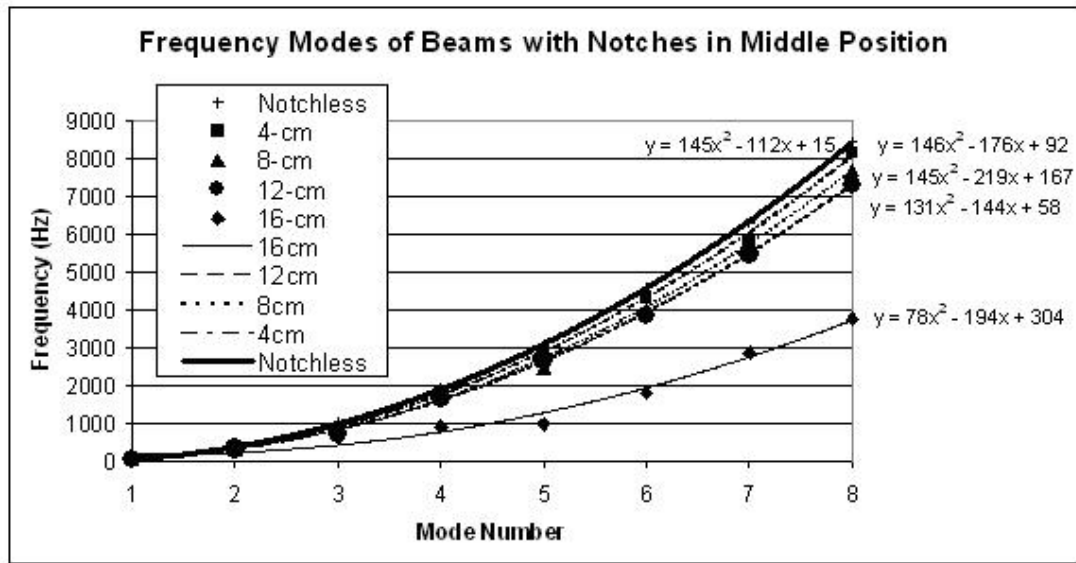


Figure 4.9 Frequency modes of beam containing eccentrically located notch in the middle.

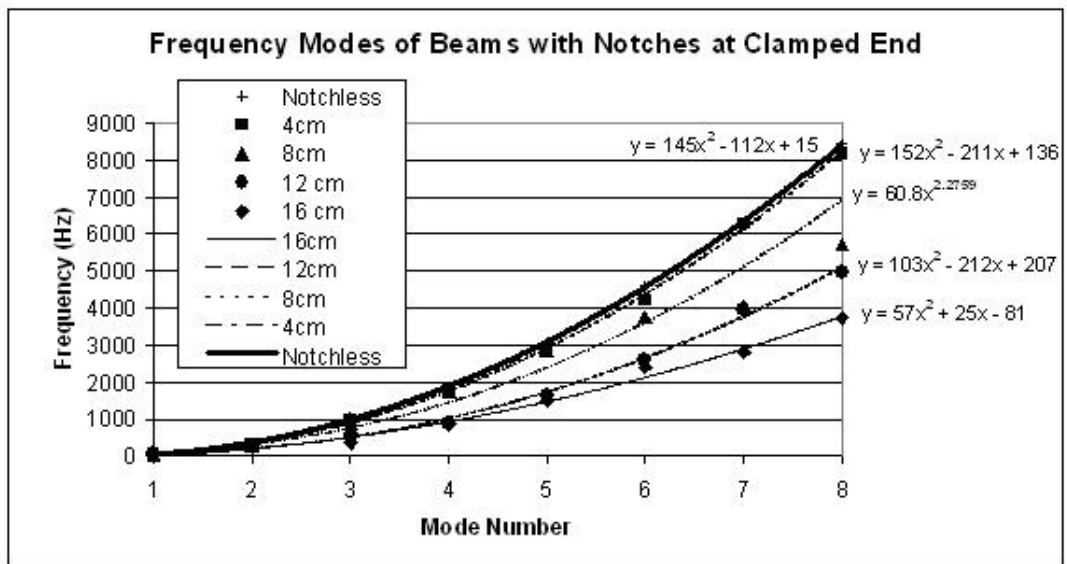


Figure 4.10 Frequency modes of beam containing eccentrically located notch at the clamped end.

The notch size may be determined from the natural frequency deviation from the notchless case. The beams containing notches located at the free end are shown in Figure 4.8. The 12-cm and 16-cm notched beams are individually distinguishable at modes 4 and higher. The 8-cm notched beam begins to deviate notably from the notchless beam and the 4-cm beam at mode 6. The notches located at the clamped end display characterizable behavior. The 4-cm notched beam does not appear to deviate a large amount in natural frequencies from the notchless case. However, the 8-cm, 12-cm, and 16-cm notched beams display a linear proportionality between natural frequency deviation from the notchless case and length of notch and appear distinguishable at mode 4 and higher modes. The 4-cm notched beam here also does not appear to be discernable from the notchless beam. The beams containing notches in the middle display a different behavior. Only the longest notch is discernable from the other cases. A notch located eccentrically in the middle of the beam is difficult to size properly.

In Table 4.4, the deviation from the notchless case of the modal frequencies calculated from the curve fits of the experimental data are displayed. The percent deviation is calculated with respect to the notchless case, by Equation (4.1). Modes four and higher are shown, since the lower modes do not show discernable behavior as stated previously, and the curve fits are dominated by the larger frequencies.

In the case of 4-cm notched beams, the percent deviation is small. Therefore, the differences in percent deviation between the different locations are not significant, although the free end notch produces a lower deviation than the others for modes four through seven. In the case of 8-cm notched beams, deviation of the clamped-end notch is significantly higher than the free-end and middle notches in modes four and five. In modes seven and eight, the percent deviation of the clamped-end and the free-end notches is equivalent, whereas the percent deviation of the middle notch is significantly lower.

CURVE-FIT MODAL FREQUENCIES					
Eccentrically notched beams					
Deviation from notchless beam (%)					
Mode	4	5	6	7	8
Notchless	1887	3080	4563	6336	8399
Free End					
4-cm	1819 3.60%	2974 3.44%	4413 3.29%	6136 3.16%	8143 3.05%
8-cm	1804 4.40%	2799 9.12%	3988 12.60%	5371 15.23%	6948 17.28%
12-cm	1445 23.42%	2124 31.04%	2913 36.16%	3812 39.84%	4821 42.60%
16-cm	938.0 50.29%	1473 52.18%	2122 53.50%	2885 54.47%	3762 55.21%
Middle					
4-cm	1724 8.64%	2862 7.08%	4292 5.94%	6014 5.08%	8028 4.42%
8-cm	1611 14.63%	2697 12.44%	4073 10.74%	5739 9.42%	7695 8.38%
12-cm	1578 16.38%	2613 15.16%	3910 14.31%	5469 13.68%	7290 13.20%
16-cm	776.0 58.88%	1284 58.31%	1948 57.31%	2768 56.31%	3744 55.42%
Clamped End					
4-cm	1724 8.64%	2881 6.46%	4342 4.84%	6107 3.61%	8176 2.66%
8-cm	1426 24.43%	2370 23.06%	3588 21.36%	5096 19.56%	6906 17.77%
12-cm	1007 46.63%	1722 44.09%	2643 42.08%	3770 40.50%	5103 39.24%
16-cm	931.0 50.66%	1469 52.31%	2121 53.52%	2887 54.43%	3767 55.15%

Table 4.4 Modal frequencies obtained from the least-squares curve-fit of the experimental data of the eccentrically notched beams.

The 12-cm notches also display discernable trends in the location of the notches. The frequency percent deviations of the free-end and clamped-end notches are significantly greater than the middle notch percent deviations for all five modes. In the fourth and fifth modes, the free-end 12-cm notch differs from the clamped-end notch

by 30% to 50%. In the case of the 16-cm notch, the middle notch percent deviation is greater than that of the free-end and clamped-end notches by more than 5% in the fourth and fifth modes.

To establish the size of the notch, the sixth modal frequencies are investigated. If the deviation of the modal frequency from the notchless case is between 3% and 6% then the notch is 13% of the beam length. If the deviation of the modal frequency is between 10% and 20% then the notch is at least 26% of the beam length. The notch could also be 39% of the beam length if it is located in the middle. If the deviation of the modal frequency is between 35% and 45% from the notchless case then the notch is 39% of the beam length. If the deviation is between 50 and 60% then the notch is over 50% of the beam length. These trends are presented graphically in Figures 4.11 through 4.14.

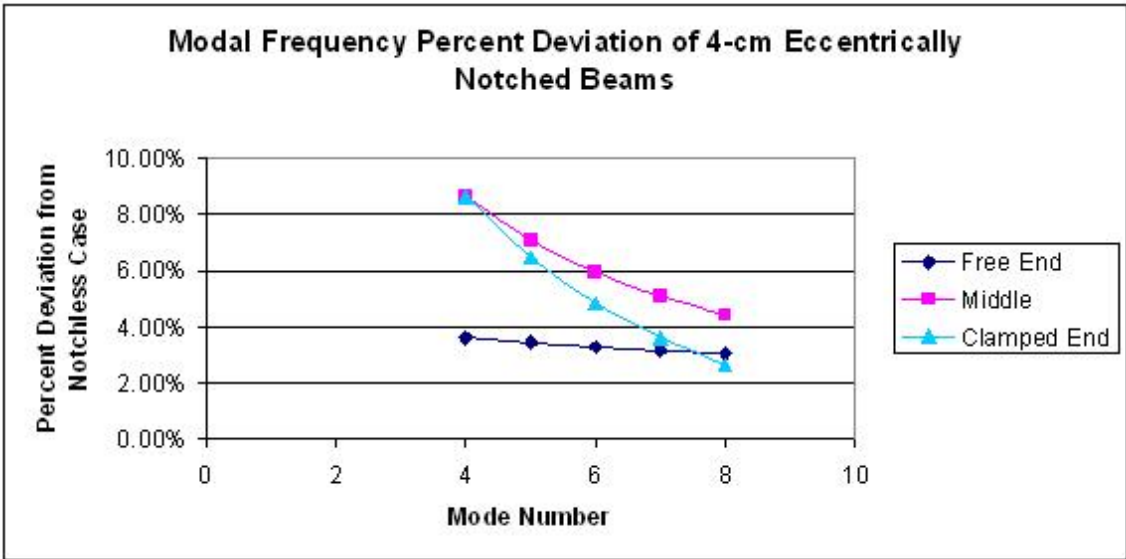


Figure 4.11 Modal frequency percent deviation of 4-cm eccentrically notched beams.

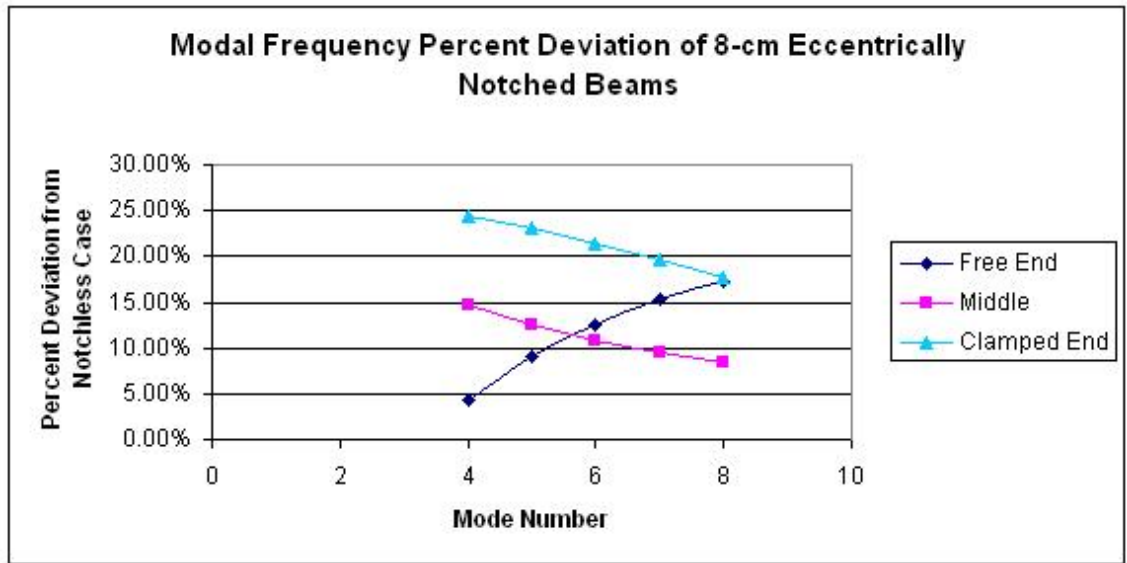


Figure 4.12 Modal frequency percent deviation of 8-cm eccentrically notched beams.

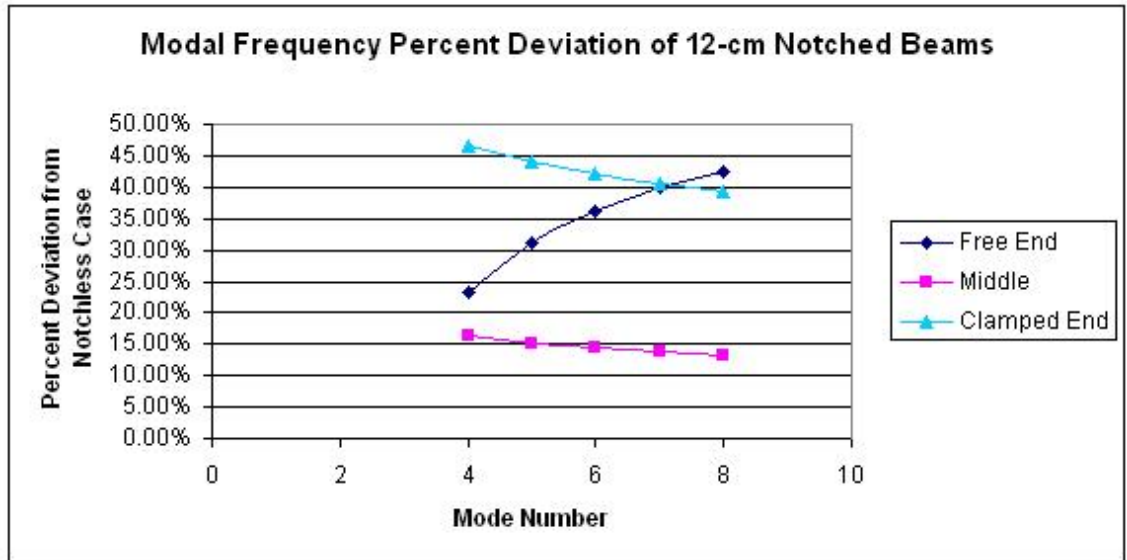


Figure 4.13 Modal frequency percent deviation of 12-cm eccentrically notched beams.

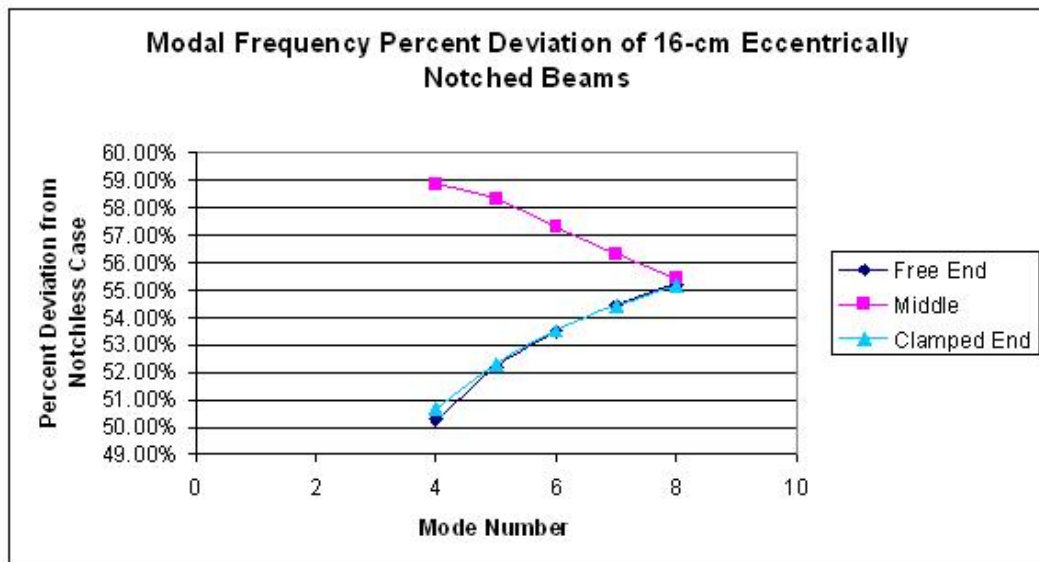


Figure 4.14 Modal frequency percent deviation of 16-cm eccentrically notched beams.

4.3 Comparison with Beams Containing Centered Notches

These results correspond with the modal frequency trends of the beams containing the centralized notch discussed by Reifsnnyder.¹⁸ In order to be able to compare the beams of different thicknesses, the modal frequencies are normalized using the corresponding modal frequencies of the notchless beam of the appropriate thickness. For the case of the beam containing an 8 cm notch at the clamped end, the results for the Al 2024 O case are displayed with a 3% correction factor to account for the residual stresses within the Al 2024 T3 beams. Again, the percent deviation is calculated using Equation (4.1).

The ratio for the notchless case presented in Table 4.5 is the eccentrically notched beam frequency divided by the centrally notched beam frequency. The theoretical natural frequency for a simple lump mass is

$$\omega = \sqrt{\frac{k}{m}} \quad (4.2)$$

where k is the stiffness and m is the mass of the structure. The stiffness is a function of the moment of inertia I , which is found using Equation (2.5). Since the thickness of the beam containing the centered notch is half that of the beam containing the eccentric notch, the moment of inertia of the former is one eighth that of the latter. On the other hand, since the beams are isotropic and the same material, the mass of the centrally notched beam is half that of the eccentrically notched beam. Therefore, the ratio of the natural frequencies of the notchless beams is

$$\frac{\omega_e}{\omega_c} = \sqrt{\frac{\frac{1}{8}}{\frac{1}{2}}} = 2 \quad (4.3)$$

The experimental ratios, which are shown for the notchless case in Table 4.5, are found to be approximately 2, as well.

		EXPERIMENTAL MODAL FREQUENCIES							
		Normalized with notchless beam							
Mode		1	2	3	4	5	6	7	8
Notchless	Eccentric	52.92	330.9	1053	1869	3093	4590	6306	8450
	Centered	28.09	172.4	484	945	1566	2342	3268	4359
	Ratio	1.88	1.92	2.18	1.98	1.98	1.96	1.93	1.94
Free End									
4-cm	3.81x0.64x30.5 (eccentric)	0.998	0.992	0.958	0.978	0.961	0.942	0.980	0.963
	3.81x0.32x30.5 (centered)	1.029	1.016	0.974	0.986	0.948	0.945	0.954	0.952
	% Difference	-3.13%	-2.50%	-1.69%	-0.85%	1.30%	-0.37%	2.66%	1.08%
8-cm	3.81x0.64x30.5 (eccentric)	0.992	0.982	0.938	0.926	0.939	0.864	0.869	0.814
	3.81x0.32x30.5 (centered)	1.043	0.968	0.871	0.820	0.868	0.760	0.775	0.798
	% Difference	-5.14%	1.44%	7.13%	11.49%	7.47%	12.07%	10.80%	2.06%
12-cm	3.81x0.64x30.5 (eccentric)	0.992	0.926	0.895	0.891	0.741	0.556	0.587	0.594
	3.81x0.32x30.5 (centered)	1.034	0.895	0.839	0.697	0.696	0.747	0.725	0.699
	% Difference	-4.21%	3.34%	6.24%	21.83%	5.99%	-34.37%	-23.57%	-17.63%
16-cm	3.81x0.64x30.5 (eccentric)	0.898	0.892	0.335	0.459	0.480	0.523	0.445	0.442
	3.81x0.32x30.5 (centered)	1.006	0.851	0.695	0.594	0.668	0.655	0.693	0.631
	% Difference	-12.08%	4.53%	-107.71%	-29.55%	-39.18%	-25.35%	-55.75%	-42.60%
Middle									
4-cm	3.81x0.64x30.5 (eccentric)	0.980	1.001	0.980	0.991	0.933	0.939	0.927	0.966
	3.81x0.32x30.5 (centered)	0.987	0.989	0.942	0.952	0.981	0.844	0.934	0.868
	% Difference	-0.70%	1.21%	3.87%	3.98%	-5.08%	10.05%	-0.82%	10.06%
8-cm	3.81x0.64x30.5 (eccentric)	0.963	0.992	0.935	1.005	0.795	0.874	0.911	0.912
	3.81x0.32x30.5 (centered)	1.001	0.980	0.807	0.768	0.819	0.789	0.758	0.799
	% Difference	-4.03%	1.16%	13.66%	23.53%	-3.06%	9.81%	16.78%	12.35%
12-cm	3.81x0.64x30.5 (eccentric)	0.951	0.960	0.857	0.876	0.866	0.839	0.868	0.865
	3.81x0.32x30.5 (centered)	0.978	0.936	0.756	0.673	0.690	0.738	0.728	0.686
	% Difference	-2.87%	2.50%	11.72%	23.21%	20.29%	11.97%	16.16%	20.67%
16-cm	3.81x0.64x30.5 (eccentric)	0.945	0.888	0.762	0.485	0.318	0.396	0.454	0.446
	3.81x0.32x30.5 (centered)	0.955	0.884	0.671	0.611	0.654	0.599	0.607	0.647
	% Difference	-1.05%	0.45%	11.90%	-26.03%	-105.42%	-51.20%	-33.53%	-45.16%
Clamped End									
4-cm	3.81x0.64x30.5 (eccentric)	0.963	0.962	0.908	0.935	0.924	0.918	0.996	0.967
	3.81x0.32x30.5 (centered)	0.987	0.985	0.981	1.022	0.886	0.887	0.946	0.905
	% Difference	-2.56%	-2.46%	-8.08%	-9.35%	4.12%	3.34%	4.94%	6.36%
8-cm	3.81x0.64x30.5 (eccentric)	0.957	0.897	0.828	0.935	0.922	0.819	0.639	0.678
	3.81x0.32x30.5 (centered)	0.958	0.897	0.973	0.731	0.789	0.753	0.795	0.781
	% Difference	-0.09%	0.07%	-17.49%	21.82%	14.37%	8.10%	-24.45%	-15.24%
12-cm	3.81x0.64x30.5 (eccentric)	0.933	0.808	0.547	0.471	0.534	0.565	0.628	0.589
	3.81x0.32x30.5 (centered)	0.895	0.850	0.763	0.723	0.664	0.707	0.701	0.676
	% Difference	4.12%	-5.18%	-39.52%	-53.52%	-24.42%	-25.19%	-11.59%	-14.90%
16-cm	3.81x0.64x30.5 (eccentric)	0.992	0.733	0.335	0.459	0.480	0.523	0.445	0.442
	3.81x0.32x30.5 (centered)	0.862	0.795	0.620	0.597	0.655	0.619	0.605	0.632
	% Difference	13.09%	-8.48%	-85.31%	-30.07%	-36.48%	-18.33%	-36.02%	-42.90%

Table 4.5 Comparison of eccentrically and centrally notched beams normalized by the notchless cases.

The normalized frequencies deviate less than 10% for the beams containing notches of length 4 cm. An eccentrically located notch and a centrally located notch are comparable for a small crack. The normalized frequencies of beams containing 8-cm notches are also close. The highest deviations between the eccentrically and centrally notched beams are 12% for the 6th mode of the notch located at the free end and 24% for the 4th mode of the notch located in the middle.

The differences become significant for the beams containing longer notches. The 12-cm notch located in the middle produces frequencies that are still within 24%. For this case, the eccentric beam actually has a higher stiffness indicated by the larger normalized natural frequencies. The beams containing 12-cm notches at the free end and the clamped end display normalized natural frequencies that are

significantly lower in the eccentrically notched beam. This deviation indicates a lower stiffness, which is expected. The 16-cm notched beams display this behavior at all three notch locations. The largest deviations are 108% for the 3rd mode of the free end notched bar, 105% for the 5th mode of the mid-bar notch, and 85% for the 3rd mode of the clamped end notched bar. This suggest that for longer notches, the eccentrically placed notch has a greater influence on the natural frequency. However, the influence of the beam thickness differences may not be canceled by the simple normalization.

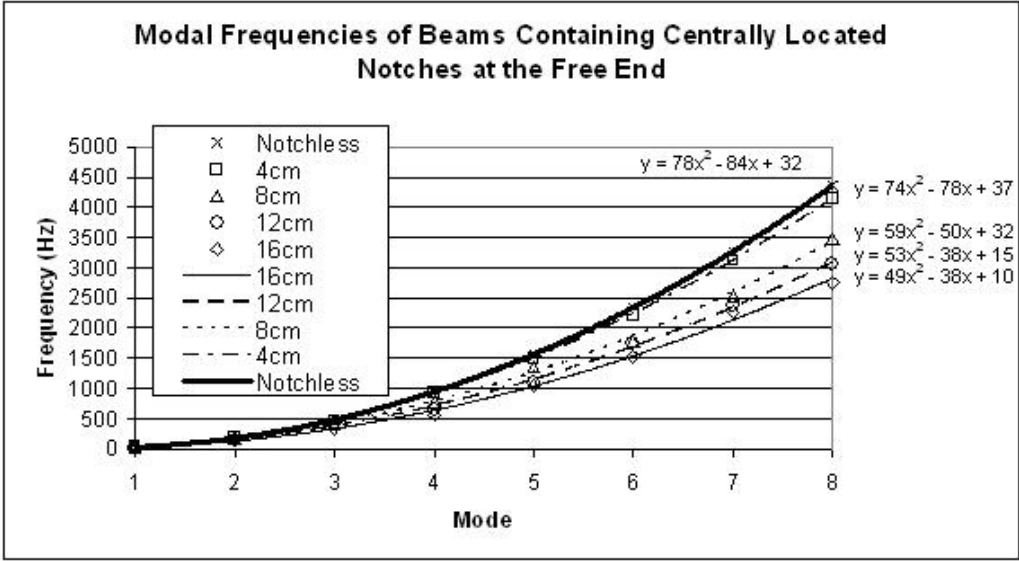


Figure 4.15 Frequency modes of beam containing centrally located notch at the free end.

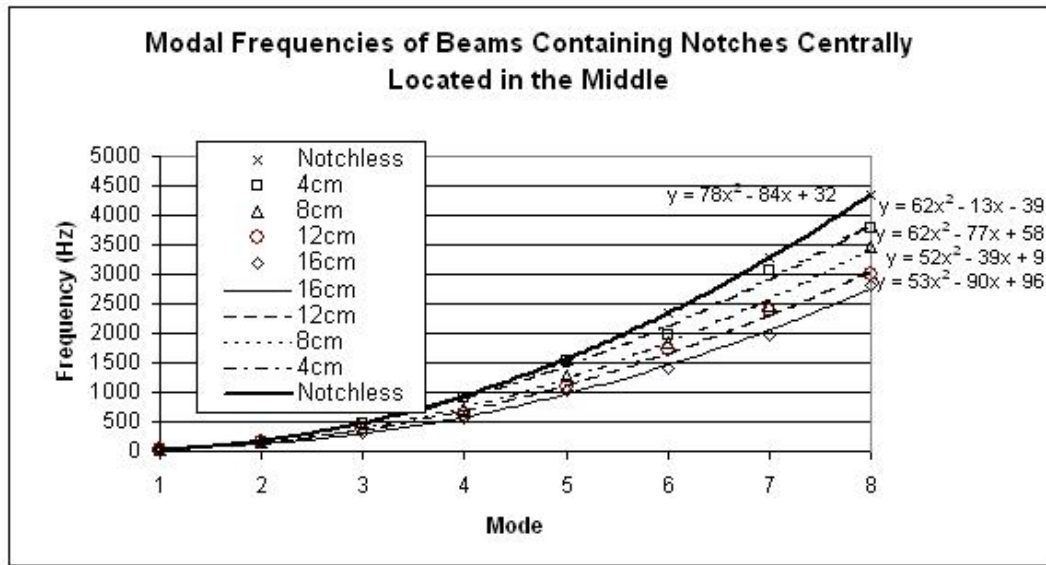


Figure 4.16 Frequency modes of beam containing centrally located notch in the middle.

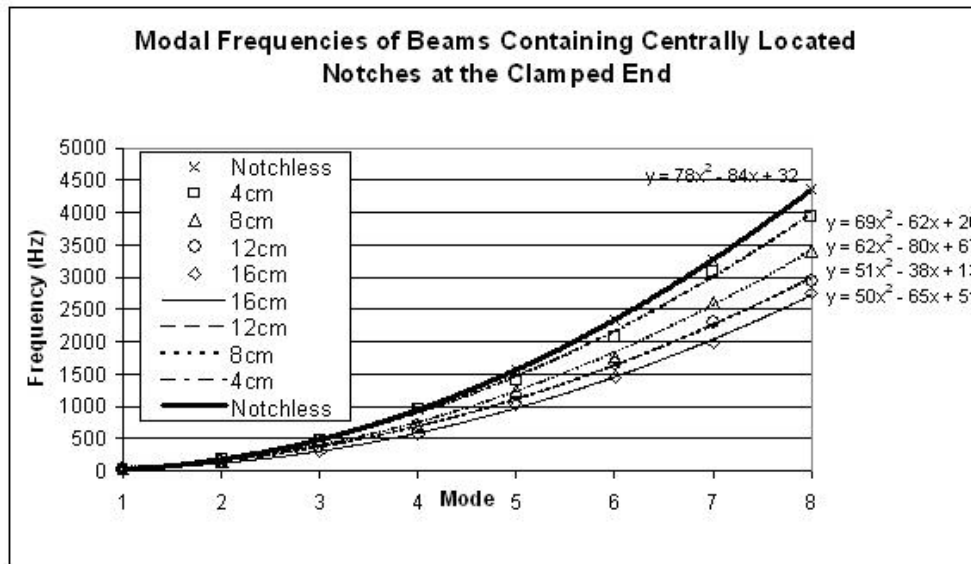


Figure 4.17 Frequency modes of beam containing centrally located notch at the clamped end.

Unlike the eccentrically notched beams, the beams containing centrally located notches display a linear proportionality between notch length and deviation from the reference case for all three notch locations. However, the notches become discernable at a higher mode than for the eccentrically notched beams.

In Table 4.6, the deviation from the notchless case of the modal frequencies calculated from the curve fits of the experimental data are displayed. Modes four and higher are shown, to compare with the eccentrically notched beam results.

Observation of the percent deviation from the notchless case yields the following comparison of the centered and eccentric notches. The centered notch has a larger deviation from the notchless beam than the eccentric notch for the 5th through 8th modal frequencies for the beams with 4-cm and 8-cm notches at each of the three locations. This observation also applies to the 12-cm middle notched beam. However, the beams containing the 12-cm notch at the free end and clamped end, and the 16-cm notches have larger deviations in frequency in the eccentrically placed notches rather than the centered notches. The difference in percent deviations is a result of the difference in notch location along the beam thickness, and the difference in thickness.

In the case of the centrally notched beam, the modal frequency percent deviations from the notchless case of notches with equal length at different locations differ less than 5% for the 8-cm, the 12-cm, and the 16-cm notched beams. The largest percent deviation occurs in the 4-cm notched beams between the middle and clamped-end notched beams, which differ in the eighth mode by 7%. Therefore, the location appears more difficult to diagnose in beams containing centered notches.

CURVE-FIT MODAL FREQUENCIES					
Centrally notched beams					
Deviation from notchless beam (%)					
Mode	4	5	6	7	8
Notchless	944	1562	2336	3266	4352
Free End					
4-cm	909 3.71%	1497 4.16%	2233 4.41%	3117 4.56%	4149 4.66%
8-cm	776 17.80%	1257 19.53%	1856 20.55%	2573 21.22%	3408 21.69%
12-cm	711 24.68%	1150 26.38%	1695 27.44%	2346 28.17%	3103 28.70%
16-cm	642.0 31.99%	1045 33.10%	1546 33.82%	2145 34.32%	2842 34.70%
Middle					
4-cm	901 4.56%	1446 7.43%	2115 9.46%	2908 10.96%	3825 12.11%
8-cm	742 21.40%	1223 21.70%	1828 21.75%	2557 21.71%	3410 21.65%
12-cm	685 27.44%	1114 28.68%	1647 29.49%	2284 30.07%	3025 30.49%
16-cm	584.0 38.14%	971 37.84%	1464 37.33%	2063 36.83%	2768 36.40%
Clamped End					
4-cm	882 6.57%	1441 7.75%	2138 8.48%	2973 8.97%	3946 9.33%
8-cm	739 21.72%	1217 22.09%	1819 22.13%	2545 22.08%	3395 21.99%
12-cm	677 28.28%	1098 29.71%	1621 30.61%	2246 31.23%	2973 31.69%
16-cm	591.0 37.39%	976 37.52%	1461 37.46%	2046 37.35%	2731 37.25%

Table 4.6 Modal frequencies obtained from the least-squares curve-fit of the experimental data of the centrally notched beams.

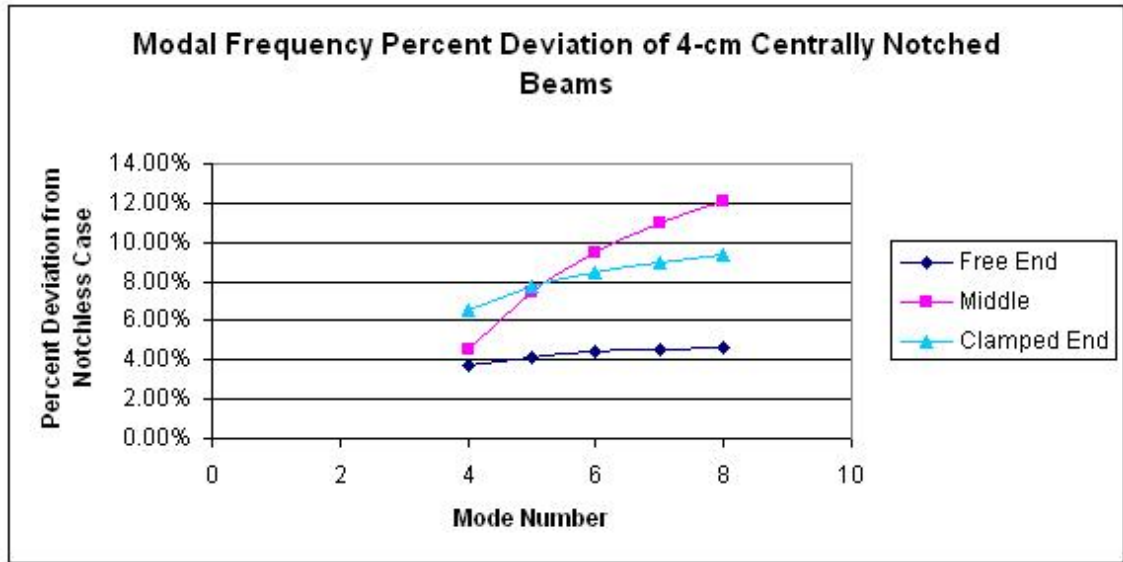


Figure 4.18 Modal frequency percent deviation of 4-cm centrally notched beams.

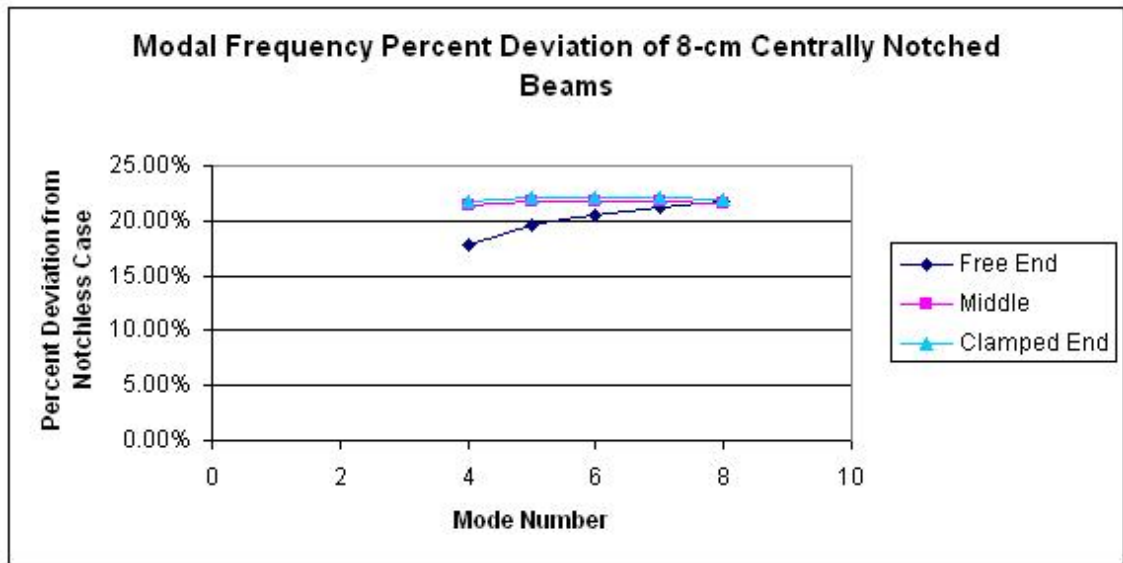


Figure 4.19 Modal frequency percent deviation of 8-cm centrally notched beams.

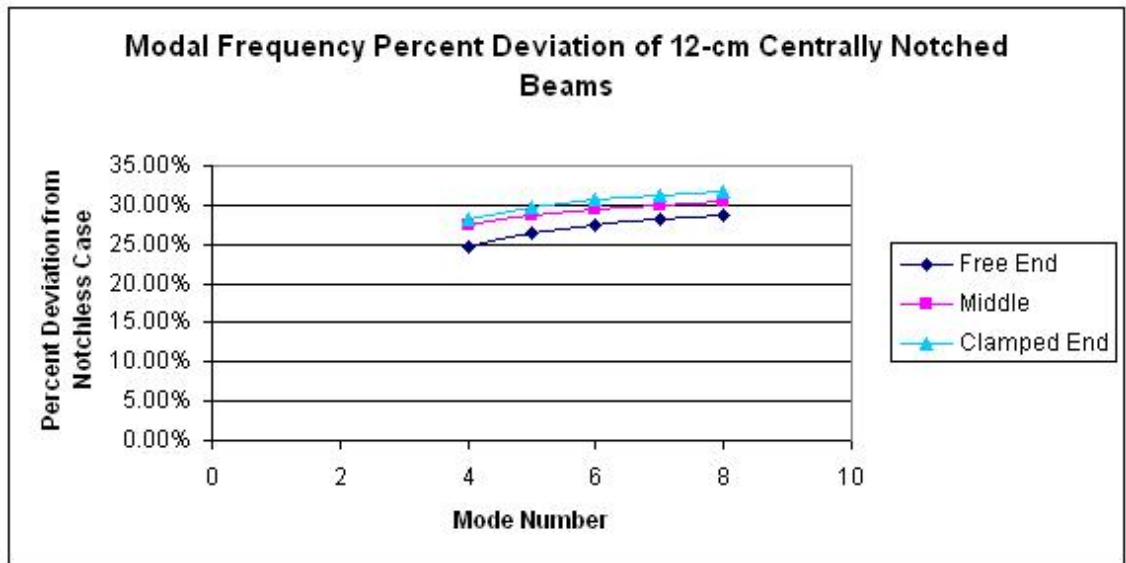


Figure 4.20 Modal frequency percent deviation of 12-cm centrally notched beams.

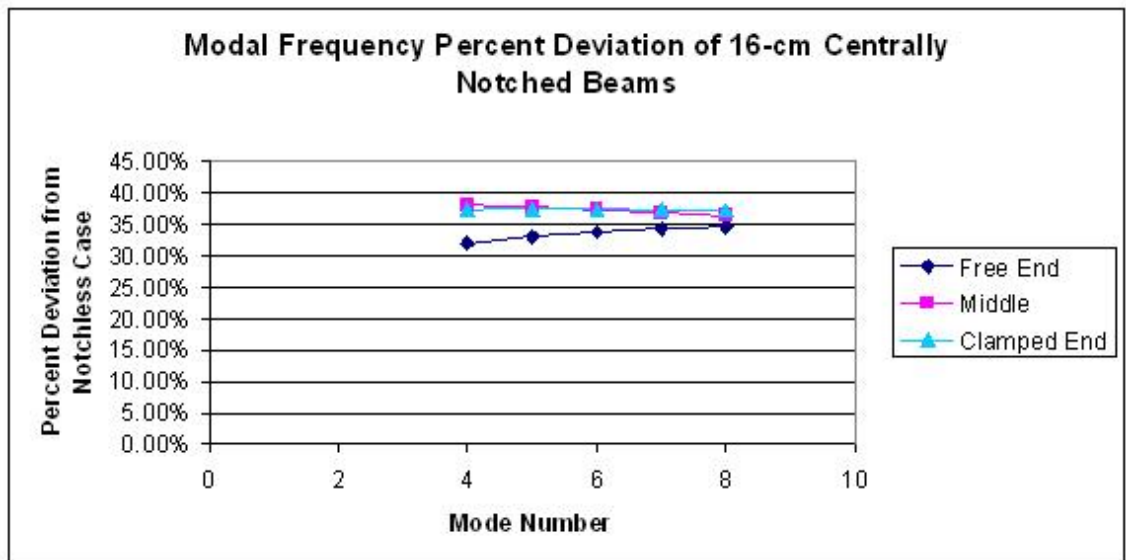


Figure 4.21 Modal frequency percent deviation of 16-cm centrally notched beams.

Mode	5	6	7
4-cm	3% to 8%	3% to 10%	3% to 10%
8-cm	9% to 23%	10% to 25%	10% to 22%

Table 4.7 Ranges of percent deviation from notchless case for 4-cm and 8-cm notched beams for mode 5, mode 6, and mode 7.

Again, observing the 6th mode, if the deviation is between 4% and 10%, then the notch is 13% of the beam. If the deviation is between 20% and 25%, then the notch is 26% of the beam. If the deviation is between 26% and 31% of the beam, then the notch is 39% of the beam length. If the deviation is between 34% and 38% then the notch length is over 50% of the beam.

If the above observation is considered in conjunction with the observations of the eccentric notches, a method for approximating notch size despite location can be determined. A frequency deviation of 3% to 10% indicates a notch, which is around 13% of the beam length. Likewise, a deviation of 10% to 25% indicates a notch length around 26% of the beam. Longer notches cannot be distinguished unless the notch location is known. However, the evaluating of small notches is more critical for practical purposes. The other modes are then evaluated and the results are displayed in table 4.7

4.4 *Perel-Palazotto Code*

The Perel-Palazotto code was first run for the notchless beam case. The results are shown compared with the theoretical natural frequencies shown in the following table.

The theory differs by less than 3%. The Perel-Palazotto code was run for three notched beam cases, the 4-cm and 8-cm free-end notched beams and the 4-cm middle notched beam. The deviation from the experimental case is displayed in the following table.

Mode	Theory	Perel-Palazotto	Error
1	56.31	57.44	-2.01%
2	352.9	359.1	-1.77%
3	988.2	1002	-1.41%
4	1937	1954	-0.91%
5	3201	3210	-0.29%
6	4782	4759	0.47%
7	6678	6578	1.34%
8	8892	8685	2.32%

Table 4.8 Comparison of theoretical and Perel-Palazotto natural frequencies of the notchless beam.

		Modal Frequencies							
		1	2	3	4	5	6	7	8
Notchless	Exp.	52.92	330.9	1053	1869	3093	4590	6306	8450
	MATLAB	57.44	359.1	1002	1954	3210	4759	6589	8685
	$\Delta\%$	7.87%	7.87%	-5.07%	4.34%	3.66%	3.56%	4.29%	2.71%
Free End 4-cm	Exp.	52.81	328.1	1009	1828	2972	4322	6178	8134
	MATLAB	57.44	359.1	1002	1954	3210	4758	6586	8678
	$\Delta\%$	8.06%	8.63%	-0.70%	6.45%	7.41%	9.16%	6.19%	6.27%
Free End 8-cm	Exp.	52.50	325.0	987.5	1731	2903	3966	5481	6881
	MATLAB	57.44	359.1	1002	1953	3196	4684	5857	6717
	$\Delta\%$	8.60%	9.50%	1.45%	11.37%	9.18%	15.33%	6.41%	-2.44%
Middle 4-cm	Exp.	51.88	331.3	812.5	1853	2887	4309	5844	8159
	MATLAB	57.44	359.1	1002	1954	3209	4757	6585	8671
	$\Delta\%$	9.68%	7.74%	18.91%	5.17%	10.04%	9.42%	11.25%	5.90%

Table 4.9 Comparison of the experimental results and the Perel-Palazotto code results for selected cases.

The results of the Perel-Palazotto code agree within 20% of the experimental values. In general the experimental natural frequencies suggest a lower stiffness than the code suggests. This difference may in part be due to a small difference in the material properties entered in the code, and the actual material properties.

4.5 Cobb-Durham Code

The Cobb-Durham code was first run for the notchless case and compared with the theoretical modal frequencies, which can be seen in Table 4.10. The Cobb-Durham code differs less than 1% from the theoretical values.

Mode	Theory	Cobb-Durham	Error
1	56.31	55.81	0.88%
2	352.9	349.7	0.91%
3	988.2	979.9	0.90%
4	1937	1919	0.91%
5	3201	3172	0.90%
6	4782	4739	0.90%
7	6678	6619	0.89%
8	8892	8813	0.89%

Table 4.10 Comparison of theoretical and Cobb-Durham natural frequencies of the notchless beam.

The code was then run for all the eccentric notch cases. The code models the section containing the notch as a beam with a smaller moment of inertia. The computer results are compared with the experimental results in Table 4.11. The percent difference is calculated by

$$\%change = \frac{(\text{Experimental modal frequency}) - (\text{Computed modal frequency})}{(\text{Experimental modal frequency})} \times 100\% \quad (4.4)$$

The Cobb-Durham code produces close results for the 4-cm and 8-cm notched beams. The 4-cm notched beam frequencies are predicted within 5% for modes higher than mode 3. The modal frequencies of the 8-cm notched beams are predicted within 10% for the modes higher than mode 3. The 12-cm notched beam frequencies are also within 10% for the notch located in the middle. The clamped end and free end experimental frequencies are much lower than the computed frequencies, as well as the 16-cm notch cases. This deviation is expected since the code does not account for contact between crack surfaces and allows them to overlap during vibration.

		EXPERIMENTAL MODAL FREQUENCIES							
		Centrally Located Notch							
Mode		1	2	3	4	5	6	7	8
Notchless	Exp.	52.92	330.9	1053	1869	3093	4590	6306	8450
	MATLAB	55.81	349.7	979.3	1919	3172	4739	6619	8813
	$\Delta\%$	-5.46%	-5.69%	7.00%	-2.66%	-2.57%	-3.25%	-4.96%	-4.30%
Free End									
4-cm	Exp.	52.81	328.1	1009	1828	2972	4322	6178	8134
	MATLAB	56.40	351.1	967.0	1840	2953	4367	6140	8256
	$\Delta\%$	-6.80%	-7.01%	4.16%	-0.66%	0.64%	-1.04%	0.62%	-1.50%
8-cm	Exp.	52.50	325.0	987.5	1731	2903	3966	5481	6881
	MATLAB	56.69	333.4	840.7	1664	2809	4098	5760	7762
	$\Delta\%$	-7.98%	-2.58%	14.87%	3.87%	3.23%	-3.33%	-5.08%	-12.80%
12-cm	Exp.	52.50	306.3	942.5	1666	2291	2550	3700	5023
	MATLAB	56.25	300.8	798.9	1611	2593	3975	5425	7367
	$\Delta\%$	-7.14%	1.80%	15.24%	3.30%	-13.18%	-55.88%	-46.62%	-46.67%
16-cm	Exp.	47.50	295.0	352.5	857.5	1485	2400	2805	3738
	MATLAB	54.13	269.0	782.0	1471	2472	3708	5100	6919
	$\Delta\%$	-13.96%	8.81%	-121.84%	-71.55%	-66.46%	-54.50%	-81.82%	-85.10%
Middle									
4-cm	Exp.	51.88	331.3	812.5	1853	2887	4309	5844	8159
	MATLAB	53.48	306.9	968.2	1749	3067	4441	6264	8381
	$\Delta\%$	-3.08%	7.36%	-19.16%	5.61%	-6.25%	-3.06%	-7.19%	-2.72%
8-cm	Exp.	50.94	328.1	775.0	1878	2459	4013	5744	7703
	MATLAB	50.09	278.0	868.0	1720	2691	4162	5848	7581
	$\Delta\%$	1.67%	15.27%	-12.00%	8.41%	-9.43%	-3.71%	-1.81%	1.58%
12-cm	Exp.	50.31	317.5	710.0	1638	2678	3850	5473	7308
	MATLAB	47.78	269.6	786.0	1645	2658	3839	5471	7413
	$\Delta\%$	5.03%	15.09%	-10.70%	-0.43%	0.75%	0.29%	0.04%	-1.44%
16-cm	Exp.	50.00	293.8	631.3	906.3	985.0	1819	2865	3766
	MATLAB	45.40	264.1	733.1	1502	2567	3787	5151	6842
	$\Delta\%$	9.20%	10.11%	-16.13%	-65.73%	-160.61%	-108.19%	-79.79%	-81.68%
Clamped End									
4-cm	Exp.	50.94	318.2	955.7	1747	2858	4212	6279	8169
	MATLAB	44.10	312.8	914.9	1818	2998	4446	6193	8274
	$\Delta\%$	13.43%	1.70%	4.27%	-4.06%	-4.90%	-5.56%	1.37%	-1.29%
8-cm	Exp.	50.63	296.9	871.9	1747	2850	3760	4031	5725
	MATLAB	38.59	309.4	852.1	1671	2842	4209	5790	7817
	$\Delta\%$	23.78%	-4.21%	2.27%	4.35%	0.28%	-11.94%	-43.64%	-36.54%
12-cm	Exp.	49.38	267.5	575.5	880	1650	2593	3960	4975
	MATLAB	36.64	290.0	805.7	1644	2623	4013	5536	7385
	$\Delta\%$	25.80%	-8.41%	-40.00%	-86.82%	-58.97%	-54.76%	-39.80%	-48.44%
16-cm	Exp.	52.50	242.5	352.5	857.5	1485	2400	2805	3738
	MATLAB	35.57	256.2	794.3	1483	2530	3710	5216	6965
	$\Delta\%$	32.25%	-5.65%	-125.33%	-72.94%	-70.37%	-54.58%	-85.95%	-86.33%

Table 4.11 Comparison of experimental and Cobb-Durham results for the eccentrically notched beams.

The results produced for the centrally notched beams are displayed in Table 4.12.

The natural frequencies of the centrally notched beams show even better agreement between the code and the experimental results. The first and second mode appear to show some large deviation. However, the code modal frequencies of mode 4 and higher modes are within 10% of the experimental frequencies for most cases.

The Cobb-Durham code does not account for the nonlinearities of the response, which result from the crack surfaces touching when the sublaminates are vibrating at different frequencies. The nonlinear nature is augmented in the eccentrically located notch, which is the reason the code agreement with experimental results differs by a greater amount for the eccentrically notched beams than for the centrally notched

beams. However, the Cobb-Durham code provides good estimates of the modal frequencies.

4.6 Notch Depth

The comparison of the centered and eccentric notches with beams of the same thickness may provide more information. Using the Cobb-Durham code, modal frequencies were computed for beams with centered notches and a beam thickness of 1/4-in. These frequencies are compared with the eccentrically notched beams computed frequencies in Figures 4.22 through 4.25.

For each notch length, the centrally notched beams at all locations have higher modal frequencies than all three of the eccentrically notched beams. In the 4-cm

		MODAL FREQUENCIES Centrally Located Notch							
Mode		1	2	3	4	5	6	7	8
Notchless	Exp.	28.09	172.4	484.1	944.8	1566	2342	3268	4359
	MATLAB	27.90	174.9	489.7	959.5	1586	2370	3310	4407
	Δ%	0.68%	-1.43%	-1.16%	-1.56%	-1.30%	-1.20%	-1.30%	-1.09%
Free End									
4-cm	Exp.	28.91	175.3	471.7	931.8	1485	2213	3116	4151
	MATLAB	28.54	175.9	469.7	849.0	1349	2048	2925	3912
	Δ%	1.28%	-0.36%	0.43%	8.93%	9.16%	7.47%	6.13%	5.76%
8-cm	Exp.	29.30	166.9	421.6	774.3	1360	1779	2533	3477
	MATLAB	28.74	152.5	358.1	757.0	1220	1798	2601	3353
	Δ%	1.91%	8.64%	15.07%	2.19%	10.27%	-1.05%	-2.67%	3.56%
12-cm	Exp.	29.04	154.3	406.3	658.2	1090	1748	2369	3048
	MATLAB	28.06	123.8	348.6	661.0	1124	1644	2336	3067
	Δ%	3.37%	19.77%	14.19%	-0.43%	-3.09%	5.97%	1.39%	-0.61%
16-cm	Exp.	28.26	146.8	336.6	561.5	1046	1535	2264	2750
	MATLAB	25.33	107.5	314.1	608.0	965	1510	2064	2726
	Δ%	10.37%	26.76%	6.68%	-8.20%	7.78%	1.63%	8.82%	0.87%
Middle									
4-cm	Exp.	27.73	170.6	456.2	899.2	1536	1978	3053	3786
	MATLAB	24.84	132.7	474.3	819	1449	2137	2901	4045
	Δ%	10.42%	22.20%	-3.96%	8.94%	5.64%	-8.06%	4.98%	-6.85%
8-cm	Exp.	28.13	169.0	390.9	725.8	1283	1847	2477	3483
	MATLAB	21.34	116.9	367.7	793	1191	1776	2637	3383
	Δ%	24.14%	30.83%	5.93%	-9.23%	7.17%	3.83%	-6.46%	2.88%
12-cm	Exp.	27.47	161.3	366.1	635.7	1081	1729	2378	2991
	MATLAB	19.42	111.9	314.5	689	1169	1636	2240	3118
	Δ%	29.30%	30.64%	14.10%	-8.43%	-8.17%	5.40%	5.79%	-4.25%
16-cm	Exp.	26.82	152.4	324.9	577.3	1024	1403	1982	2820
	MATLAB	17.72	106.3	289.5	584	1032	1582	2146	2757
	Δ%	33.93%	30.26%	10.89%	-1.23%	-0.75%	-12.73%	-8.26%	2.25%
Clamped End									
4-cm	Exp.	27.73	169.9	474.9	965.5	1387	2077	3093	3946
	MATLAB	16.87	145.9	436.5	858	1394	2075	2934	3970
	Δ%	39.17%	14.13%	8.08%	11.12%	-0.48%	0.11%	5.13%	-0.60%
8-cm	Exp.	26.90	154.6	471.0	690.3	1235	1763	2599	3404
	MATLAB	13.71	137.6	367.0	762	1283	1830	2624	3524
	Δ%	49.02%	11.01%	22.07%	-10.35%	-3.85%	-3.76%	-0.95%	-3.53%
12-cm	Exp.	25.13	146.6	369.1	682.8	1039	1656	2290	2949
	MATLAB	12.75	116.4	352.7	694	1124	1722	2339	3206
	Δ%	49.26%	20.62%	4.45%	-1.68%	-8.15%	-3.96%	-2.15%	-8.71%
16-cm	Exp.	24.22	137.1	300.3	563.7	1026	1449	1977	2756
	MATLAB	12.25	94.30	325.4	610.0	1001	1549	2076	2841
	Δ%	49.42%	31.22%	-8.36%	-8.21%	2.44%	-6.90%	-5.01%	-3.10%

Table 4.12 Comparison of experimental and Cobb-Durham results for the centrally notched beams.

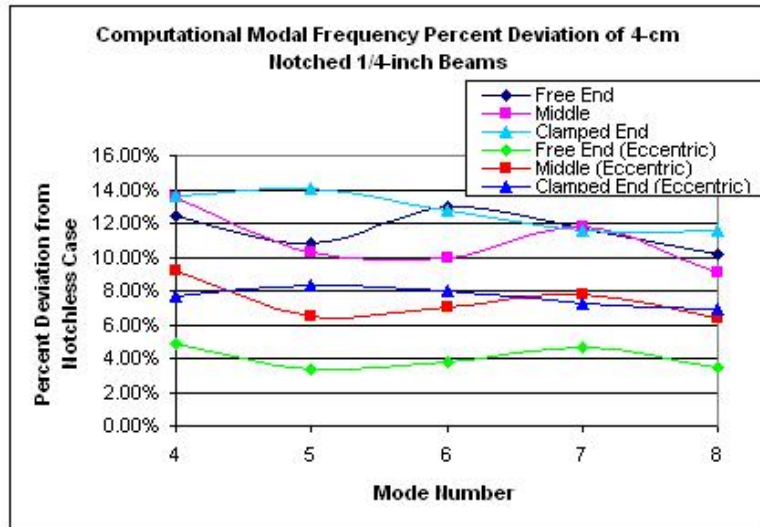


Figure 4.22 Computational modal frequency percent deviation of 4-cm notched beams.

case, the centrally notched beam frequencies are at least 2% larger than eccentrically notched beam frequencies, and are 4% larger in the seventh mode. In the 8-cm case, the centrally notched beam frequencies are 5% to 7% larger. These trends indicate

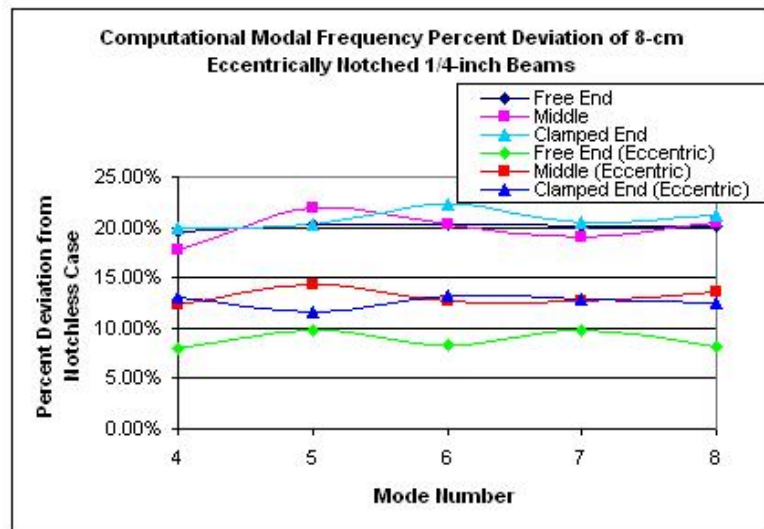


Figure 4.23 Computational modal frequency percent deviation of 8-cm notched beams.

the possibility of estimating the notch depth with experimentally obtained ranges of the percent deviation from the notchless case.

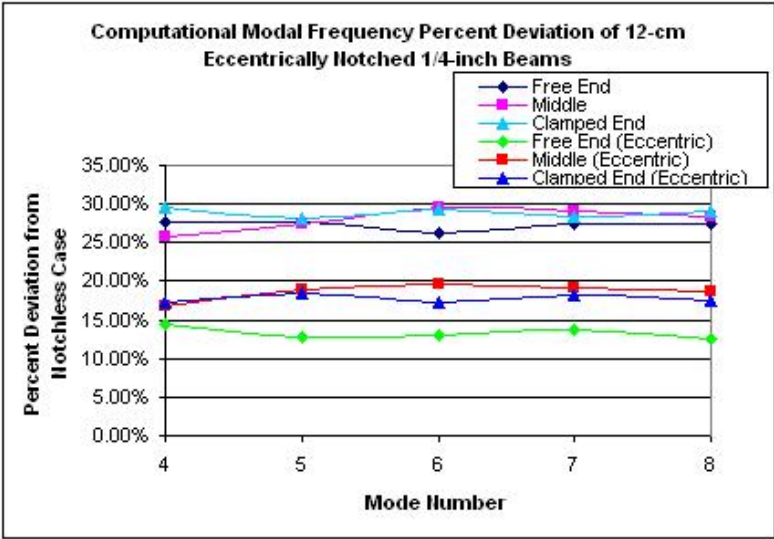


Figure 4.24 Computational modal frequency percent deviation of 12-cm notched beams.

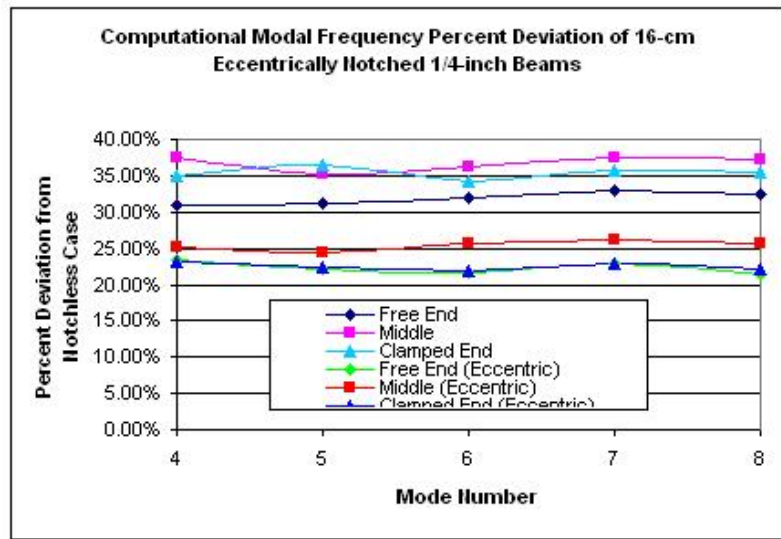


Figure 4.25 Computational modal frequency percent deviation of 16-cm notched beams.

4.7 Locations of maximum shear

The notch should have greater impact on points where the beam is subjected to greater shear. The locations of maximum shear occur at nodes of modal curvature inflection, where the mode shape changes from concave up to concave down, or vice versa. A notch that intersects one of these locations of maximum shear may have an amplified effect on the modal frequencies.

In Table 4.14, the change in frequency as the notch length increases in length by 4 cm, and the number of points of maximum shear crossed by the notch are presented. The large percent changes should correspond to a difference in the number of points crossed.

$$\% \text{ Change} = \frac{(\text{Frequency of longer notched beam}) - (\text{Frequency of shorter notched beam})}{(\text{Frequency of shorter notched beam})} \times 100\% \quad (4.5)$$

Several modes exhibit the expected behavior. In the beams containing notches at the clamped end, the 8-cm notch crosses two additional nodes in the seventh mode and one additional node in the eighth mode, which result in large frequency changes of 36% and 30% respectively. The 12-cm notch crosses an additional node in mode three and mode 5, which result in frequency changes of 34% and 42%. The 16-cm notch crosses an additional node in the eighth mode and two additional nodes in the seventh mode, which result in 25% and 29% changes. However, the theory does not hold up for some instances. The 8-cm notch crosses additional nodes in the fourth and fifth modes, but the modal frequency does not change. The 8-cm notch crosses two additional modes in the sixth mode, and the frequency change is only 11%. In the case of the 12-cm notch, a large percentage change in frequency is seen where an additional node is not crossed, in the fourth and sixth modes. As for the 16-cm notch, little frequency change is seen where additional nodes are crossed in the fourth and sixth modes.

	EXPERIMENTAL MODAL FREQUENCIES							
	Deviation from notchless beam (%)							
	Number of nodes crossed							
Mode	1	2	3	4	5	6	7	8
Notchless	52.92	330.9	1053	1869	3093	4590	6306	8450
Free End								
4-cm	52.81 0.21% 0	328.1 0.84% 0	1009 4.18% 0	1828 2.21% 0	2972 3.90% 0	4322 5.84% 0	6178 2.03% 0	8134 3.74% 0
8-cm	52.50 0.79% 0	325.0 1.77% 0	987.5 6.22% 0	1731 7.40% 0	2903 6.14% 1	3966 13.59% 1	5481 13.08% 1	6881 18.57% 2
12-cm	52.50 0.79% 0	306.3 7.42% 0	942.5 10.49% 0	1666 10.88% 1	2291 25.92% 1	2550 44.44% 2	3700 41.33% 3	5023 40.56% 3
16-cm	47.50 10.24% 0	295.0 10.84% 0	352.5 66.52% 0	857.5 54.13% 1	1485 51.98% 1	2400 47.71% 1	2805 55.52% 2	3738 55.76% 2
Middle								
4-cm	51.88 1.97% 0	331.3 -0.13% 0	812.5 1.96% 0	1853 0.87% 0	2887 6.66% 1	4309 6.12% 1	5844 7.33% 1	8159 3.44% 2
8-cm	50.94 3.74% 0	328.1 0.84% 0	775.0 6.48% 1	1878 -0.46% 0	2459 20.49% 1	4013 12.57% 2	5744 8.92% 2	7703 8.84% 4
12-cm	50.31 4.93% 0	317.5 4.04% 0	710.0 14.33% 1	1638 12.38% 1	2678 13.41% 2	3850 16.12% 2	5473 13.21% 3	7308 13.51% 4
16-cm	50.00 5.52% 0	293.8 11.20% 2	631.3 23.82% 2	906.3 51.52% 3	985 68.15% 4	1819 60.37% 5	2865 54.57% 6	3766 55.43% 6
Clamped End								
4-cm	50.94 3.74% 0	318.2 3.83% 1	955.7 9.24% 1	1747 6.60% 1	2858 7.59% 1	4212 8.24% 1	6279 0.43% 2	8169 3.33% 2
8-cm	50.63 4.33% 0	296.9 10.27% 1	871.9 17.20% 1	1747 6.54% 2	2850 7.85% 2	3760 18.08% 3	4031 36.08% 3	5725 32.25% 3
12-cm	49.38 6.69% 0	267.5 19.15% 1	575.5 45.35% 2	880 52.92% 2	1650 46.65% 3	2593 43.51% 3	3960 37.21% 3	4975 41.12% 4
16-cm	52.50 0.79% 0	242.5 26.71% 1	352.5 66.52% 4	857.5 54.13% 3	1485 51.98% 3	2400 47.71% 4	2805 55.52% 5	3738 55.76% 5

Table 4.13 Modal frequency and nodes crossed of the eccentrically notched beams.

	NODES CROSSED (Eccentric Notch)							
	(%) Change							
Mode	1	2	3	4	5	6	7	8
Free End								
4cm	0	0	0	0	0	0	0	0
	0.59%	0.94%	2.13%	5.31%	2.33%	8.24%	11.28%	15.40%
8cm	0	0	0	0	1	1	1	2
	0.00%	5.75%	4.56%	3.76%	21.07%	35.70%	32.50%	27.00%
12cm	0	0	0	1	1	2	3	3
	9.52%	3.69%	62.60%	48.53%	35.18%	5.88%	24.19%	25.58%
16cm	0	0	0	1	1	1	2	2
Middle								
4cm	0	0	0	0	1	1	1	2
	1.81%	0.97%	4.62%	-1.35%	14.82%	6.87%	1.71%	5.59%
8cm	0	0	1	0	1	2	2	4
	1.24%	3.23%	8.39%	12.78%	-8.91%	4.06%	4.72%	5.13%
12cm	0	0	1	1	2	2	3	4
	0.62%	7.46%	11.08%	44.67%	63.22%	52.75%	47.65%	48.47%
16cm	0	1	2	2	3	4	5	6
Clamped End								
4cm	0	0	1	1	1	1	1	2
	0.61%	6.69%	8.77%	0.00%	0.28%	10.73%	35.80%	29.92%
8cm	0	1	1	2	2	3	3	3
	2.47%	9.90%	33.99%	49.63%	42.11%	31.04%	1.76%	13.10%
12cm	0	1	2	2	3	3	3	4
	-6.32%	9.35%	38.75%	2.56%	10.00%	7.44%	29.17%	24.86%
16cm	0	1	2	3	3	4	5	5

Table 4.14 Percent change between notch size and number points of maximum shear crossed in the eccentrically notched beam.

In the case of the mid-bar notches, similar variation is found. The 8-cm notch crosses additional nodes in the third, sixth, seventh, and eighth modes, where the frequency change is less than 6%. Furthermore, the largest frequency change between the 4-cm and 8-cm notched bar is seen in the fifth mode where no additional node is crossed. The largest frequency change from the 8-cm notch to the 12-cm notch is in the fourth mode where an additional node is crossed. An additional node is also crossed in the seventh mode, but the frequency change is less than 5%. The 16-cm notch crosses one or two additional notches in modes four through eight where

a large frequency change is seen. The second and third modes only show a small change, even though an additional notch is crossed.

The beams containing notches at the free end also produce similar results. In the case of the 8-cm notched beam, the largest changes occur when additional nodes are crossed. The 12-cm notch crosses additional nodes in the sixth, seventh, and eighth modes where a large change is evident. However, a large change occurs in the fifth mode where no additional node is crossed, and a small change occurs in the fourth mode where an additional node is crossed.

Table 4.15 displays the number of nodes crossed by the centered notch and the changes in modal frequency as crack size increases for the centrally notched beams.

The results for the centrally notched beams yield the same ambiguous correlation and are described in detail by Reifsnyder.¹⁸

When the centrally and eccentrically notched beams are compared, the eccentrically notched beams are found to cross either as many or more nodes than the centrally notched beams do for the experimental mode shapes for the 4cm, 8cm, and 12cm notched beams. The eccentrically notched beams cross more nodes in the fourth and eighth modes for the middle 4cm notch and in the third, seventh, and eighth modes for the clamped end 4cm notch. The free end 4cm notch crosses the same number of nodes in both cases. The eccentrically notched beams cross more nodes in the fifth, sixth, and eighth modes for the free end 8cm notch, in the fourth, sixth, and eighth modes for the middle 8cm notch, and in the fourth through eighth modes for the clamped end 8cm notch. Finally, the eccentrically notched beams cross more nodes in the fourth, sixth, seventh, and eighth modes for the free end 12cm notch, in the eighth mode for the middle 12cm notch, and in the third, fourth, fifth, seventh, and eighth modes for the clamped end 12cm notch.

Thus the eighth mode appears to lend some indication of notch depth through the modal shape. If the size and location is known, then the depth (if limited to two

	NODES CROSSED (Centered Notch)							
	(%) Change							
Mode	1	2	3	4	5	6	7	8
Free End								
4cm	0	0	0	0	0	0	0	0
	-1.35%	4.76%	10.62%	16.90%	8.44%	19.61%	18.70%	16.25%
8cm	0	0	0	0	0	0	1	1
	0.89%	7.57%	3.64%	15.00%	19.81%	1.74%	6.49%	12.32%
12cm	0	0	0	0	1	1	2	2
	2.69%	4.88%	17.15%	14.70%	4.04%	12.20%	4.45%	9.79%
16cm	0	0	0	1	1	2	2	3
Middle								
4cm	0	0	0	1	1	1	1	1
	-1.44%	0.92%	14.33%	19.29%	16.45%	6.62%	18.87%	7.99%
8cm	0	0	1	1	1	1	2	2
	2.35%	4.54%	6.33%	12.41%	15.77%	6.35%	4.01%	14.13%
12cm	0	0	1	1	2	2	3	3
	2.37%	5.52%	11.27%	9.19%	5.21%	18.85%	16.63%	5.71%
16cm	0	0	1	2	2	3	3	4
Clamped End								
4cm	0	0	0	1	1	1	0	1
	3.00%	8.99%	0.82%	28.50%	10.95%	15.12%	15.95%	13.75%
8cm	0	1	1	1	1	2	1	2
	6.57%	5.17%	21.62%	1.09%	15.88%	6.06%	11.91%	13.36%
12cm	0	1	1	1	2	3	2	3
	3.62%	6.50%	18.65%	17.44%	1.28%	12.52%	13.66%	6.56%
16cm	0	1	1	2	3	3	3	4

Table 4.15 Percent change between notch size and number points of maximum shear crossed in the centrally notched beam.

possibilities) can be determined by the following. Considering the free end, if an 8 cm notch crosses 1 node, it is centrally located, and if it crosses 2 nodes, the notch is eccentrically located. Two nodes crossed by a 12cm notch indicates a centered notch, and three nodes crossed indicate an eccentric notch. Considering the middle and clamped end notches, if a 4 cm notch crosses 1 node, it is centrally located, whereas if it crosses 2 nodes it is eccentrically located. Two nodes crossed by an 8 cm notch indicate a centered notch, whereas three nodes crossed indicate an eccentric

notch. Likewise, if a 12-cm notch crosses three nodes it is centered, and if a 12-cm notch crosses four nodes it is eccentric.

4.8 Locations of Maximum Curvature

Regions of maximum curvature, or anti-nodes, are also analyzed. Curvature at a point is

$$\nu'' = \frac{M}{EI} \quad (4.6)$$

where M is the bending moment, E is the modulus of elasticity, and I is the second moment of inertia of the cross-sectional area. Damage results in a decrease in the second moment of inertia, which should then result in an increase in curvature. The table below shows the number of anti-nodes crossed by the notch at each mode for each case.

The clamped-end notched beams demonstrate the following behavior. The greatest changes in frequency from the 4-cm notched beam to the 8-cm notched beam correspond to the modes where additional anti-nodes are crossed, namely the third, sixth, seventh, and eighth modes. The 12-cm notch crosses additional anti-nodes in the third, fifth, and sixth modes, where large changes in frequency are demonstrated. However, the frequency change is large in the fourth mode where no additional anti-node is crossed, and is less than 15% for the eighth and second modes where an additional anti-node is crossed. The 16-cm notch crosses one additional anti-node in the eighth mode and two additional anti-nodes in the seventh mode where the frequency changes are 25% and 30%. Nonetheless, a large frequency change is observed where no additional anti-node is crossed in the third mode, and the frequency change is insignificant where an additional anti-node is crossed in the fifth mode.

In the mid-located notched beam, the largest frequency changes from the 4-cm notched beam to the 8-cm notched beam occur when the notch crosses an additional

	ANTI-NODES CROSSED (Eccentric Notch)							
	(%) Change							
Mode	1	2	3	4	5	6	7	8
Free End								
4cm	0	0	0	0	0	1	0	1
	0.59%	0.94%	2.13%	5.31%	2.33%	8.24%	11.28%	15.40%
8cm	0	0	0	1	1	2	2	2
	0.00%	5.75%	4.56%	3.76%	21.07%	35.70%	32.50%	27.00%
12cm	0	0	1	2	2	3	3	4
	9.52%	3.69%	62.60%	48.53%	35.18%	5.88%	24.19%	25.58%
16cm	0	1	1	1	1	2	2	3
Middle								
4cm	0	1	0	1	1	1	1	1
	1.81%	0.97%	4.62%	-1.35%	14.82%	6.87%	1.71%	5.59%
8cm	0	1	1	1	2	2	3	2
	1.24%	3.23%	8.39%	12.78%	-8.91%	4.06%	4.72%	5.13%
12cm	0	1	2	1	2	3	2	3
	0.62%	7.46%	11.08%	44.67%	63.22%	52.75%	47.65%	48.47%
16cm	0	1	2	2	3	3	4	3
Clamped End								
4cm	0	0	0	0	1	1	2	1
	0.61%	6.69%	8.77%	0.00%	0.28%	10.73%	35.80%	29.92%
8cm	0	0	1	2	1	2	3	3
	2.47%	9.90%	33.99%	49.63%	42.11%	31.04%	1.76%	13.10%
12cm	0	1	2	2	2	3	2	4
	-6.32%	9.35%	38.75%	2.56%	10.00%	7.44%	29.17%	24.86%
16cm	0	1	2	2	3	3	4	5

Table 4.16 Percent change between notch size and number anti-nodes crossed in the eccentrically notched beam.

anti-node, although another anti-node is crossed in the seventh mode where negligible frequency change is seen. The 12-cm notch crosses additional anti-nodes in modes five through eight, and the corresponding frequency changes are large. The behavior of the third and fourth modes do not follow this trend.

The following table displays the number of nodes crossed by the centered notch and the changes in modal frequency as crack size increases for the centrally notched beams¹⁸

	ANTI-NODES CROSSED (Centered Notch)							
	(% Change)							
Mode	1	2	3	4	5	6	7	8
Free End								
4cm	0	0	0	0	0	0	0	0
	-1.35%	4.76%	10.62%	16.90%	8.44%	19.61%	18.70%	16.25%
8cm	0	0	0	0	1	1	1	1
	0.89%	7.57%	3.64%	15.00%	19.81%	1.74%	6.49%	12.32%
12cm	0	0	0	1	1	2	2	2
	2.69%	4.88%	17.15%	14.70%	4.04%	12.20%	4.45%	9.79%
16cm	0	0	1	1	2	2	3	3
Middle								
4cm	0	0	0	1	1	1	1	1
	-1.44%	0.92%	14.33%	19.29%	16.45%	6.62%	18.87%	7.99%
8cm	0	0	1	1	1	2	2	2
	2.35%	4.54%	6.33%	12.41%	15.77%	6.35%	4.01%	14.13%
12cm	0	1	0	1	2	2	3	3
	2.37%	5.52%	11.27%	9.19%	5.21%	18.85%	16.63%	5.71%
16cm	0	1	1	2	2	3	3	4
Clamped End								
4cm	0	0	1	0	0	1	1	2
	3.00%	8.99%	0.82%	28.50%	10.95%	15.12%	15.95%	13.75%
8cm	0	1	1	1	1	2	2	3
	6.57%	5.17%	21.62%	1.09%	15.88%	6.06%	11.91%	13.36%
12cm	0	1	1	1	2	2	3	3
	3.62%	6.50%	18.65%	17.44%	1.28%	12.52%	13.66%	6.56%
16cm	0	1	2	1	2	3	4	4

Table 4.17 Percent change between notch size and number anti-nodes crossed in the centrally notched beam.

The location of maximum curvature in the eighth mode reveals information about the depth of a notch located at the free end. If a 4 cm notch crosses 1 anti-node, it is eccentric, and if it crosses no anti-nodes, it is centered. Two anti-nodes crossed by an 8 cm notch indicate an eccentric notch, whereas one anti-node indicates a centered notch. Likewise, if a 12 cm notch crosses four anti-nodes, the notch is eccentric, whereas if it crosses two, it is centered.

4.9 ABAQUS Model

Two centrally notched beam specimens were modeled using the ABAQUS CAE package, the beams containing a 4 cm notch and an 8 cm notch at the clamped end. The ABAQUS approach requires that each case be individually modeled and meshed, in contrast to the MATLAB programs. The 4 cm notch was modeled by Capt Aaron Reifsnnyder. The 8 cm notch was modeled by Mr Vikram Dhruva. Approximately 14,000 8-noded linear hexahedral brick elements were used to model the 4 cm notched beam. Approximately 60% of the total elements were concentrated in the notched region. A mesh of 66,600 elements was constructed for the 8 cm notched beam, also concentrating elements in the notched region. The beam characteristics required for ABAQUS were a modulus of elasticity of 10×10^6 psi, a density of 2.666×10^{-4} slugs per cubic feet, and a poisson's ratio of 0.3. The piezoelectric patch was ignored for both cases. ABAQUS computes bending, torsional, and mixed modes, so the mode shapes were once again used to distinguish the pure bending modes. The bending modes are displayed in the table below.

		MODAL FREQUENCIES							
	Mode	1	2	3	4	5	6	7	8
4 cm Clamped End	Exp.	28.65	174.7	489.5	995.4	1439	2137	3191	4105
	ABAQUS	28.6	175.5	498.2	995	1502	2151	3189	4311
	$\Delta\%$	-017%	0.46%	1.78%	-0.04%	4.38%	0.66%	-0.06%	5.02%
8 cm Clamped End	Exp.	27.73	159.4	485.5	711.7	1274	1818	2680	3509
	ABAQUS	26.86	159.5	463.7	713.8	1309	1842	2646	3445
	$\Delta\%$	-3.13%	0.08%	-4.49%	0.30%	2.80%	1.33%	-1.26%	-1.84%

Table 4.18 Comparison of experimental ABAQUS modal frequencies for the 4-cm and 8-cm clamped-end notched beams.

The ABAQUS results are within 5% of the experimental results. This deviation could be further reduced by a mesh convergence study. ABAQUS could be useful in studying the modal characteristics of the eccentrically-located notched beam, where the nonlinear behavior is augmented. The first eight modal shapes computed by

the ABAQUS method for the centrally located 8-cm clamped-end notched beam are shown below.

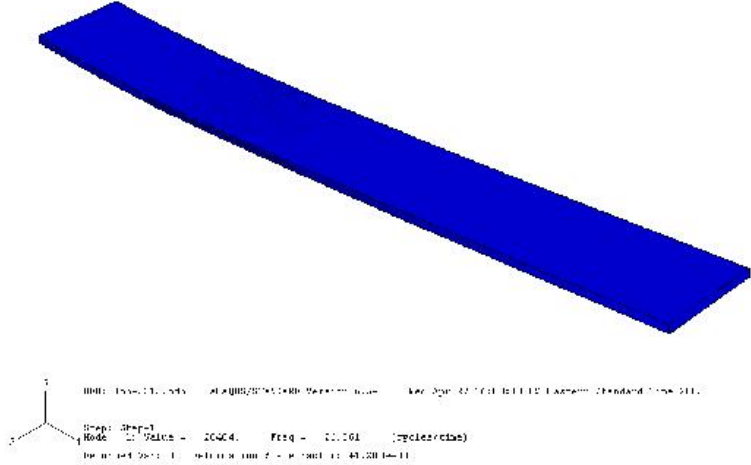


Figure 4.26 ABAQUS bending mode 1.

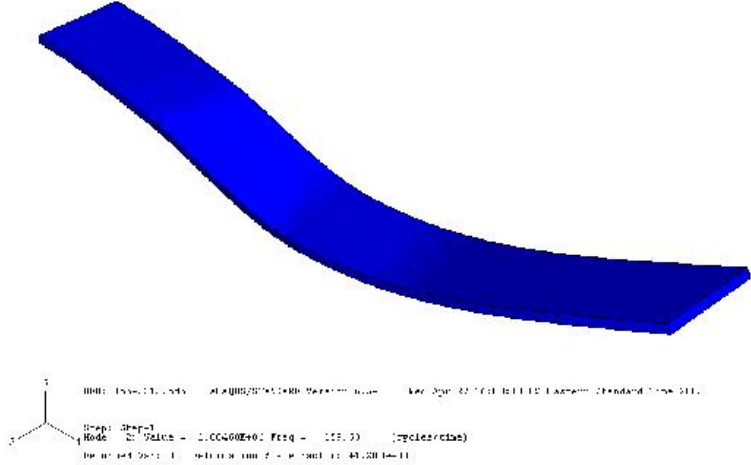


Figure 4.27 ABAQUS bending mode 2.

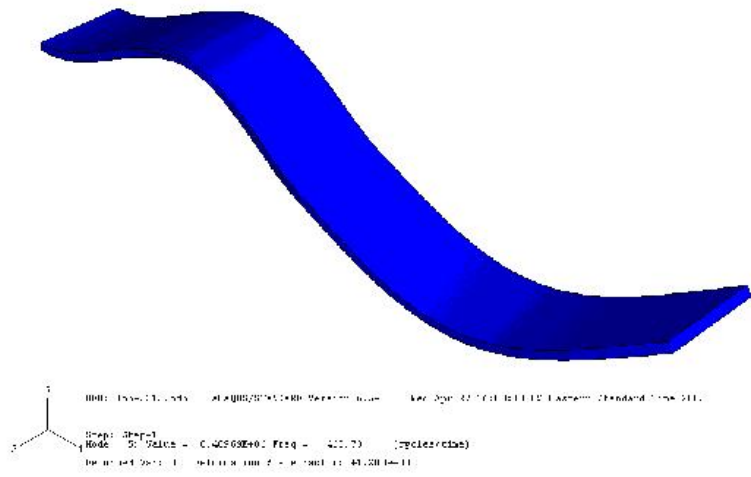


Figure 4.28 ABAQUS bending mode 3.

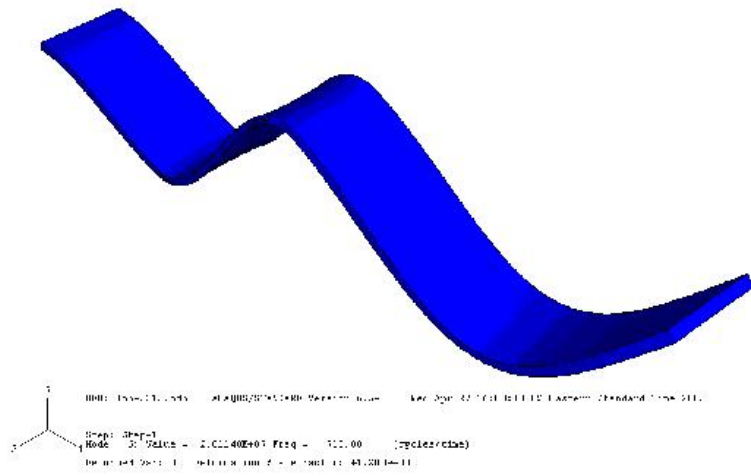


Figure 4.29 ABAQUS bending mode 4.

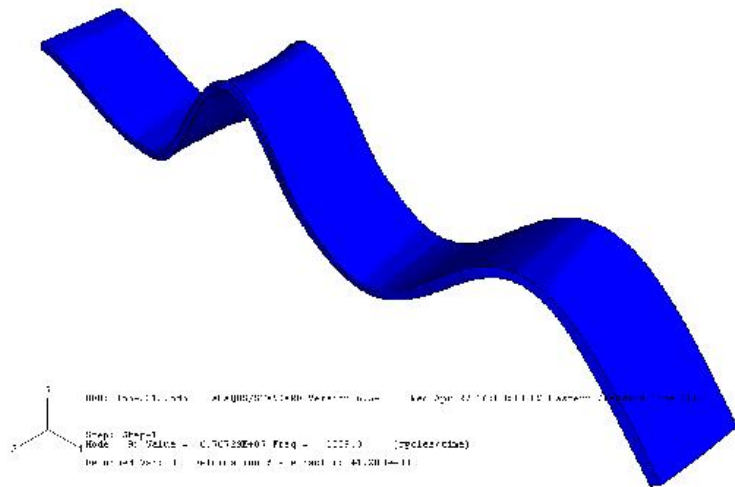


Figure 4.30 ABAQUS bending mode 5.

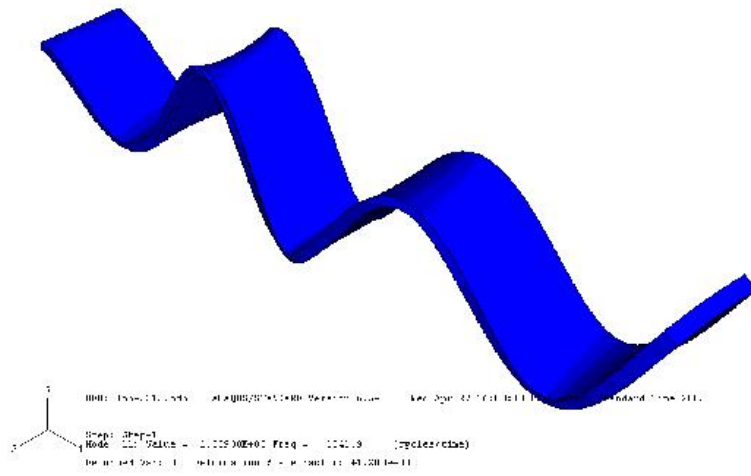


Figure 4.31 ABAQUS bending mode 6.

V. Conclusions and Recommendations for Further Study

The present study investigated the natural frequency response of Al 2024-T3 cantilever beams containing notches of varying length and location. The diagnostic approaches used were modal analysis and finite element methods. The natural frequency trends were examined according to notch length, location along the length of the beam, and location with respect to the beam axis. The following conclusions have been drawn.

1. The natural frequency of the beam decreased as the notch length increases.
2. The percent decrease from the notchless case of the natural frequency of beams with inclusions was generally greater for a beam containing notch located on the beam axis than off-axis.
3. Eccentric notches and centered notches can be sized using the natural frequency deviation from the notchless case.
4. The trend of the natural frequency deviation from the notchless case provides information on the location of the notch in the case of eccentrically located notches.
6. The eccentric notches intersect more points of maximum shear and points of maximum curvature of the modal shapes than the centered nodes.
7. The acoustic horn introduced interference in the FRF plot of the notchless case that was not present in the FRF plot of the piezoelectric-actuator excited notchless beam. However, it is difficult to attribute the interference specifically to the acoustic horn or to notch contact.
8. The Cobb-Durham code is a simple finite element model, which produces good estimates for the natural frequencies of the notched beams for both the eccentric and the centered notch cases.

9. ABAQUS is an effective modeling tool to model the frequency response of beams containing notches.

Further experimentation should be conducted to characterize the behavior of the acoustic horn. The acoustic horn is a less expensive tool than the piezoelectric actuator, but it can cause interference in sensitive measurements. If this influence were characterized, the horn would be available for more applications and would provide better results.

Likewise, the notch sublaminates need to be modeled, to determine that notch surface contact does indeed occur, and to determine the circumstances under which interference may be attributed to this surfact contact.

With respect to this study, the experiment may be performed using centrally notched beams with the same thickness as the eccentric notches in this study. The direct comparison would allow verification of the code predictions, as well as perhaps more insight into the influence of notch depth.

Other methods of locating notches are possible. An experiment could be conducted to measure the frequency response in the time domain and use a spectral element model to observe the stress wave as it propagates down the length of the beam. The stress wave is magnified at the crack tips, and thereby can indicate both notch size and location. To reexamine the notch depth, the beams of this experiment could be tested with the lower sublaminate facing the laser vibrometer. This orientation may results in different measured modal frequencies and thereby may offer a model for notch depth.

*Appendix A. Mode Shapes and Frequencies of the Eccentrically
Notched Beams*

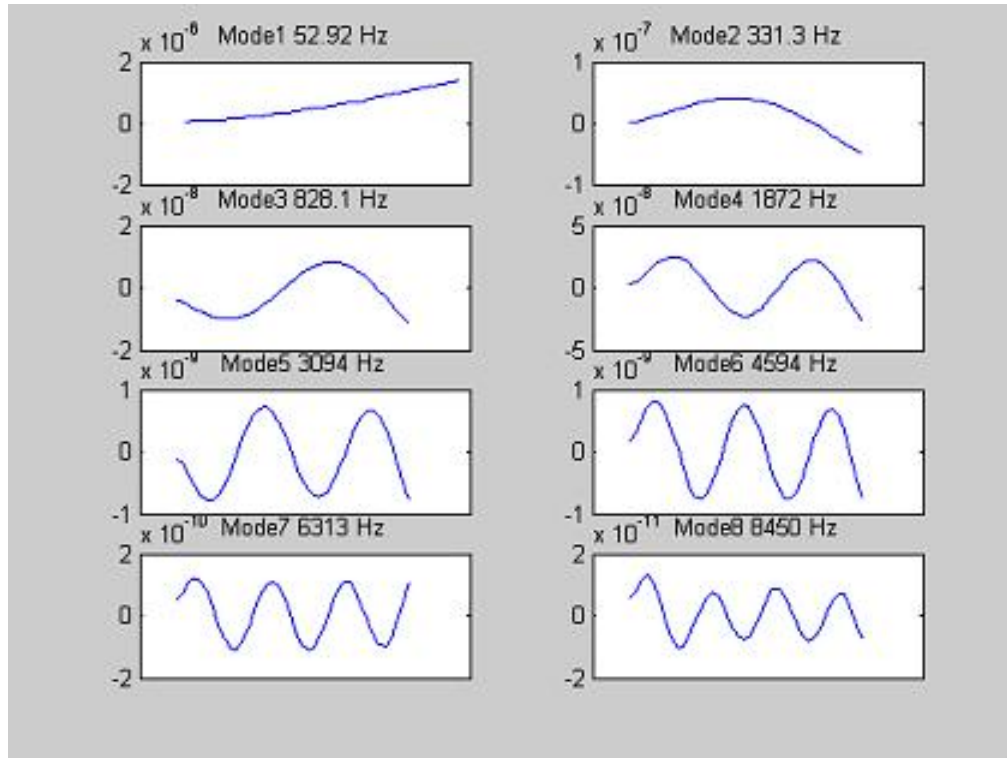


Figure A.1 First eight mode shapes and modal frequencies of the notchless beam.

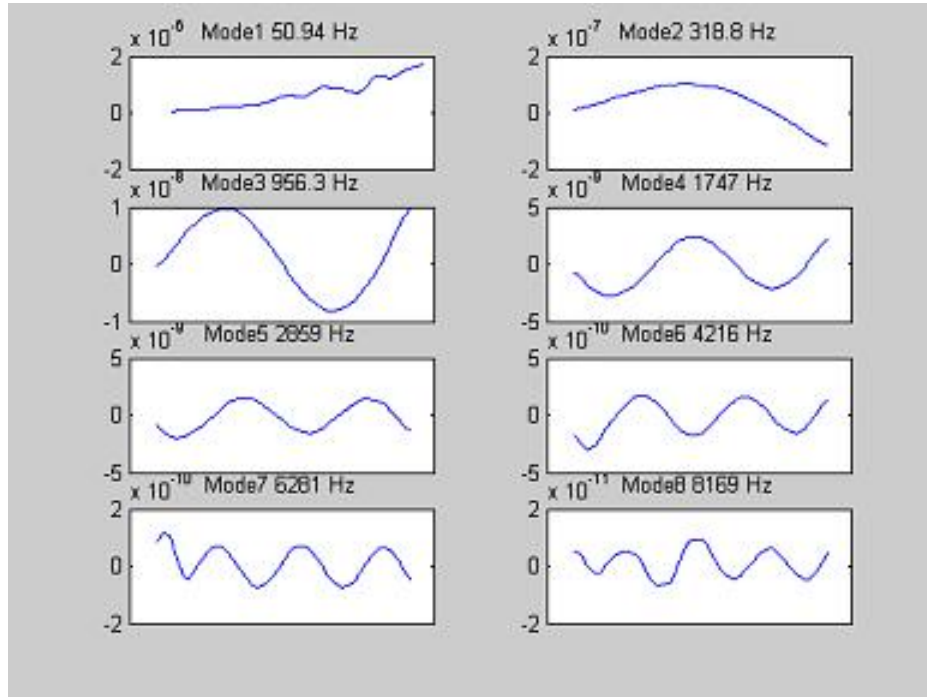


Figure A.2 First eight mode shapes and modal frequencies of the beam containing the 4-cm notch at the clamped end.

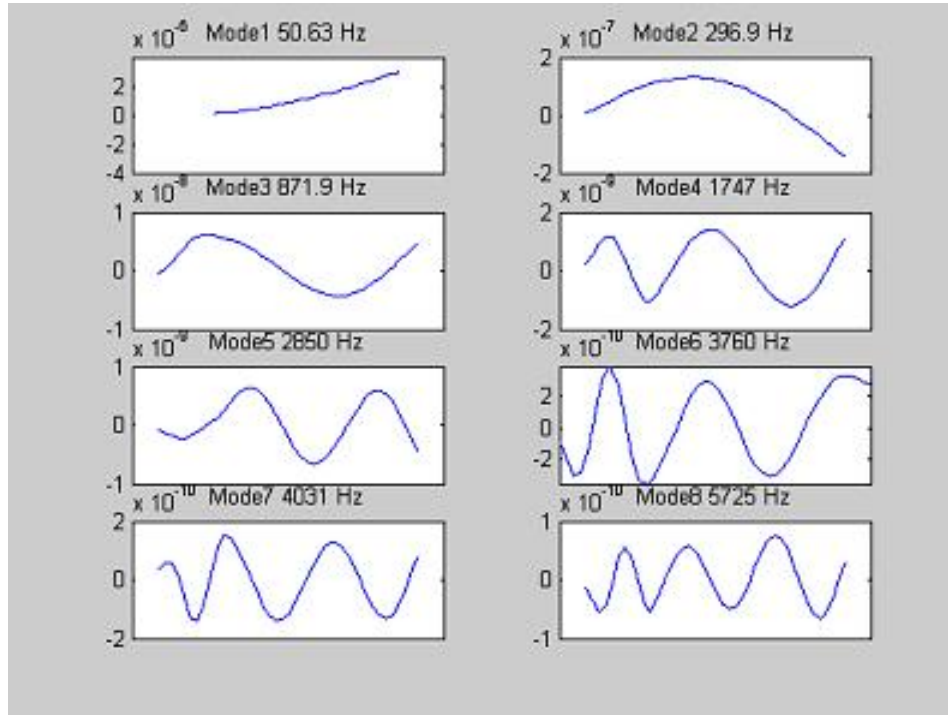


Figure A.3 First eight mode shapes and modal frequencies of the beam containing the 8-cm notch at the clamped end.

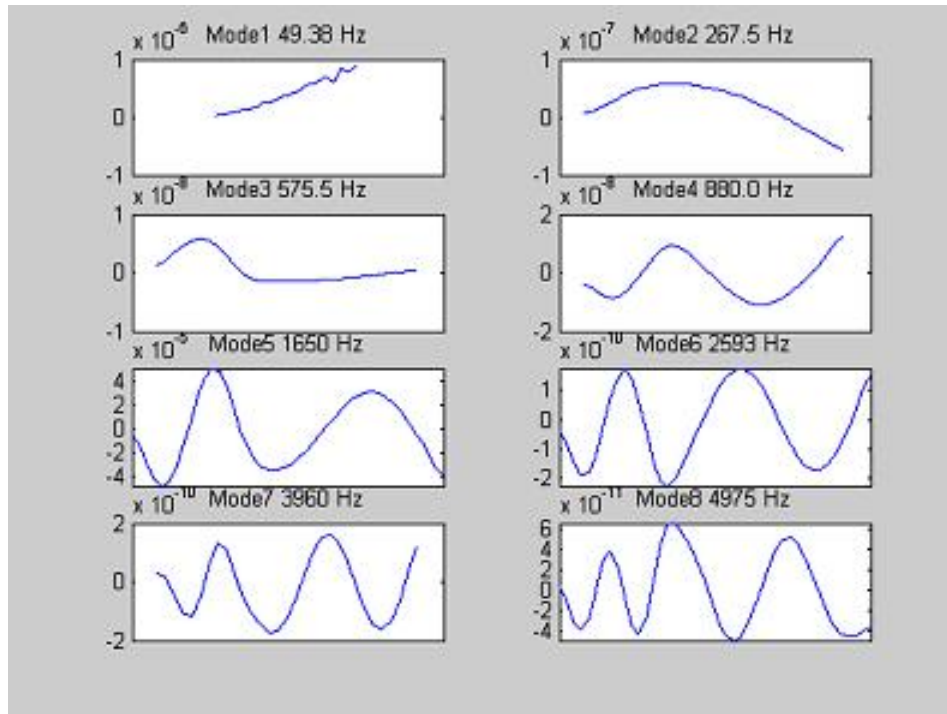


Figure A.4 First eight mode shapes and modal frequencies of the beam containing the 12-cm notch at the clamped end.

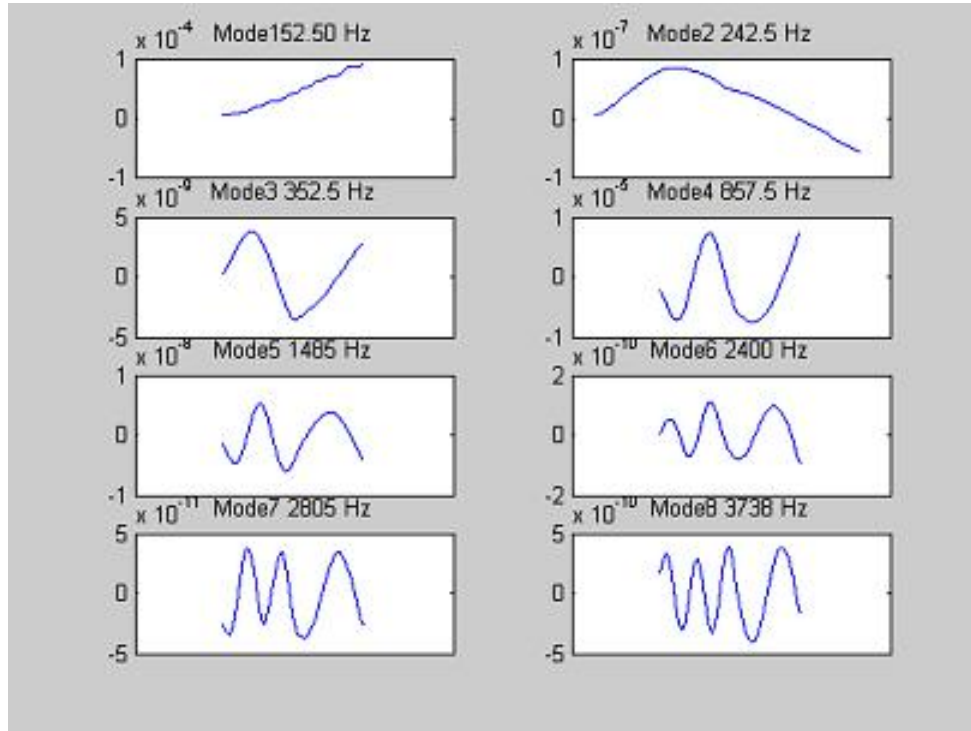


Figure A.5 First eight mode shapes and modal frequencies of the beam containing the 16-cm notch at the clamped end.

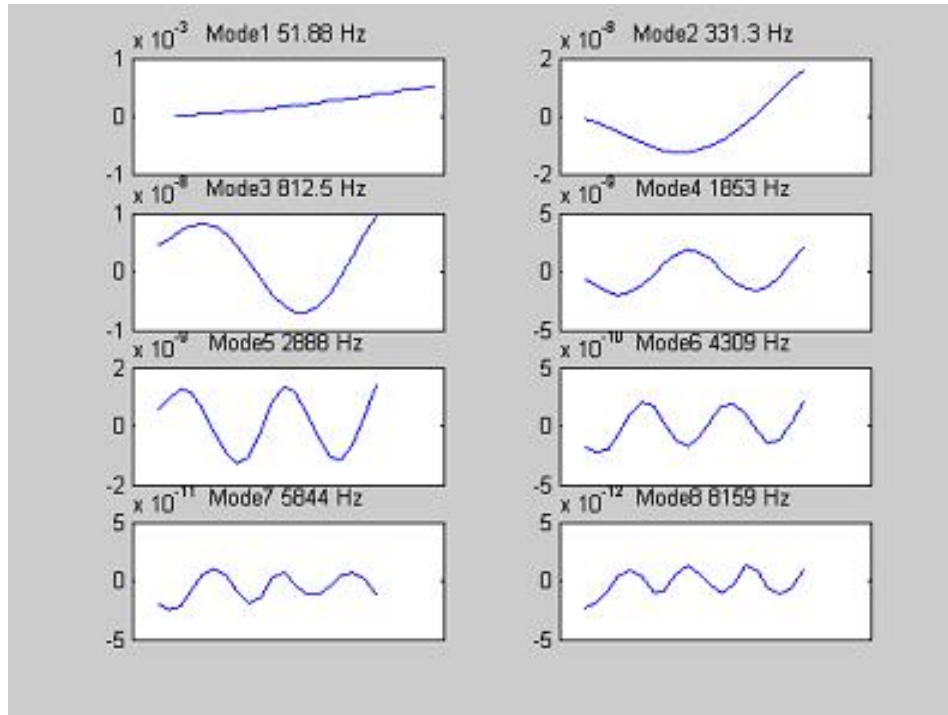


Figure A.6 First eight mode shapes and modal frequencies of the beam containing the 4-cm notch in the middle.

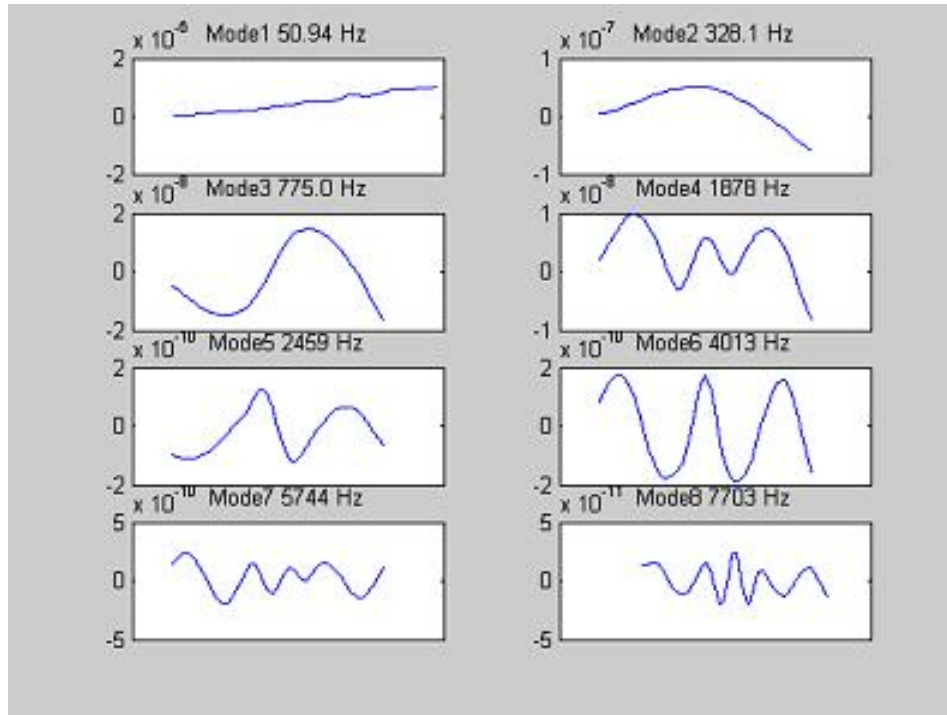


Figure A.7 First eight mode shapes and modal frequencies of the beam containing the 8-cm notch in the middle.

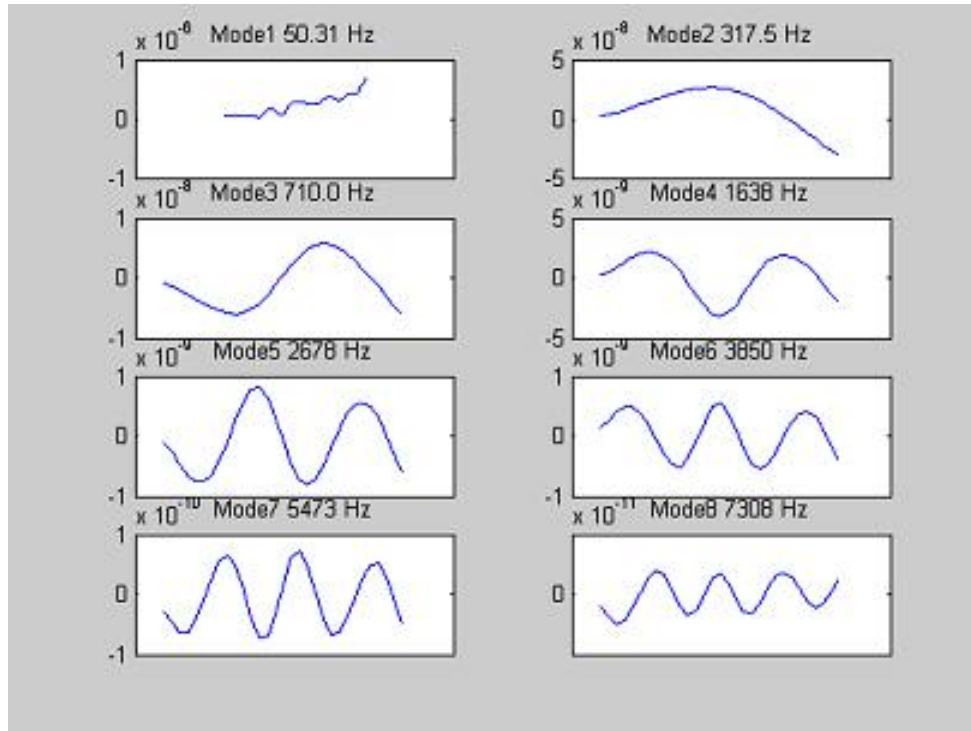


Figure A.8 First eight mode shapes and modal frequencies of the beam containing the 12-cm notch in the middle.

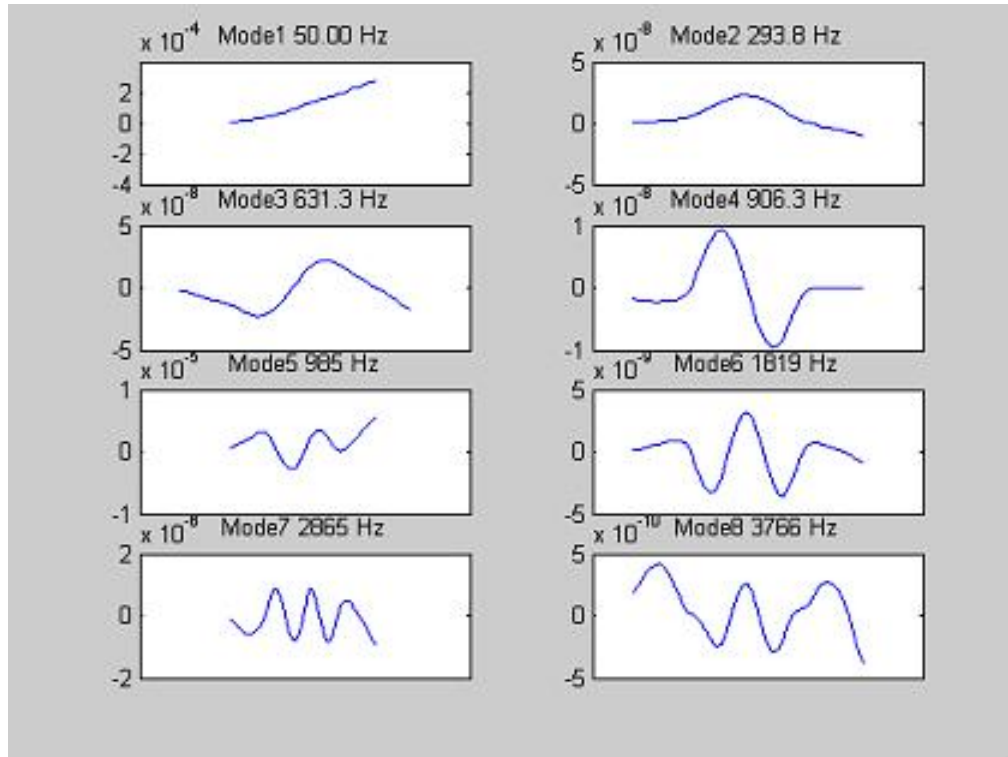


Figure A.9 First eight mode shapes and modal frequencies of the beam containing the 16-cm notch in the middle.

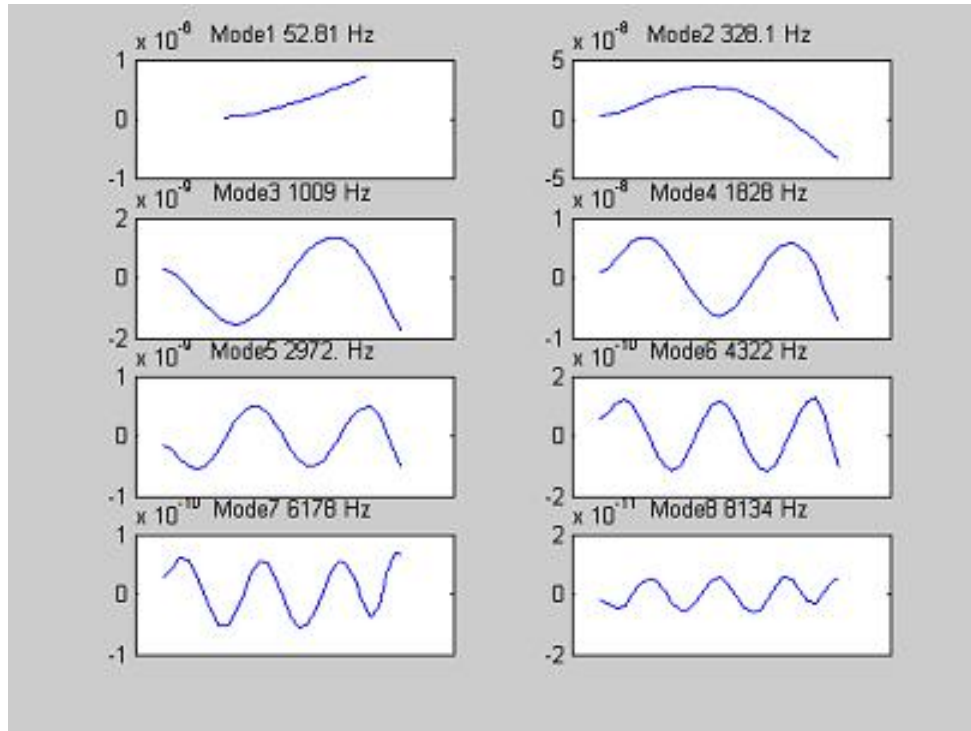


Figure A.10 First eight mode shapes and modal frequencies of the beam containing the 4-cm notch at the free end.

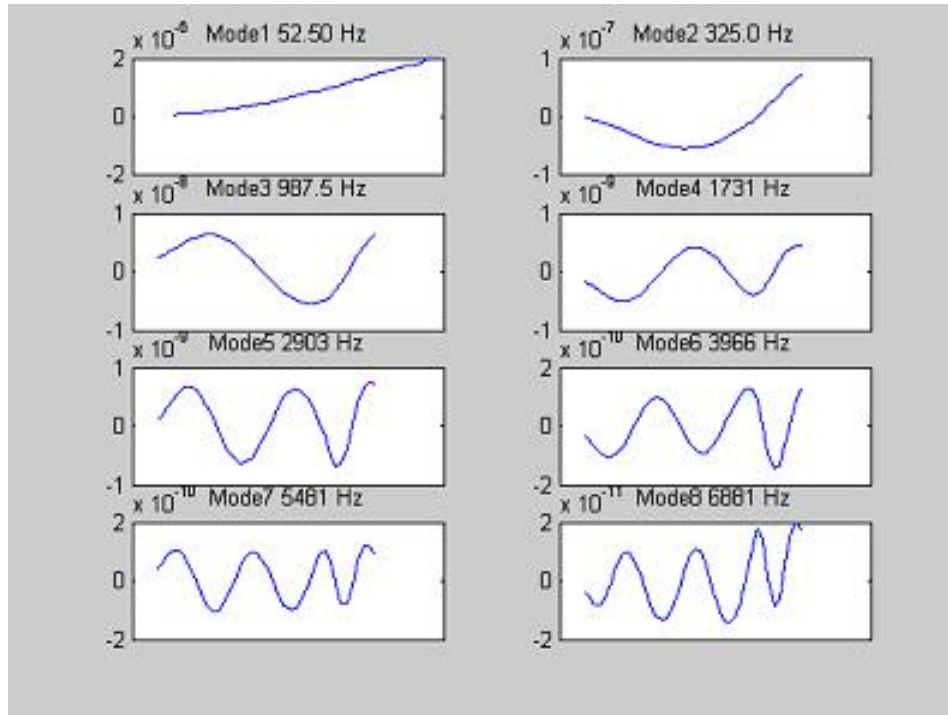


Figure A.11 First eight mode shapes and modal frequencies of the beam containing the 8-cm notch at the free end.

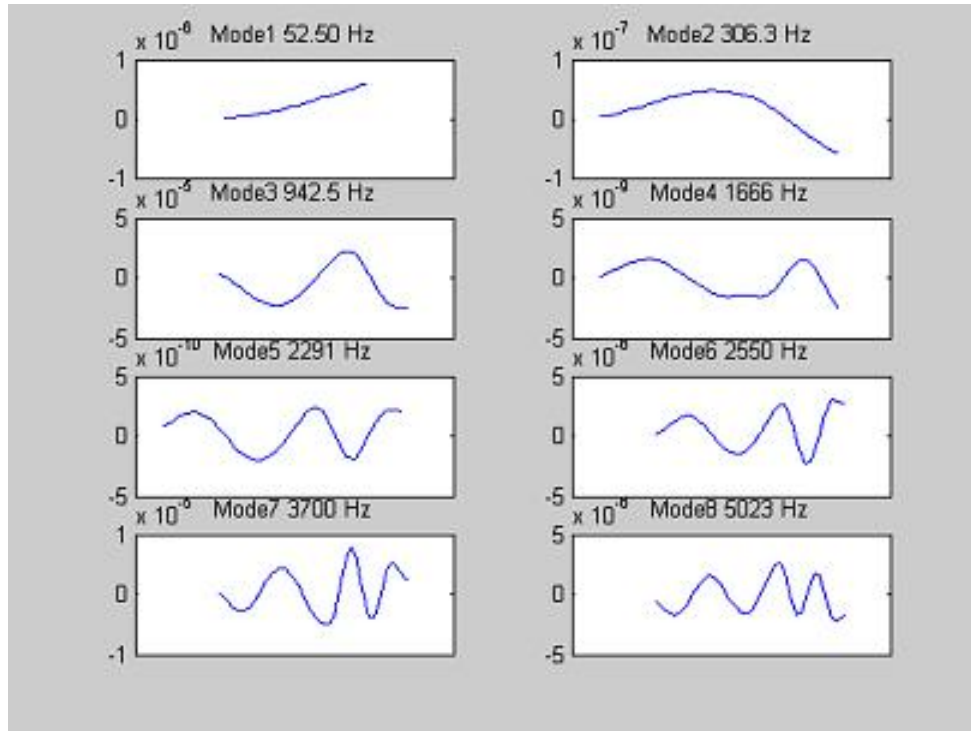


Figure A.12 First eight mode shapes and modal frequencies of the beam containing the 12-cm notch at the free end.

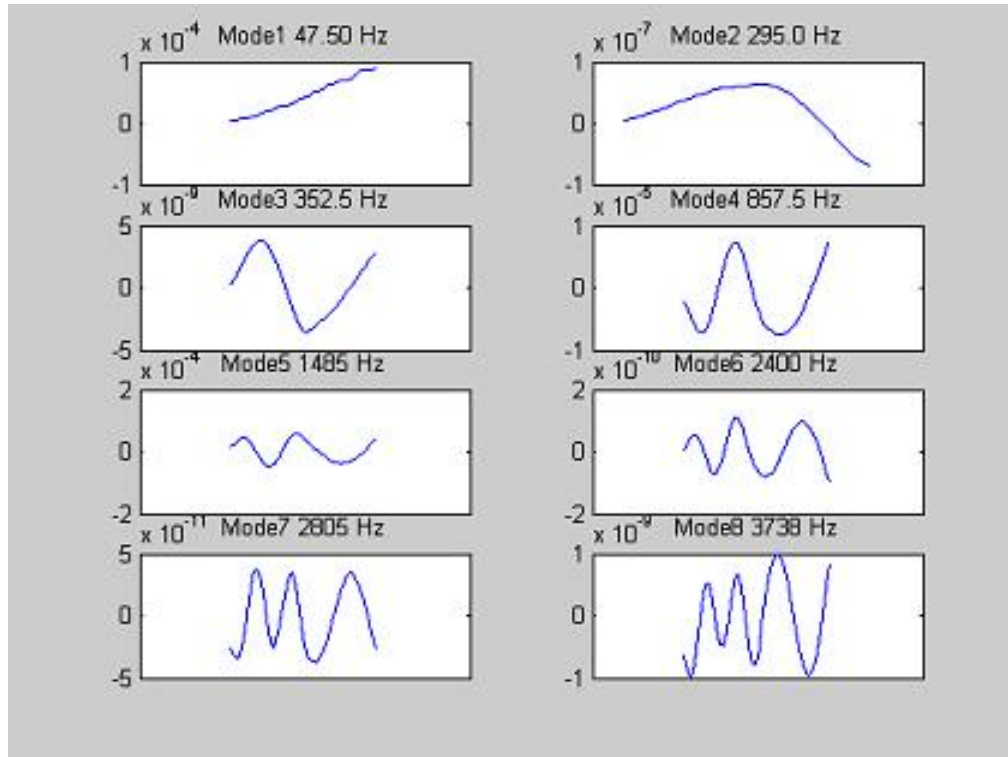


Figure A.13 First eight mode shapes and modal frequencies of the beam containing the 16-cm notch at the free end.

Appendix B. Cobb-Durham Code

```
% FEM analytical solution
% Written by Dr Richard Cobb
% Modified by Frances Durham

% This code computes the natural frequencies and mode shapes of a
% cantilevered beam containing an eccentric notch.

beam_length = 12/12; % ft
h = .25/12 ;      % ft
h_u = h/4-0.006/12; h_l = 3*h/4-0.006/12;
b = 1.5/12; % ft
E = 10000000*12*12; % lb-f/ft^2 (10000 ksi)
rho = 0.0975/32.174*12^3; % slug/ft^3

n_els = 36; n_nodes = n_els + 1; j = n_nodes*2;
c = .000001; % assume lightly damped

A(1:n_els) = b*h; I(1:n_els) = b*(h^3)/12; L(1:n_els) =
beam_length/n_els;

n_crack_tip_els = 3; crack_length_cm = input('Length of crack in cm:
'); crack_length = crack_length_cm/2.54/12; location =
input('Location of crack (1) clamped end (2) middle (3) free end:
'); n_crack_els = crack_length_cm*6/4; L_crack =
crack_length/n_crack_els; L_crack_tip_els=L_crack; if (location==1)
```

```

L_undamaged = (beam_length - crack_length - n_crack_tip_els*L_crack_tip_els)/(n_els);
L(1:n_crack_els) = L_crack;
L(n_crack_els+1:n_crack_els+n_crack_tip_els) = L_crack_tip_els;
L(n_crack_els+n_crack_tip_els+1:n_els) = L_undamaged;
crackel1=1;
crackel2=n_crack_els;
for k=1:n_crack_els
    I(k) = b*(h_u^3+h_l^3)/12;
    A(k) = b*(h_u+h_l);
end
slope = (I(n_crack_els+1)-I(n_crack_els))/(n_crack_tip_els+1);
for k=1:n_crack_tip_els
    I(n_crack_els+k) = I(n_crack_els)+k*slope;
end
end if (location==2)
L_undamaged = (beam_length-crack_length-2*n_crack_tip_els*L_crack_tip_els)/(n_els);
n_els_undamaged = n_els-n_crack_els-2*n_crack_tip_els;
L(1:n_els_undamaged/2)=L_undamaged;
L(n_els_undamaged/2+1:n_els_undamaged/2+n_crack_tip_els) = L_crack_tip_els;
L(n_els_undamaged/2+n_crack_tip_els+1:n_els_undamaged/2+n_crack_tip_els+n_crack_els) = L_crack;
L(n_els-n_els_undamaged/2-n_crack_tip_els+1:n_els-n_els_undamaged/2) = L_crack_tip_els;
L(n_els-n_els_undamaged/2:n_els) = L_undamaged;
crackel1=n_els_undamaged/2+n_crack_tip_els+1;
crackel2=crackel1+n_crack_els;
for k=n_els_undamaged/2+n_crack_tip_els+1:n_els_undamaged/2+n_crack_tip_els+n_crack_els
    I(k) = b*(h_u^3+h_l^3)/12;
    A(k) = b*(h_u+h_l);
end

```

```

slope = (I(1)-I(n_els_undamaged/2+n_crack_tip_els+1))/(n_crack_tip_els+2);
for k=1:n_crack_tip_els
    I(n_els_undamaged/2+k) = I(n_els_undamaged/2)-k*slope;
    I(n_els_undamaged/2+n_crack_tip_els+k) = I(n_els_undamaged/2+n_crack_tip_els+
end
end if (location==3)
    L_undamaged = (beam_length - crack_length-(n_crack_tip_els+1)*L_crack_tip_els)/(n
    L(1:n_els-n_crack_tip_els-n_crack_els-2)=L_undamaged;
    L(n_els-n_crack_tip_els-n_crack_els-1:n_els-n_crack_els-2)=L_crack_tip_els;
    L(n_els-n_crack_els-1:n_els-1)=L_crack;
    L(n_els)=L_crack_tip_els;
    crackel2=n_els-1;
    crackel1=crackel2-n_crack_els;
    for k=n_els-n_crack_els-1:n_els-1
        I(k) = b*(h_u^3+h_l^3)/12;
        A(k) = b*(h_u+h_l);
    end
    slope = (I(1)-I(n_els-1))/(n_crack_tip_els+1);
    for k=1:n_crack_tip_els
        I(n_els-n_crack_els-1-k)=I(n_els-1)+(n_crack_tip_els-k)*slope;
    end
end pos(1)=0; for k=1:n_els-1
    pos(k+1)=pos(k)+L(k);
end

M = zeros(j);K = zeros(j);

for i=1:2:j-3

```

```

k=(i+1)/2;
mel = (rho*A(k)*L(k)/420)*[156 22*L(k) 54 -13*L(k);...
    22*L(k) 4*(L(k)^2) 13*L(k) -3*(L(k)^2);...
    54 13*L(k) 156 -22*L(k);...
    -13*L(k) -3*(L(k)^2) -22*L(k) 4*(L(k)^2)];

kel = (E*I(k)/(L(k)^3))*[12 6*L(k) -12 6*L(k);...
    6*L(k) 4*(L(k)^2) -6*L(k) 2*(L(k)^2);...
    -12 -6*L(k) 12 -6*L(k);...
    6*L(k) 2*(L(k)^2) -6*L(k) 4*(L(k)^2)];

M(i:i+3,i:i+3) = M(i:i+3,i:i+3) + mel;
K(i:i+3,i:i+3) = K(i:i+3,i:i+3) + kel;
end

M = M(3:j,3:j); % Apply BC
K= K(3:j,3:j); C = K*c; F=zeros(n_els*2,1);
F(6)=1; % patched creates moment at 1.5 in -> node 3 -> DOF 6

%%%%%%%%%%%%
A=[zeros(n_els*2,n_els*2) eye(n_els*2);-M^-1*K -M^-1*C];
[asize,other]=size(A); C=eye(n_els*4); C=C(1:n_els*2,:);
[V,D]=eig(A); for i=1:asize
    Doh(i)=D(i,i);
    Dohabs(i)=abs(Doh(i))/2/pi;
end
%
```

```

figure(1) subplot(4,2,1) M1=V(:,asize)
m1hz=abs(D(asize,asize))/2/pi; mode1=M1(1:2:2*n_els);
mode1=real(mode1/max(mode1));
plot(pos,mode1);title(sprintf('Mode1 %3.3f ',m1hz))
set(gca,'XTick',[])

%
subplot(4,2,2) M2=V(:,asize-2) m2hz=abs(D(asize-2,asize-2))/2/pi
mode2=M2(1:2:2*n_els); mode2=real(mode2/max(mode2))
plot(pos,mode2);title(sprintf('Mode2 %3.3f ',m2hz))
set(gca,'XTick',[])

i=0; p=0; mode2_crossedanti=0; mode2_crossednode=0; for k=2:n_els-1
    if mode2(k-1)<=mode2(k) & mode2(k+1)<=mode2(k)
        i=i+1;
        mode2_maxcurve(i)=pos(k);
        if k>=crackel1 & k<=crackel2
            mode2_crossedanti=mode2_crossedanti+1;
        end
    elseif mode2(k-1)>=mode2(k) & mode2(k+1)>=mode2(k)
        i=i+1;
        mode2_maxcurve(i)=pos(k);
        if k>=crackel1 & k<=crackel2
            mode2_crossedanti=mode2_crossedanti+1;
        end
    end
end
if mode2(k)<=0 & mode2(k+1)>=0
    p=p+1;

```

```

        mode2_nodes(p)=pos(k);
        mode2_crossednode=mode2_crossednode+1;
elseif mode2(k)>=0 & mode2(k+1)<=0
        p=p+1;
        mode2_nodes(p)=pos(k);
        mode2_crossednode=mode2_crossednode+1;
end
end

%
subplot(4,2,3) M3=V(:,asize-4); m3hz=abs(D(asize-4,asize-4))/2/pi
mode3=M3(1:2:2*n_els); mode3=real(mode3/max(mode3));
plot(pos,mode3);title(sprintf('Mode3 %3.2f ',m3hz))
set(gca,'XTick',[])
%set(gca,'YTick',[])

i=0; p=0; mode3_crossedanti=0; mode3_crossednode=0; for k=3:n_els-1
    if mode3(k-1)<=mode3(k) & mode3(k+1)<=mode3(k)
        i=i+1;
        mode3_maxcurve(i)=pos(k);
        if k>=crackel1 & k<=crackel2
            mode3_crossedanti=mode3_crossedanti+1;
        end
    elseif mode3(k-1)>=mode3(k) & mode3(k+1)>=mode3(k)
        i=i+1;
        if k>=crackel1 & k<=crackel2
            mode3_crossedanti=mode3_crossedanti+1;
        end
    end
end

```

```

        mode3_maxcurve(i)=pos(k);
    end
    if mode3(k)<=0 & mode3(k+1)>=0
        p=p+1;
        mode3_nodes(p)=pos(k);
        mode3_crossednode=mode3_crossednode+1;
    elseif mode3(k)>=0 & mode3(k+1)<=0
        p=p+1;
        mode3_nodes(p)=pos(k);
        mode3_crossednode=mode3_crossednode+1;
    end
end

%
subplot(4,2,4) M4=V(:,asize-6); m4hz=abs(D(asize-6,asize-6))/2/pi
mode4=M4(1:2:2*n_els); mode4=real(mode4/max(mode4));
plot(pos,mode4);title(sprintf('Mode4 %3.2f ',m4hz))
set(gca,'XTick',[])
%set(gca,'YTick',[])

i=0; p=0; mode4_crossedanti=0; mode4_crossednode=0; for k=2:n_els-1
    if mode4(k-1)<=mode4(k) & mode4(k+1)<=mode4(k)
        i=i+1;
        mode4_maxcurve(i)=pos(k);
        if k>=crackel1 & k<=crackel2
            mode4_crossedanti=mode4_crossedanti+1;
        end
    end
end

```

```

elseif mode4(k-1)>=mode4(k) & mode4(k+1)>=mode4(k)
    i=i+1;
    mode4_maxcurve(i)=pos(k);
    if k>=crackel1 & k<=crackel2
        mode4_crossedanti=mode4_crossedanti+1;
    end
end
end
if mode4(k)<=0 & mode4(k+1)>=0
    p=p+1;
    mode4_nodes(p)=pos(k);
    mode4_crossednode=mode4_crossednode+1;
elseif mode4(k)>=0 & mode4(k+1)<=0
    p=p+1;
    mode4_nodes(p)=pos(k);
    mode4_crossednode=mode4_crossednode+1;
end
end
end

%
subplot(4,2,5) M5=V(:,asize-8); m5hz=abs(D(asize-8,asize-8))/2/pi
mode5=M5(1:2:2*n_els); mode5=real(mode5/max(mode5));
plot(pos,mode5);title(sprintf('Mode5 %3.1f ',m5hz))
set(gca,'XTick',[])
%set(gca,'YTick',[])

i=0; p=0; mode5_crossedanti=0; mode5_crossednode=0; for k=2:n_els-1
    if mode5(k-1)<=mode5(k) & mode5(k+1)<=mode5(k)
        i=i+1;

```

```

mode5_maxcurve(i)=pos(k);
if k>=crackel1 & k<=crackel2
    mode5_crossedanti=mode5_crossedanti+1;
end
elseif mode5(k-1)>=mode5(k) & mode5(k+1)>=mode5(k)
    i=i+1;
    mode5_maxcurve(i)=pos(k);
    if k>=crackel1 & k<=crackel2
        mode5_crossedanti=mode5_crossedanti+1;
    end
end
end
if mode5(k)<=0 & mode5(k+1)>=0
    p=p+1;
    mode5_nodes(p)=pos(k);
    mode5_crossednode=mode5_crossednode+1;
elseif mode5(k)>=0 & mode5(k+1)<=0
    p=p+1;
    mode5_nodes(p)=pos(k);
    mode5_crossednode=mode5_crossednode+1;
end
end
end

%
subplot(4,2,6) M6=V(:,asize-10); m6hz=abs(D(asize-10,asize-10))/2/pi
mode6=M6(1:2:2*n_els); mode6=real(mode6/max(mode6));
plot(pos,mode6);title(sprintf('Mode6 %3.1f ',m6hz))
set(gca,'XTick',[])
%set(gca,'YTick',[])

```

```

i=0; p=0; mode6_crossedanti=0; mode6_crossednode=0; for k=2:n_els-1
    if mode6(k-1)<=mode6(k) & mode6(k+1)<=mode6(k)
        i=i+1;
        mode6_maxcurve(i)=pos(k);
        if k>=crackel1 & k<=crackel2
            mode6_crossedanti=mode6_crossedanti+1;
        end
    elseif mode6(k-1)>=mode6(k) & mode6(k+1)>=mode6(k)
        i=i+1;
        mode6_maxcurve(i)=pos(k);
        if k>=crackel1 & k<=crackel2
            mode6_crossedanti=mode6_crossedanti+1;
        end
    end
end
if mode6(k)<=0 & mode6(k+1)>=0
    p=p+1;
    mode6_nodes(p)=pos(k);
    mode6_crossednode=mode6_crossednode+1;
elseif mode6(k)>=0 & mode6(k+1)<=0
    p=p+1;
    mode6_nodes(p)=pos(k);
    mode6_crossednode=mode6_crossednode+1;
end
end

%
subplot(4,2,7) M7=V(:,asize-12); m7hz=abs(D(asize-12,asize-12))/2/pi

```

```

mode7=M7(1:2:2*n_els); mode7=real(mode7/max(mode7));
plot(pos,mode7);title(sprintf('Mode7 %3.1f ',m7hz))
set(gca,'XTick',[])
%set(gca,'YTick',[])

i=0; p=0; mode7_crossedanti=0; mode7_crossednode=0; for k=2:n_els-1
    if mode7(k-1)<=mode7(k) & mode7(k+1)<=mode7(k)
        i=i+1;
        mode7_maxcurve(i)=pos(k);
        if k>=crackel1 & k<=crackel2
            mode7_crossedanti=mode7_crossedanti+1;
        end
    elseif mode7(k-1)>=mode7(k) & mode7(k+1)>=mode7(k)
        i=i+1;
        mode7_maxcurve(i)=pos(k);
        if k>=crackel1 & k<=crackel2
            mode7_crossedanti=mode7_crossedanti+1;
        end
    end
end
if mode7(k)<=0 & mode7(k+1)>=0
    p=p+1;
    mode7_nodes(p)=pos(k);
    mode7_crossednode=mode7_crossednode+1;
elseif mode7(k)>=0 & mode7(k+1)<=0
    p=p+1;
    mode7_nodes(p)=pos(k);
    mode7_crossednode=mode7_crossednode+1;
end
end

```

```

end

%
subplot(4,2,8) M8=V(:,asize-14); m8hz=abs(D(asize-14,asize-14))/2/pi
mode8=M8(1:2:2*n_els); mode8=real(mode8/max(mode8));
plot(pos,mode8);title(sprintf('Mode8 %3.1f ',m8hz))
set(gca,'XTick',[])
%set(gca,'YTick',[])

i=0; p=0; mode8_crossedanti=0; mode8_crossednode=0; for k=2:n_els-1
    if mode8(k-1)<=mode8(k) & mode8(k+1)<=mode8(k)
        i=i+1;
        mode8_maxcurve(i)=pos(k);
        if k>=crackel1 & k<=crackel2
            mode8_crossedanti=mode8_crossedanti+1;
        end
    elseif mode8(k-1)>=mode8(k) & mode8(k+1)>=mode8(k)
        i=i+1;
        mode8_maxcurve(i)=pos(k);
        if k>=crackel1 & k<=crackel2
            mode8_crossedanti=mode8_crossedanti+1;
        end
    end
end
if mode8(k)<=0 & mode8(k+1)>=0
    p=p+1;
    mode8_nodes(p)=pos(k);
    mode8_crossednode=mode8_crossednode+1;
elseif mode8(k)>=0 & mode8(k+1)<=0

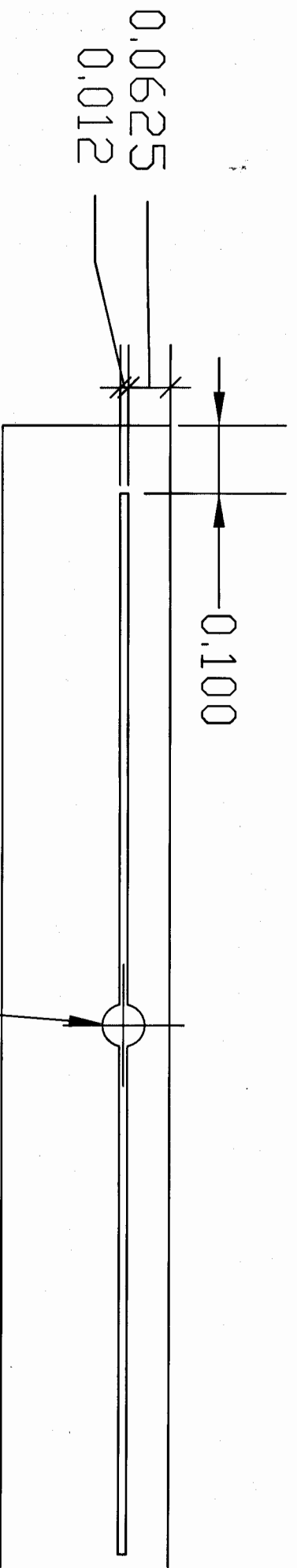
```

```
        p=p+1;
        mode8_nodes(p)=pos(k);
        mode8_crossednode=mode8_crossednode+1;
    end
end

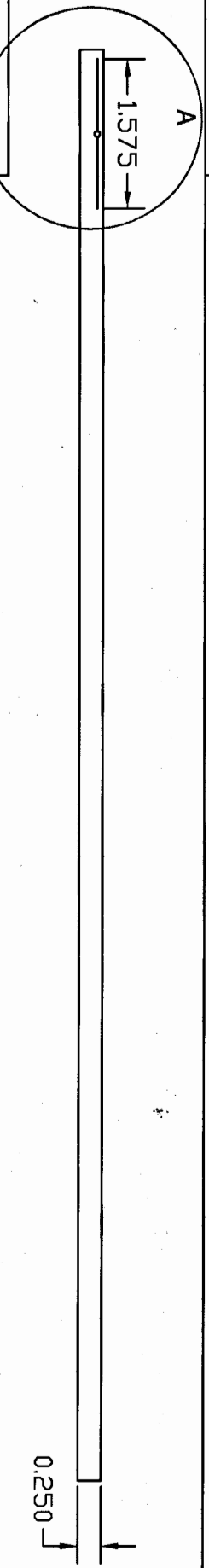
%
```

Appendix C. Beam Drawings

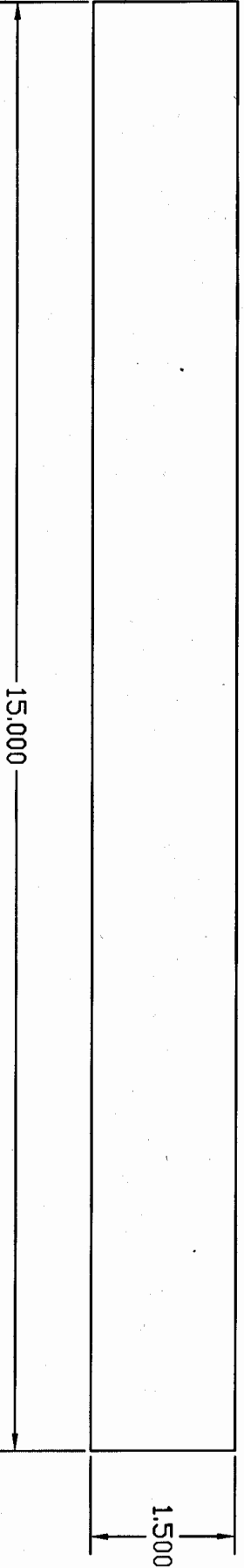
The following pages display diagrams created by Aaron Chmiel of the eccentrically notched beams. The dimensions are in inches.



Detail A



Elevation



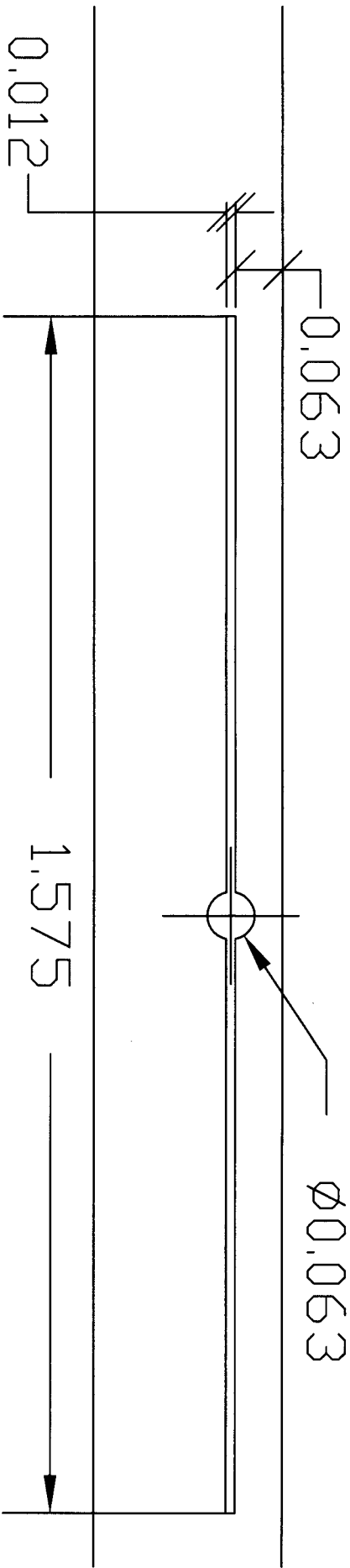
Plan

4cm notch, free end
Aaron Chmiel
aaron.chmiel@afit.edu

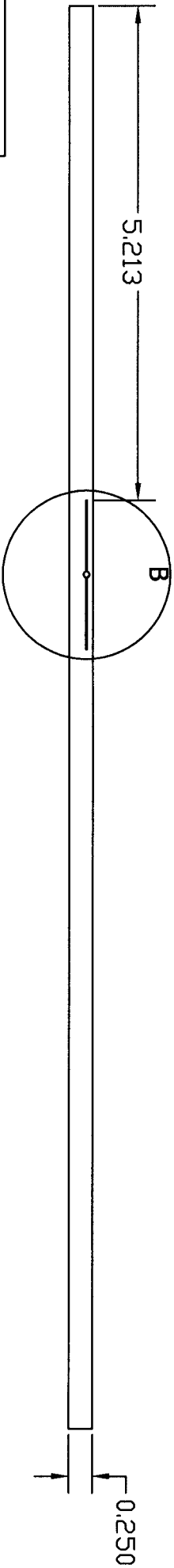
Aluminum 2024-O

All dimensions in inches

All tolerances +/- 0.005

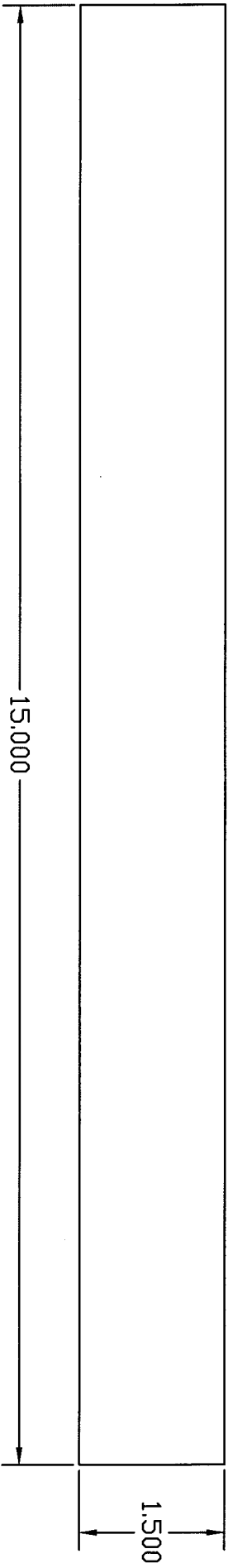


Detail B



Elevation

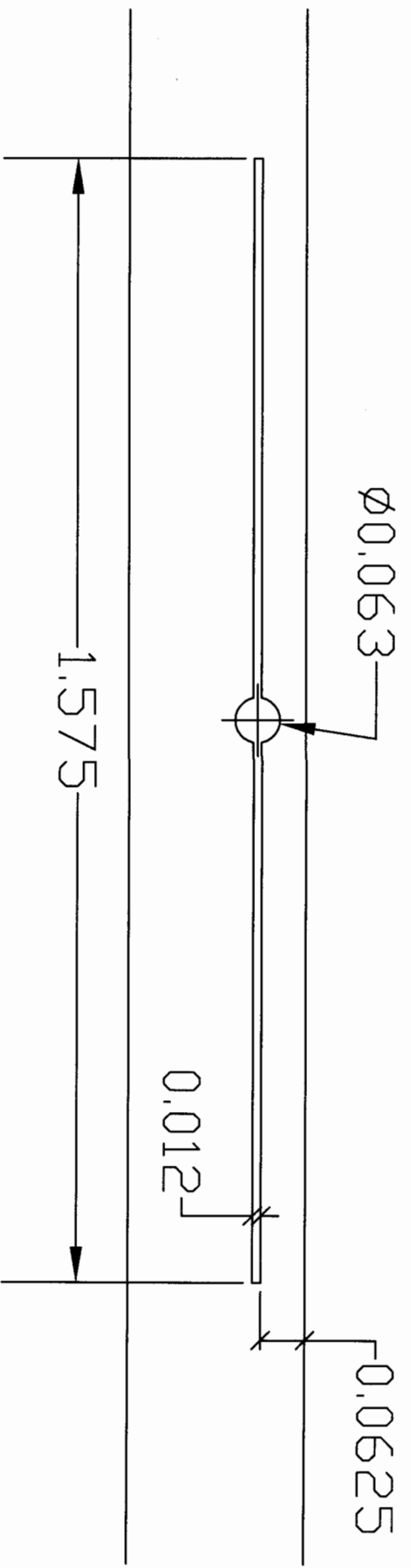
Plan



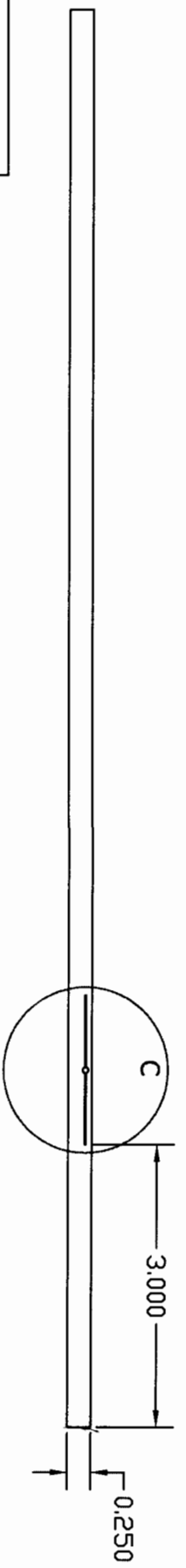
Aluminum 2024-O

All dimensions in inches

All tolerances +/- 0.005

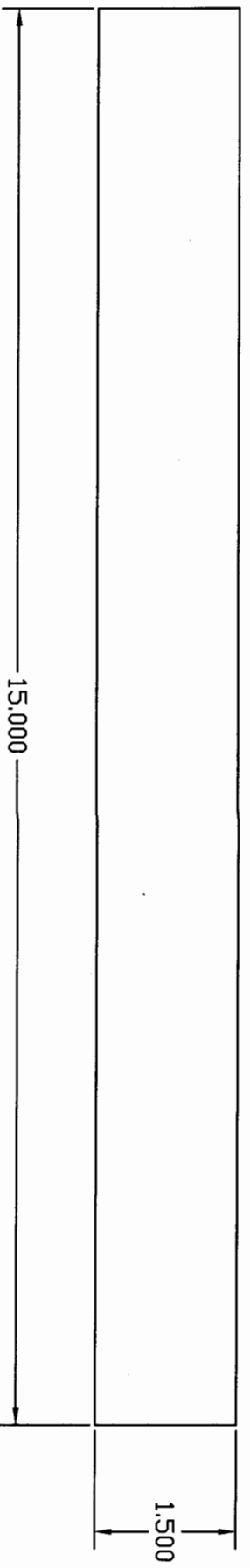


Detail C



Elevation

Plan

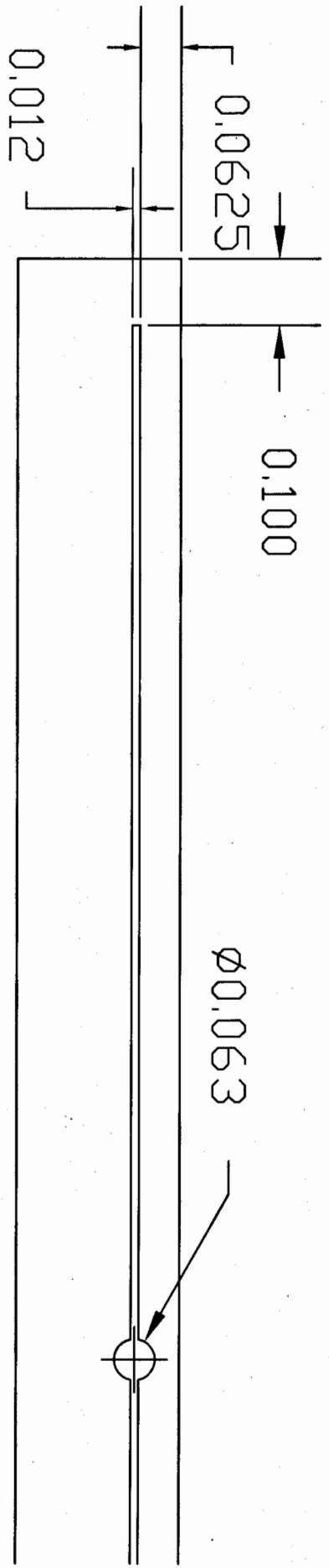


Aluminum 2024-O

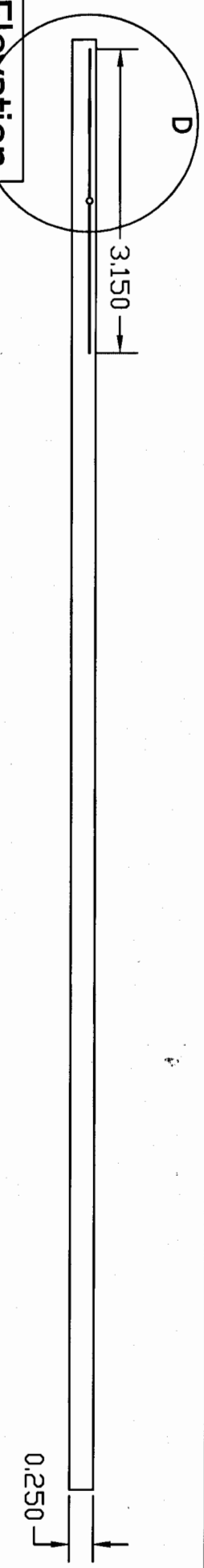
All dimensions in inches

All tolerances +/- 0.005

4cm notch, fixed end
Aaron Chmiel
aaron.chmiel@afit.edu

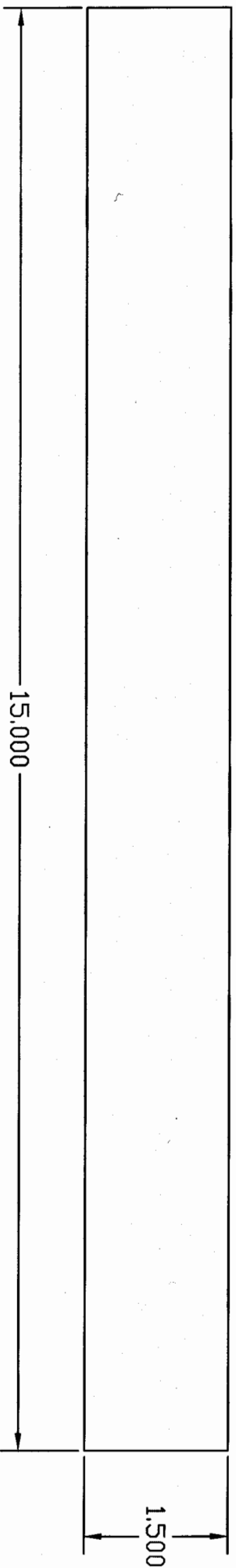


Detail D



Elevation

Plan

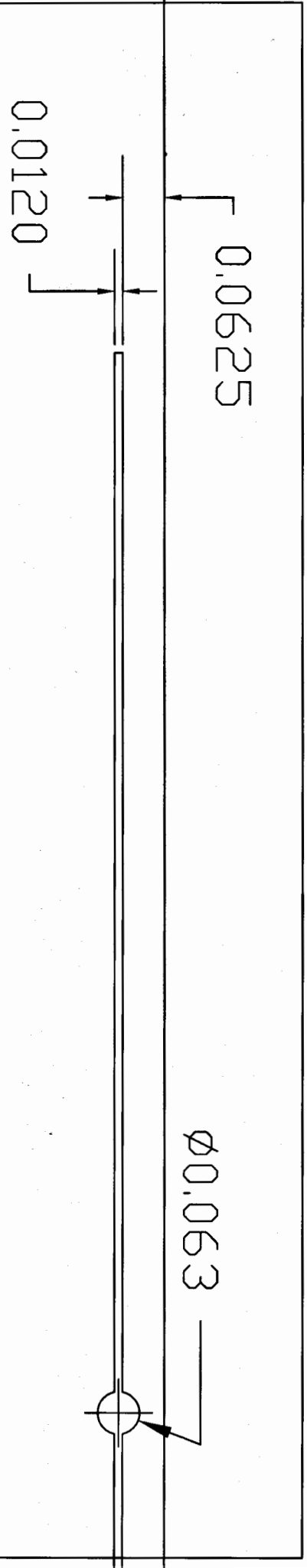


Aluminum 2024-O

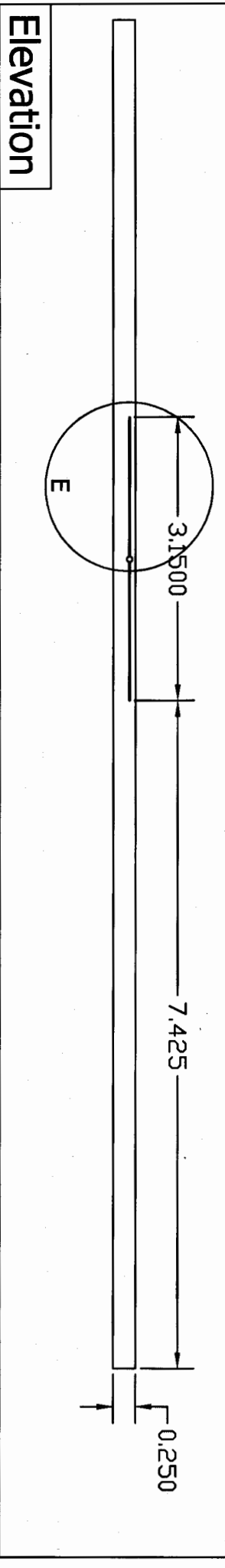
All dimensions in inches

All tolerances +/- 0.005

8cm notch, free end
Aaron Chmiel
aaron.chmiel@afit.edu

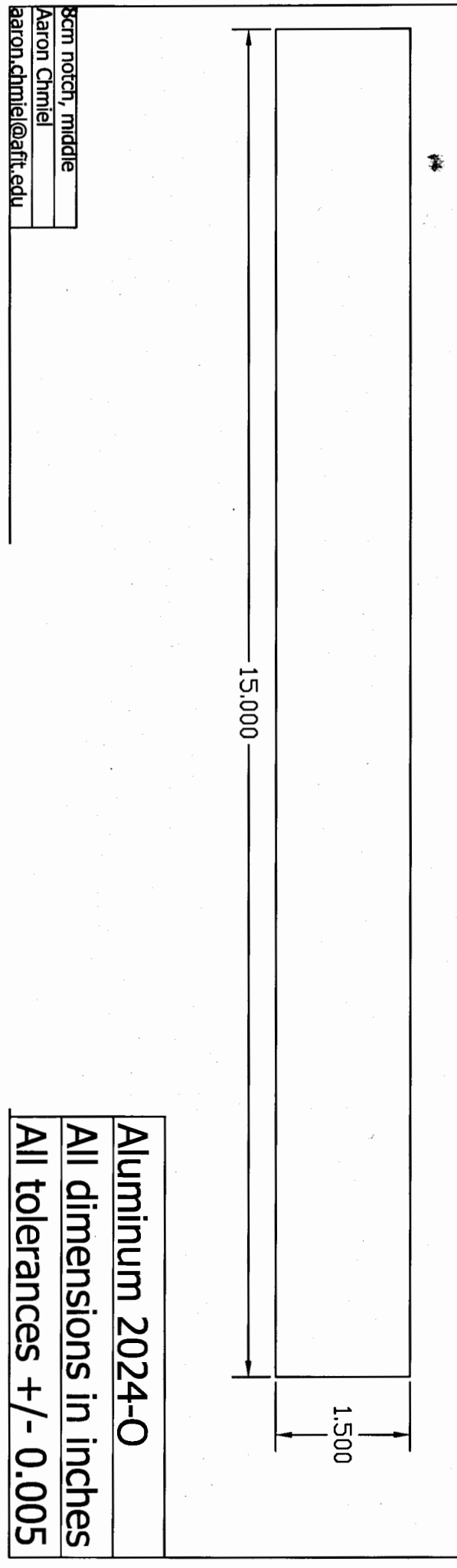


Detail E



Elevation

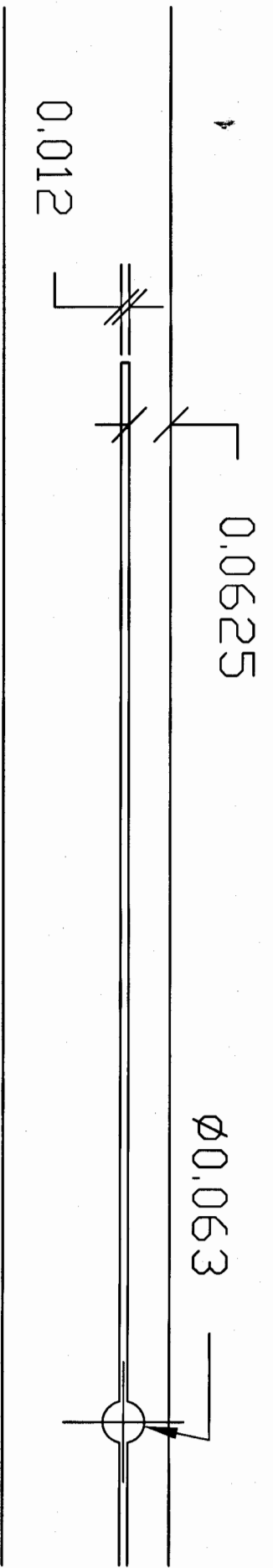
Plan



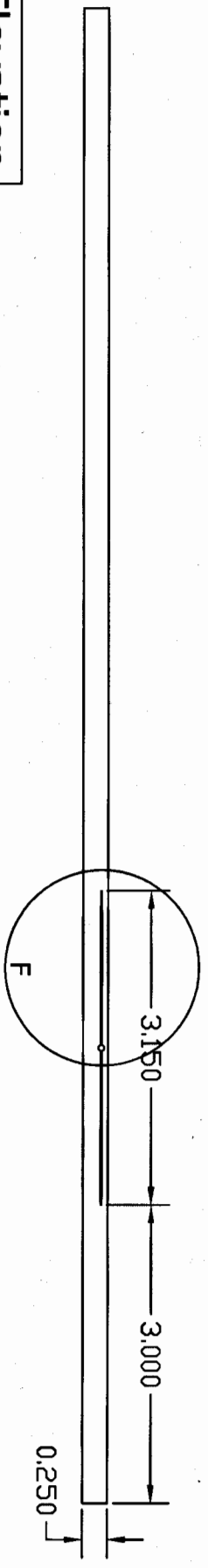
Aluminum 2024-O

All dimensions in inches

All tolerances +/- 0.005

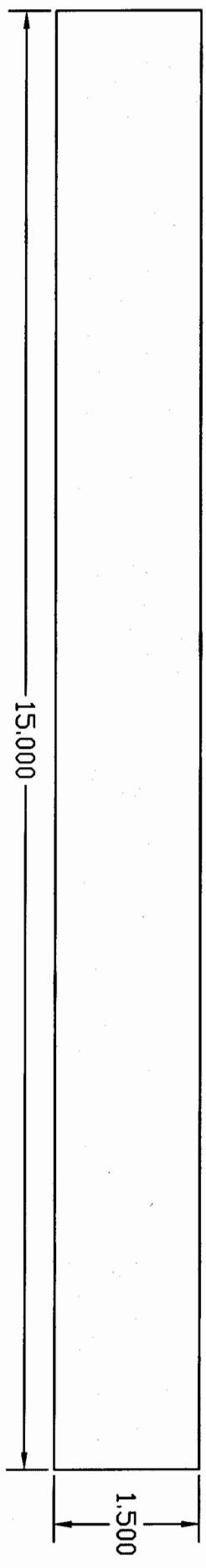


Detail F



Elevation

Plan

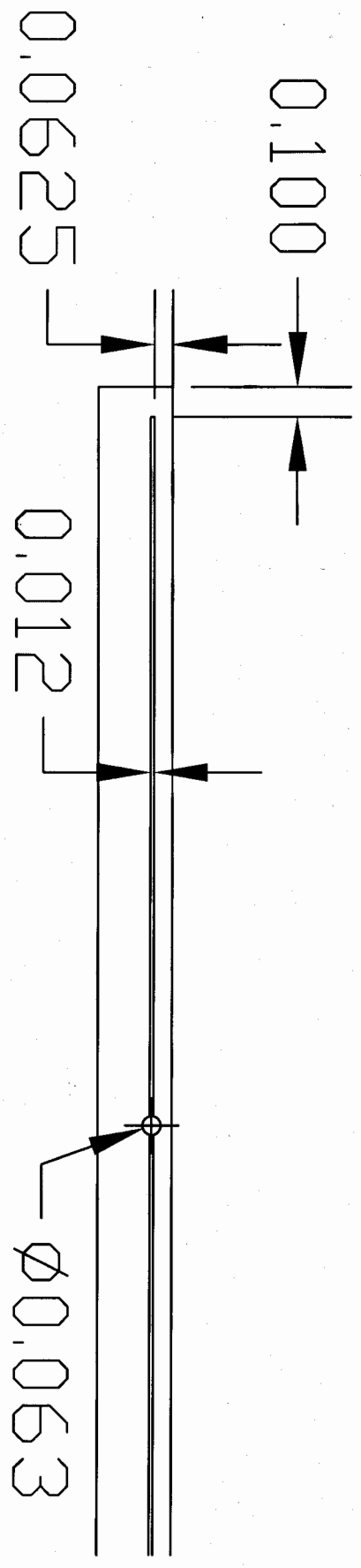


Aluminum 2024-O

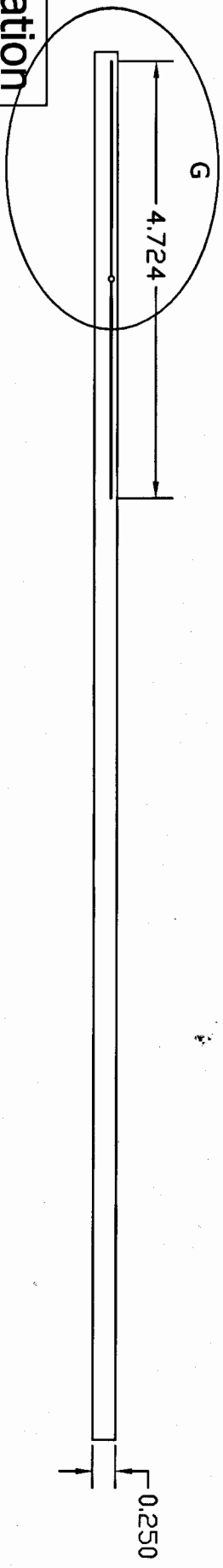
All dimensions in inches

All tolerances +/- 0.005

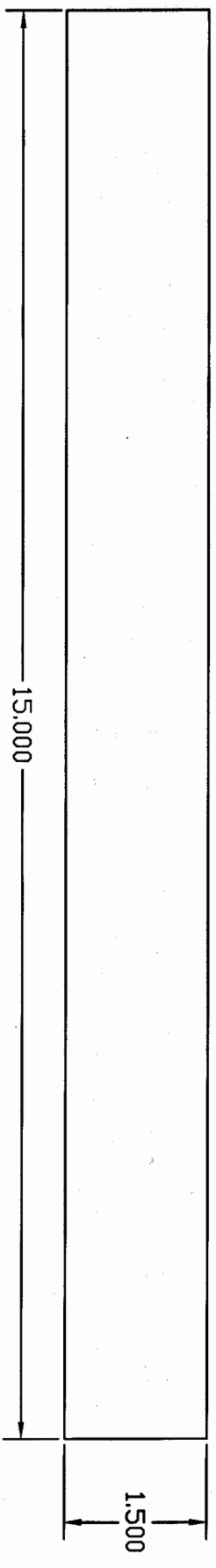
8cm notch, fixed end
Aaron Chmiel
aaron.chmiel@qaftr.edu



Detail G



Elevation



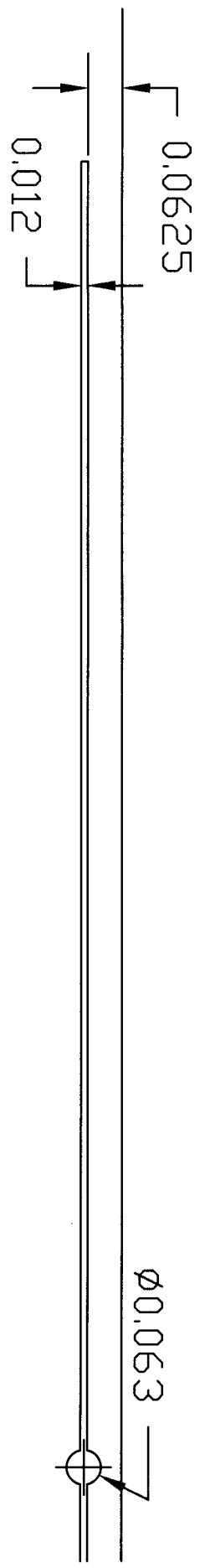
Plan

12cm notch, free end
Aaron Chmiel
aaron.chmiel@afit.edu

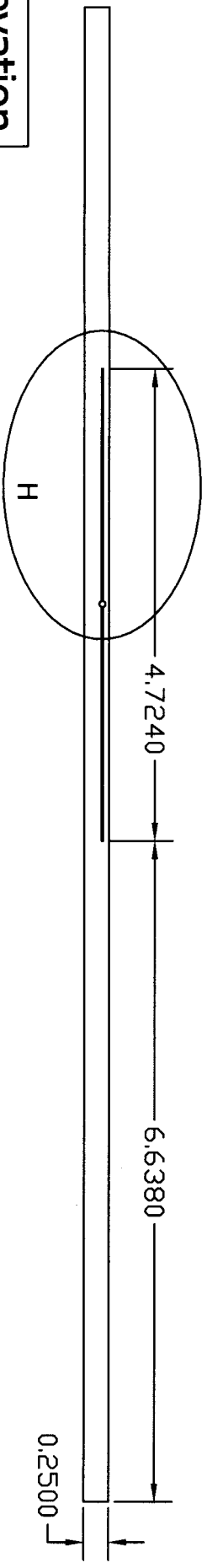
Aluminum 2024-O

All dimensions in inches

All tolerances +/- 0.005

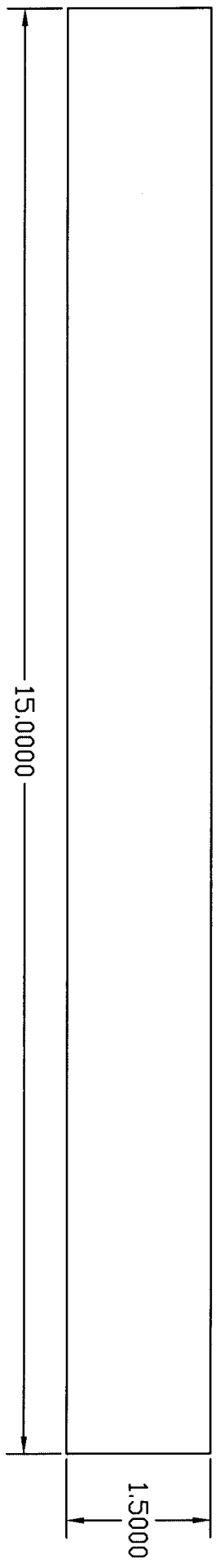


Detail H



Elevation

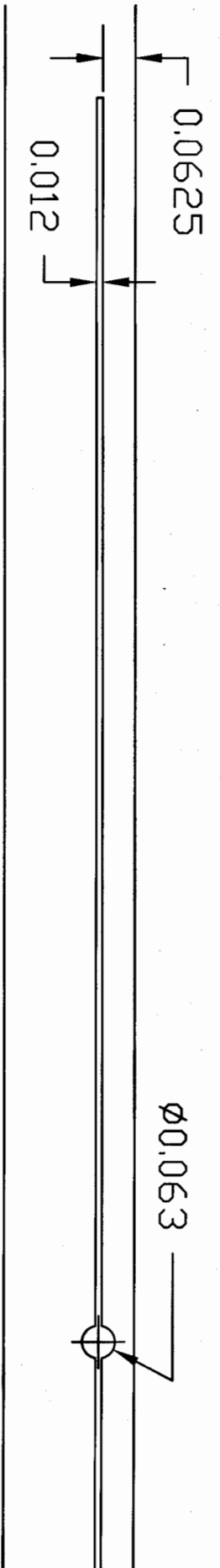
Plan



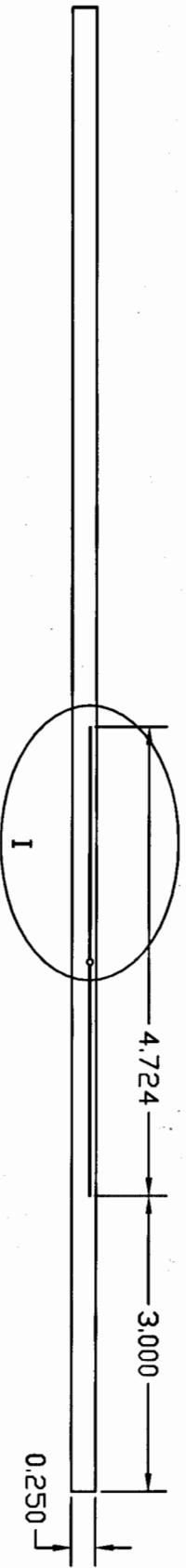
Aluminum 2024-O

All dimensions in inches

All tolerances +/- 0.005

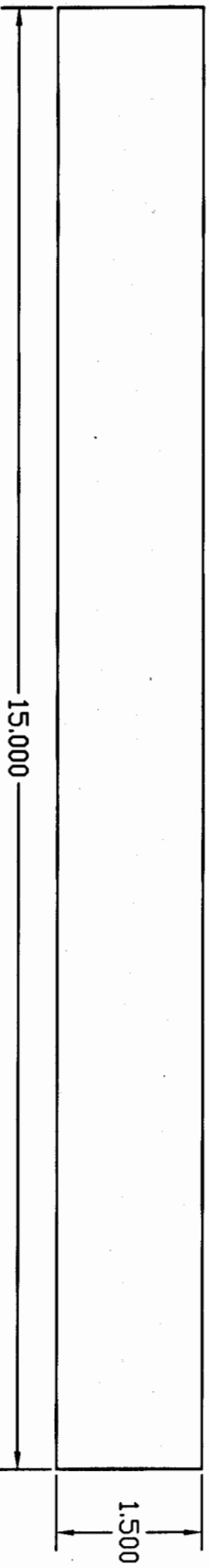


Detail I



Elevation

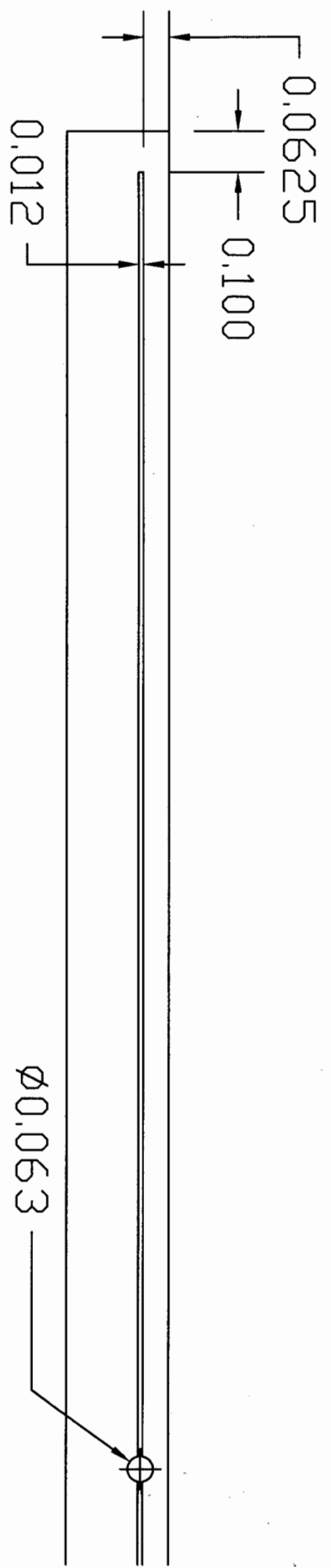
Plan



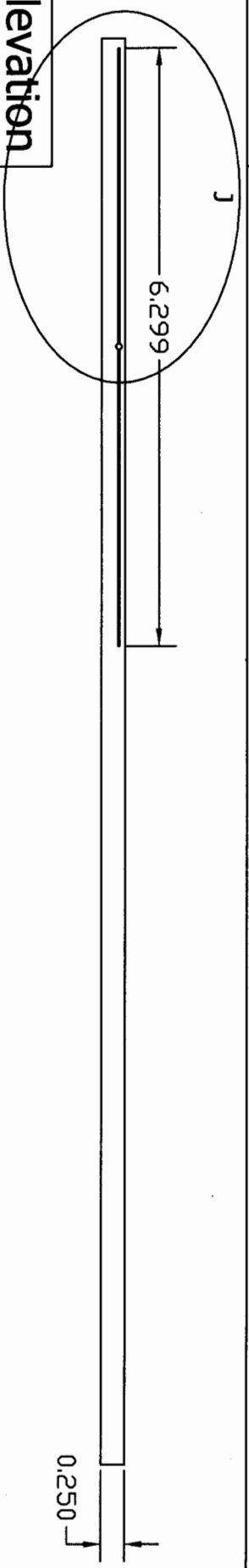
Aluminum 2024-O

All dimensions in inches

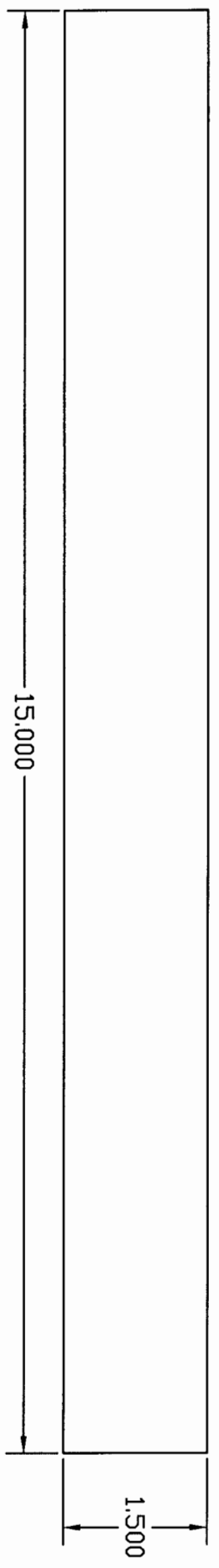
All tolerances +/- 0.005



Detail J



Elevation



16cm notch, free end
Aaron Chmiel
aaron.chmiel@afit.edu

Aluminum 2024-O

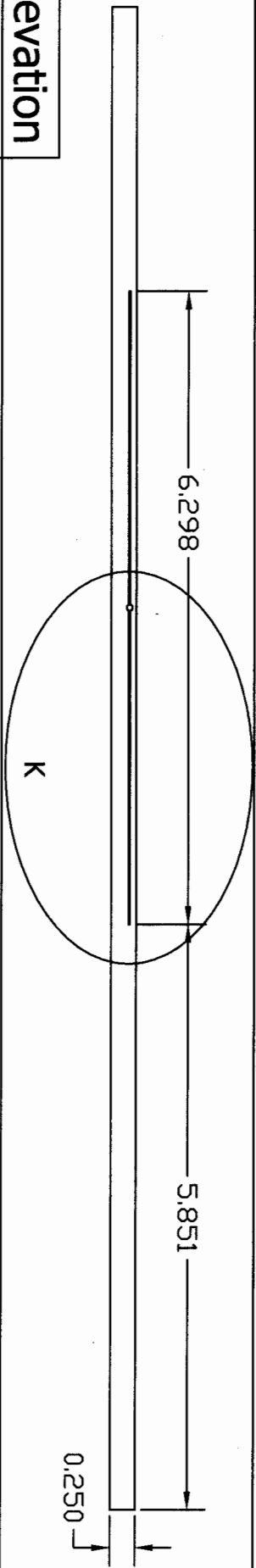
All dimensions in inches

All tolerances +/- 0.005

Ø0.063

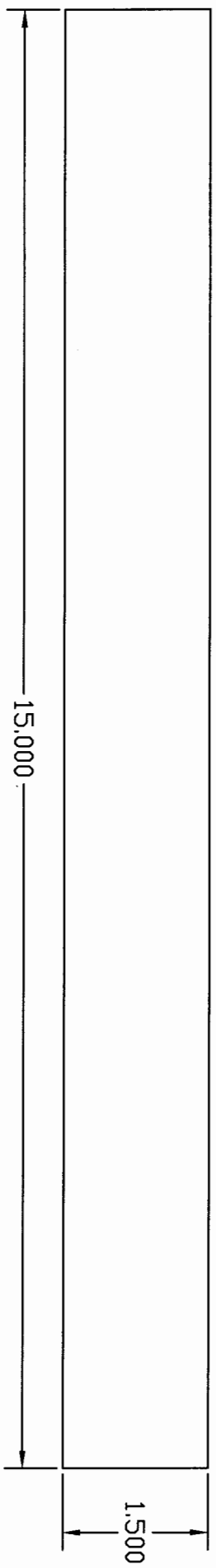
0.0625
0.012

Detail K



Elevation

Plan

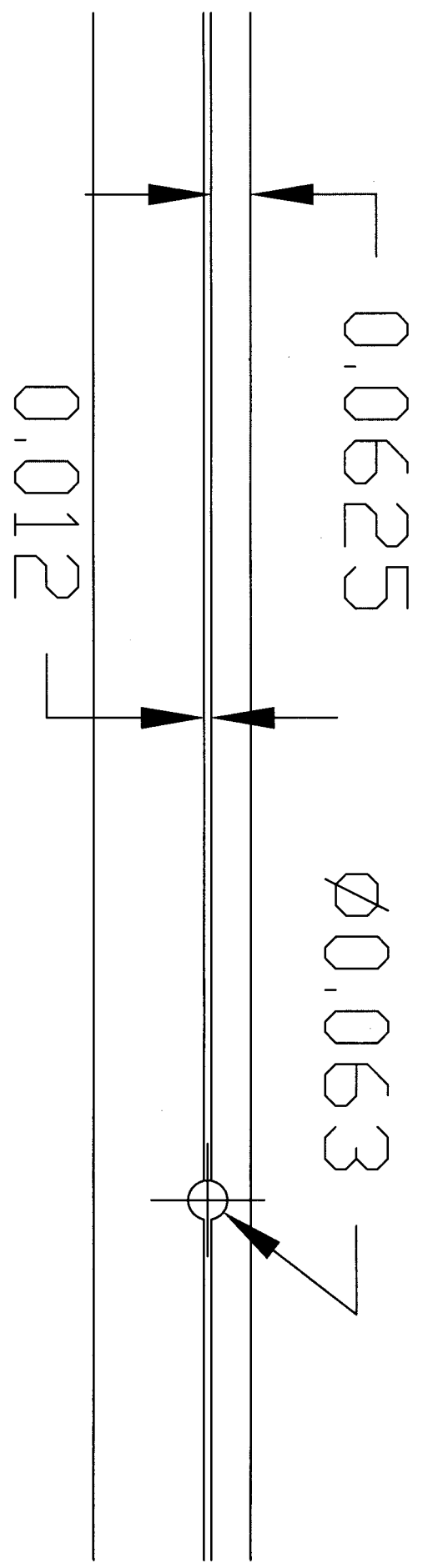


16cm notch, middle
Aaron Chmiel
aaron.chmiel@afit.edu

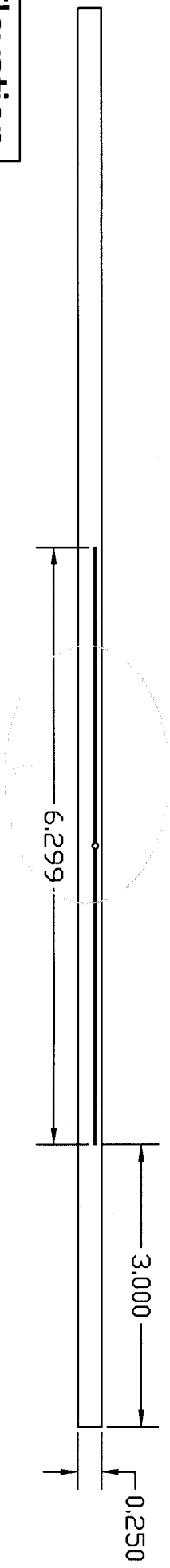
Aluminum 2024-O

All dimensions in inches

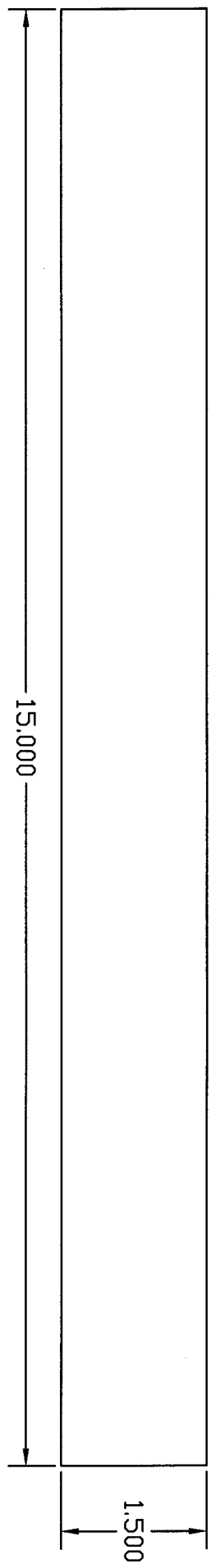
All tolerances +/- 0.005



Detail L



Elevation



Plan

Aluminum 2024-O

All dimensions in inches

All tolerances +/- 0.005

15cm notch, fixed end
Aaron Chmiel
aaron.chmiel@afit.edu

Bibliography

1. *Polytec Scanning Vibrometer: Theory Manual*. Version 8.1.
2. P.F. Aspragathos, A.D. Dimarogonas, and P.F. Rizos. Identification of crack location and magnitude in a cantilever beam from the vibration modes. *Journal of Sound and Vibration*, 138:381–388, 1990.
3. Martin Bauer, Frank Ritter, and Georg Siegmund. High-precision laser vibrometers based on digital Doppler-signal processing. In *Fifth International Conference on Vibration Measurement by Laser Techniques: Advances and Applications*, SPIE 4827, pages 49–61, 2002.
4. P. Cawley and R. Ray. A comparison of the natural frequency changes produced by cracks and slots. *Journal of Vibration, Acoustics, Stress, and Reliability in Design*, 110:366–370, 1988.
5. Richard Cobb. *Structural Damage Identification from Limited Measurement Data*. PhD thesis, Air Force Institute of Technology, Dayton, OH, 1996.
6. Richard Cobb. MECH 719 Vibration Damping and Control Class Notes. Air Force Institute of Technology, Fall 2004.
7. A.D. Dimarogonas.
8. Andrew D. Dimarogonas. Vibration of cracked structures: A state of the art review. *Engineering Fracture Mechanics*, 55(5):831–857.
9. Andrew D. Dimarogonas. *Vibration Engineering*. West Publishing Co., St Paul, MN, 1976.
10. James F. Doyle. Determining the size and location of transverse cracks in beams. *Experimental Mechanics*, 35:272–280, 1995.
11. D.J. Ewins. *Modal Testing: Theory and Practice*. Research Studies Press Ltd., 1984.
12. C.P. Fritzen and K. Bohle. Vibration-based global damage identification - A tool for rapid evaluation of structural safety. In Chang, editor, *Structural Health Monitoring*. 2004.
13. T.Y. Kam and T.Y. Lee. Detection of cracks in structures using modal test data. *Engineering Fracture Mechanics*, 42:381–387, 1992.
14. Magdalena Palacz, Marek Krawczuk, and Wiesaw Ostachowicz. The spectral finite element model for analysis of flexural-shear coupled wave propagation. *Composite Structures*, 68:45–51, 2005.

15. A.K. Pandey, M. Biswas, and M.M. Samman. Damage detection from changes in curvature mode shapes. *Journal of Sound and Vibration*, 145:321–332, 1991.
16. Victor Y. Perel. *Nonlinear Dynamics of Composite Delaminated Beam with Piezoelectric Actuator*. Trafford Publishing, Victoria, Canada, 2003.
17. Kenneth A. Ramsey. Effective measurements for structural dynamics testing. Available at <http://www.spectraldynamics.com/effective1.htm>.
18. Aaron Reifsnnyder. Vibrometric Detection of Beam Damage Due to Inclusions. Master's thesis, Air Force Institute of Technology, Dayton, OH, 2004.
19. O.S. Salawu. Detection of structural damage through changes in frequency: a review. *Engineering Structures*, 19:718–723, 1997.
20. H.-J. Schmidt and B. Schmidt-Brandecker. Structure design and maintenance benefits from health monitoring systems. In Chang, editor, *Structural Health Monitoring*, pages 80–101. 2004.
21. Joseph C. Slater. Vibration testing, with modal analysis and health monitoring. Technical report, Wright State University, Dayton, OH, 2002.
22. M.M.F. Yuen. A numerical study of the eigenparameters of a damaged cantilever. *Journal of Sound and Vibration*, 103:301–310, 1985.

REPORT DOCUMENTATION PAGE

Form Approved
OMB No. 0704-0188

The public reporting burden for this collection of information is estimated to average 1 hour per response, including the time for reviewing instructions, searching existing data sources, gathering and maintaining the data needed, and completing and reviewing the collection of information. Send comments regarding this burden estimate or any other aspect of this collection of information, including suggestions for reducing this burden to Department of Defense, Washington Headquarters Services, Directorate for Information Operations and Reports (0704-0188), 1215 Jefferson Davis Highway, Suite 1204, Arlington, VA 22202-4302. Respondents should be aware that notwithstanding any other provision of law, no person shall be subject to any penalty for failing to comply with a collection of information if it does not display a currently valid OMB control number. PLEASE DO NOT RETURN YOUR FORM TO THE ABOVE ADDRESS.

1. REPORT DATE (DD-MM-YYYY) 13-06-2005		2. REPORT TYPE Master's Thesis		3. DATES COVERED (From — To) Jul 2004 – Jun 2005	
4. TITLE AND SUBTITLE Internal Damage Detection and Assessment in Beams Using Experimental Natural Frequencies				5a. CONTRACT NUMBER	
				5b. GRANT NUMBER	
				5c. PROGRAM ELEMENT NUMBER	
6. AUTHOR(S) Durham, Frances K., Ensign, USNR				5d. PROJECT NUMBER	
				5e. TASK NUMBER	
				5f. WORK UNIT NUMBER	
7. PERFORMING ORGANIZATION NAME(S) AND ADDRESS(ES) Air Force Institute of Technology Graduate School of Engineering and Management (AFIT/EN) 2950 Hobson Way WPAFB OH 45433-8865				8. PERFORMING ORGANIZATION REPORT NUMBER AFIT/GAE/ENY/05-J03	
9. SPONSORING / MONITORING AGENCY NAME(S) AND ADDRESS(ES) AFRL/VASM Attn: Mr. Mark Derriso 2790 D Street WPAFB OH 45433				10. SPONSOR/MONITOR'S ACRONYM(S)	
				11. SPONSOR/MONITOR'S REPORT NUMBER(S)	
12. DISTRIBUTION / AVAILABILITY STATEMENT APPROVAL FOR PUBLIC RELEASE; DISTRIBUTION IS UNLIMITED.					
13. SUPPLEMENTARY NOTES					
14. ABSTRACT This study investigated the frequency response of a cantilever beam with the intent of establishing a reliable nondestructive method of damage detection. The test specimens were twelve Al 2024 T3 beams, each identical excepting a unique eccentrically located notch, and one reference notchless beam. The machined notches varied in length and location to simulate varying degrees of damage. Laser doppler vibrometry enabled the data acquisition. The changes in natural frequencies were correlated to notch length and notch location. A comparison of eccentric and centered notch influence on the natural frequencies was also discussed.					
15. SUBJECT TERMS Vibration, Vibration Testing, Structural Analysis, Cantilever Beams, Modal Analysis, Natural Frequency, Frequency, Resonant Frequency, Frequency Response, Laser Velocimeters, Delamination, Finite Element Analysis, Structural Health Monitoring					
16. SECURITY CLASSIFICATION OF:			17. LIMITATION OF ABSTRACT	18. NUMBER OF PAGES	19a. NAME OF RESPONSIBLE PERSON
a. REPORT	b. ABSTRACT	c. THIS PAGE			Anthony N. Palazotto, Ph.D. (ENY)
U	U	U	UU	143	19b. TELEPHONE NUMBER (include area code) (937) 255-3636, ext 4599